JETP Letters, Vol. 74, No. 11, 2001, pp. 523–528. Translated from Pis'ma v Zhurnal Éksperimental'noĭ i Teoreticheskoĭ Fiziki, Vol. 74, No. 11, 2001, pp. 595–600.

Chromomagnetic Catalysis of Color Superconductivity

V. Ch. Zhukovsky[1], K. G. Klimenko[2], V. V. Khudyakov[1], and D. Ebert[3]

[1] *Moscow State University, Vorob'evy gory, Moscow, 119899 Russia*

[2] *Institute for High Energy Physics, Protvino, Moscow region, 142284 Russia*

[3] *Institut für Physik, Humboldt-Universität zu Berlin, D-10115 Berlin, Germany*

Received October 15, 2001

The effect of an external chromomagnetic field on the phase structure of the extended Nambu–Jona–Lasinio model with two quark flavors is examined. It is shown that, depending on the relationship between the quark coupling constants in the $\bar{q}q$ and qq channels, chromomagnetic fields of certain types induce spontaneous breaking of chiral, color, or both symmetries simultaneously. © *2001 MAIK "Nauka/Interperiodica".*

PACS numbers: 12.38.Mh; 12.39.Fe

INTRODUCTION.

According to current QCD concepts, hadrons in the confinement phase existing at low temperatures and densities are elementary excitations of the ground state; i.e. quarks do not escape and color symmetry is unbroken. A nonzero chiral condensate $\langle \bar{q}q \rangle$ is the characteristic feature of this phase, flagging spontaneous chiral symmetry breaking (SCSB). It was predicted that, at high temperatures T, a system undergoes transition to the quark–gluon plasma state, where quarks are free and all symmetries of the QCD Lagrangian are recovered. For a sufficiently high baryon density (low T), a new phase with color superconductivity (CS) is expected to appear in QCD. This phase allows the formation of two-quark bound states (Cooper pairs) with a nonzero vacuum condensate $\langle qq \rangle$, indicating spontaneous color symmetry breaking.

The properties of the CS phase of matter was discussed more than twenty years ago [1]. This phenomenon was recently analyzed in [2] within the framework of one-gluon exchange in QCD, and it was proved that CS is, in principle, possible at the values of chemical potential μ above 10^8 MeV [3]. The corresponding baryon densities are so high that they exist neither in nature (neutron stars) nor in laboratory conditions (the densities in future experiments on ion–ion collisions will only be several times higher than the density of the ordinary nuclear matter; i.e., $\mu \sim 500$ MeV). The possibility of observing CS at intermediate baryon densities was proved only recently on the basis of various effective theories of a low-energy QCD region, including the Nambu–Jona–Lasinio (NJL) model (see [4–6] and the review [7] and references therein). In these works, allowance was made for the nonperturbative characteristic of a real QCD vacuum, such as SCSB, i.e., nonzero chiral condensate $\langle \bar{q}q \rangle$, to show that the CS effect can be manifested at much smaller values $\mu \approx 400$ MeV, i.e., in the near-future experiments on heavy-ion collisions.

It is important that the NJL and QCD Lagrangians have the same symmetry group. For this reason, the NJL model is successfully used in studying the properties of a nonperturbative QCD vacuum, in particular, under the action of external factors such as temperature and chemical potential [8]. These investigations are particularly important in the cases where the use of numerical lattice methods in QCD is hampered, i.e., in the presence of chemical potential and external magnetic field [9, 10]. Moreover, it was found on the basis of the NJL theories that arbitrarily weak external magnetic fields induce SCSB [11]. This effect was named magnetic catalysis of SCSB and has found application in different fields of physics (see reviews [12]).

It is well known that the low-energy QCD vacuum is characterized not only by the nonzero $\langle \bar{q}q \rangle \neq 0$, but also by the nonzero gluon condensate $\langle FF \rangle \equiv \langle F^a_{\mu\nu} F^{a\mu\nu} \rangle$, where $F^a_{\mu\nu}$ is the gluon field strength tensor. Since the NJL model is free of dynamical gluons, the gluon condensate is absent in it. To remedy the situation and describe physical processes more realistically, external color fields are usually employed as a gluon condensate in the NJL model [13]. In particular, it was shown in the NJL model with gluon condensate that, similar to an ordinary magnetic field, an external chromomagnetic field catalyzes SCSB [14].

In this work, the formation of CS is studied with allowance for two nonperturbative characteristics of the QCD vacuum, namely, chiral and gluon condensates. With this aim, the phase structure of the NJL model is considered in the presence of an external color field to demonstrate that chromomagnetic fields of certain types can induce color superconductivity, whose indicative feature is a nonzero diquark condensate. Since the chemical potential μ facilitates transition of the system to the CS state, whereas the role of gluon condensate

(external chromomagnetic field) in this process has not been adequately studied yet, it is set $\mu = 0$[1] throughout the work.

MODEL AND ITS EFFECTIVE POTENTIAL

Let us consider a (3 + 1)-dimensional NJL model with the Lagrangian

$$L = \bar{q}\gamma^{\nu}\left(i\partial_{\nu} + gA_{\nu}^{a}(x)\frac{\lambda_a}{2}\right)q + \frac{G_1}{2N_c}[(\bar{q}q)^2 + (\bar{q}i\gamma^5\boldsymbol{\tau}q)^2] + \frac{G_2}{N_c}[i\bar{q}_c\varepsilon\epsilon^b\gamma^5 q][i\bar{q}\varepsilon\epsilon^b\gamma^5 q_c]. \quad (1)$$

Here, the quark fields $q \equiv q_{i\alpha}$ form a flavor doublet (i = 1 and 2) and an $SU(3)_c$ color triplet (α = 1,2, and 3); $A_{\mu}^{a}(x)$ is the vector potential of the classical $SU(3)_c$ gauge field (for this reason, it is implied hereafter that $N_c = 3$); G_1 and G_2 are the independent coupling constants;[2] $q_c = C\bar{q}^t$ and $\bar{q}_c = q^tC$ are the charge-conjugate spinors, where $C = i\gamma^2\gamma^0$ and t denotes the transposition; $\boldsymbol{\tau} \equiv (\tau^1, \tau^2, \tau^3)$ are the Pauli matrices in the flavor space; λ_a are the Gell-Mann matrices; and $(\varepsilon)^{ik} \equiv \varepsilon^{ik}$ (i, k = 1, 2) and $(\epsilon^b)^{\alpha\beta} \equiv \epsilon^{\alpha\beta b}$ (α, β, b = 1, 2, 3) are the totally antisymmetric tensors in the flavor and color spaces, respectively. Lagrangian (1) is obviously invariant under the transformations of the chiral $SU(2)_L \times SU(2)_R$ and color $SU(3)_c$ groups.

Models of this type successfully describe the dynamics of mesons and diquarks, as well as the processes involving baryons in low-energy QCD with two quark flavors [17]. Moreover, model (1) is precisely that which was used to demonstrate that CS exists at $A_{\mu}^{a}(x) = 0$ in the region of moderate values of chemical potential $\mu \sim 400$ MeV [6].[3]

A linearized variant of model (1) with auxiliary boson fields has the form

$$\tilde{L} = \bar{q}\gamma^{\nu}\left(i\partial_{\nu} + gA_{\nu}^{a}(x)\frac{\lambda_a}{2}\right)q - \bar{q}(\sigma + i\gamma^5\boldsymbol{\tau}\boldsymbol{\pi})q - \frac{3}{2G_1}(\sigma^2 + \boldsymbol{\pi}^2) - \frac{3}{G_2}\Delta^{*b}\Delta^b - \Delta^{*b}[iq^tC\varepsilon\epsilon^b\gamma^5 q] - \Delta^b[i\bar{q}\varepsilon\epsilon^b\gamma^5 C\bar{q}^t]. \quad (2)$$

Lagrangians (1) and (2) are equivalent for the equations of motion for boson fields. It follows from these equations that

$$\Delta^b \sim iq^tC\varepsilon\epsilon^b\gamma^5 q, \quad \sigma \sim \bar{q}q, \quad \boldsymbol{\pi} \sim i\bar{q}\gamma^5\boldsymbol{\tau}q. \quad (3)$$

It is evident that the fields σ and $\boldsymbol{\pi}$ are color singlets' and the boson diquark fields Δ^b, each being a singlet of the $SU(2)_L \times SU(2)_R$ group, form a color antitriplet. Since σ and Δ^b are scalar fields, while $\boldsymbol{\pi}$ is a pseudoscalar field, the chiral symmetry of the model is spontaneously broken if $\langle\sigma\rangle \neq 0$, while $\langle\Delta^b\rangle \neq 0$ points to the dynamical color symmetry breaking.

In the one-loop approximation, the effective action for the boson fields can be represented in terms of the following continual integral with respect to the quark fields:

$$\exp(iS_{\text{eff}}(\sigma, \boldsymbol{\pi}, \Delta^b, \Delta^{*b}, A_{\mu}^{a})) = N'\int[d\bar{q}][dq]\exp(i\int\tilde{L}d^4x), \quad (4)$$

where N' is the normalization factor. We assume that all boson fields in Eq. (4), apart from A_{μ}^{a}, are independent of the space–time points. Since the function S_{eff} is invariant under the chiral, color, and Lorentz transformations, there always exists a coordinate system, in which $\Delta^1 = \Delta^2 = \boldsymbol{\pi} = 0$; i.e., $S_{\text{eff}} \equiv S_{\text{eff}}(\sigma, \Delta)$ where $\Delta \equiv \Delta^3$. We introduce next the effective potential V_{eff}: $S_{\text{eff}}(\sigma, \Delta) \equiv -V_{\text{eff}}(\sigma, \Delta)\int d^4x$. The point of global minimum of the effective potential determines the vacuum means of the fields and the symmetry group of the vacuum. In particular, if $\Delta \equiv \langle\Delta\rangle \neq 0$ at this point, then the SU(3) symmetry is spontaneously broken to SU(2) and the SC phenomenon arises. (If we introduced dynamical gluon fields in this case, three gluon fields would remain massless, whereas the other five gluon fields would become massive.) Now, let us represent an external uniform chromomagnetic field in the form $H^a = H_{\text{I}}^a + H_{\text{II}}^a$, where $H_{\text{I}}^a = (H^1, H^2, H^3, 0, \ldots, 0)$, $H_{\text{II}}^a = (0, 0, 0, H^4, \ldots, H^8)$. By analogy with the ordinary superconductivity, the H_{II}^a-type fields corresponding to massive gluons are expected to be expelled from an SC medium (Meissner effect). Moreover, strong fields of this type will destroy SC. However, our physical intuition tells us nothing about the effect of the H_{I}^a-type external fields on an SC medium. In what follows, it is assumed that a field of this type acts on the system. Without loss of generality, one can set $H^1 = H^2 = 0$ and $H^3 \equiv H$, i.e., assume that the field is directed along the third spatial axis. In this case, the field strength tensor has only the following nonzero components: $F_{12}^3 = -F_{21}^3 = H$. Correspondingly, a gluon condensate, whose effect on the NJL model (1) is simulated by this external chromo-

[1] The possibility of existing CS in the absence of an external field and at $\mu = 0$ was considered in [15, 16].

[2] In order to obtain physically acceptable estimates for the masses of (pseudo)vector mesons and diquarks in model (1), it is necessary to assume that the coupling constants are mutually independent [17]. In what follows, G_1 and G_2 are free parameters of the model.

[3] Similar phase structure was also predicted in a four-fermion model induced by the instanton structure of QCD vacuum at low energies [4].

magnetic field, has the value $\langle FF\rangle = 2H^2$. The vector potential $A_\nu^a(x)$ for such an external field can be chosen in the form

$$A_\nu^3(x) = (0, 0, Hx^1, 0); \quad A_\nu^a(x) = 0 \quad (a \neq 3). \tag{5}$$

In this case, the effective potential of the model at $H \neq 0$ is expressed as [18]

$$V_H(\sigma, \Delta) = \frac{3\sigma^2}{2G_1} + \frac{3\Delta\Delta^*}{G_2} - \frac{\tilde{S}(\sigma, \Delta)}{V}, \quad V = \int d^4x, \tag{6}$$

where

$$\exp(i\tilde{S}(\sigma, \Delta)) = N'\det[i\hat{\partial} - \sigma] \times \det{}^{1/2}\left[4|\Delta|^2 + \left(-i\hat{\partial} - \sigma - g\hat{A}^3\frac{\sigma_3}{2}\right)\left(i\hat{\partial} - \sigma + g\hat{A}^3\frac{\sigma_3}{2}\right)\right]. \tag{7}$$

Here, $\sigma_3 = \mathrm{diag}(1, -1)$ is the matrix in the two-dimensional color space, the operator in the first determinant acts only in the flavor, spinor, and coordinate spaces, while the operator in the second determinant acts, in addition, in the two-dimensional color space corresponding to the residual SU(2) vacuum symmetry.

Case $H = 0$. Setting $A_\nu = 0$ in Eq. (7) and using the formula $\det O = \exp(\mathrm{tr}\ln O)$, one can obtain the following expression for the effective potential:

$$V_0(\sigma, \Delta, \Delta^*) = \frac{3\sigma^2}{2G_1} + \frac{3|\Delta|^2}{G_2} - 8\int\frac{d^3k}{(2\pi)^3}\sqrt{\sigma^2 + 4|\Delta|^2 + k^2} - 4\int\frac{d^3k}{(2\pi)^3}\sqrt{\sigma^2 + k^2}. \tag{8}$$

The singular integrals in Eq. (8) are regularized using the compact domain of integration $|\mathbf{k}| \leq \Lambda$. The integration gives $V_0(\sigma, \Delta, \Delta^*) = \Lambda^4 v_0(x, y)/\pi^2$, where

$$v_0(x, y) = \frac{3A}{2}x^2 + By^2 - \frac{1}{2}\sqrt{1 + x^2} - \frac{x^2}{4}F(x) - \sqrt{1 + x^2 + y^2} - \frac{x^2 + y^2}{2}F(\sqrt{x^2 + y^2}). \tag{9}$$

Here,

$$x = \frac{\sigma}{\Lambda}, \quad y = \frac{2|\Delta|}{\Lambda}, \quad A = \frac{\pi^2}{G_1\Lambda^2}, \quad B = \frac{3\pi^2}{4G_2\Lambda^2}, \quad F(x) = \sqrt{1 + x^2} - x^2\ln\frac{1 + \sqrt{1 + x^2}}{x}. \tag{10}$$

The stationarity equations for the potential $v_0(x, y)$ have the form

$$\frac{\partial v_0(x, y)}{\partial x} \equiv x\{3A - F(x) - 2F(\sqrt{x^2 + y^2})\} = 0, \tag{11}$$

$$\frac{\partial v_0(x, y)}{\partial y} \equiv 2y\{B - F(\sqrt{x^2 + y^2})\} = 0. \tag{12}$$

It is easy to show that the function $F(x)$ in these equations decreases monotonically from $F(0) = 1$ to $F(\infty) = 0$ on the $x \in (0, \infty)$ interval $F(x) = 2/3x + o(1/x)$ at $x \longrightarrow \infty$. In addition, $F'(0) = 0$. The function $f(x)$, the inverse of $F(x)$ on the $x \in (0, 1)$ interval [recall that $x \equiv F(f(x))$], decreases monotonically from $f(0) = +\infty$ [$f(x) = 1/x + \ldots$ at $x \longrightarrow 0$] to $f(1) = 0$. In this case, $f'(1) = -\infty$. This information is sufficient to arrive at the following conclusions.

There are four types of solutions to Eqs. (11) and (12):

(I) the (0, 0) solution. It exists for all values $A, B \geq 0$;

(II) the $(x_0, 0)$ solution, where $x_0 = f(A)$. It exists for all values $0 \leq A \leq 1$;

(III) the $(0, y_0)$ solution, where $y_0 = f(B)$. It exists for all values $0 \leq B \leq 1$;

(IV) the $(\tilde{x}_0, \tilde{y}_0)$ solution. In this case, the expressions in brackets in Eqs. (11) and (12) are zero. It follows from Eq. (12) that $\sqrt{\tilde{x}_0^2 + \tilde{y}_0^2} = f(B)$ if $0 \leq B \leq 1$. Taking into account this fact, from Eq. (11) one obtains $\tilde{x}_0 = f(3A - 2B)$ if $0 \leq 3A - 2B \leq 1$, and

$$\tilde{y}_0^2 = f^2(B) - f^2(3A - 2B). \tag{13}$$

The $\tilde{y}_0^2$ value must be nonnegative. Taking into account this requirement, the monotonic decrease of the function $f(x)$ and Eq. (13), one obtains the following limitation on A and B: $B \leq A$. Therefore, the type-IV solution exists only in the ω domain where

$$\omega = \{(A, B): B \geq 0, B \leq A, 3A - 2B \leq 1\}. \tag{14}$$

To determine the global minimum (GM) of the potential (9), it is necessary to find its values at stationary points of types I–IV and select the lowest of them. The result of this procedure carried out for each fixed A, B pair is shown in Fig. 1 as a phase portrait of the model. In this figure, the (A, B) plane is divided into four domains (phases), each labeled according to the stationary point, at which the GM of the potential is located for all points (A, B) from the domains considered. Therefore, the GM for domain I is a type-I stationary point, and this domain corresponds to the completely symmetric phase of the theory. Domain II corresponds to the GM in which $\langle\bar{q}q\rangle \neq 0$ and $\langle qq\rangle = 0$. Therefore, it corresponds to the SCSB phase. Domain III is the CS phase, because the GM for all points of this domain corresponds to nonzero diquark condensate. Finally, domain IV coinciding with ω (14) corresponds

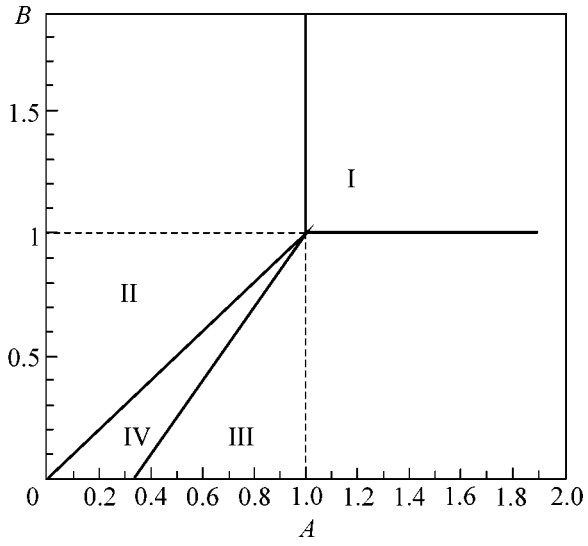

Fig. 1. The (*A*, *B*) phase portrait of the model at $H = 0$. The left and right boundaries of domain IV are the straight lines $B = A$ and $3A - 2B = 1$, respectively.

to the mixed phase of the model, because both condensates are nonzero in this case: $\langle qq \rangle \neq 0$ and $\langle \bar{q}q \rangle \neq 0$.

Vanderheyden and Jackson [16] used the random matrix method to consider the possibility of existing CS for $\mu = 0$ and $H = 0$. Using general symmetry laws, they derived a strict limitation on the quark coupling constants in the $\bar{q}q$ and qq channels, for which CS is forbidden. In terms of model (1), it has the form $B > A$. Using the phase portrait of the model (see Fig. 1), it is easy to verify that our results are consistent with this limitation.

Case $H \neq 0$. Let us now consider the effect of an external chromomagnetic field with vector potential (5) on the phase structure of the model. In this case, using the methods developed in [10], one can easily obtain from Eqs. (6) and (7)

$$V_H(\sigma, \Delta, \Delta^*) = \frac{3\sigma^2}{2G_1} + \frac{3|\Delta|^2}{G_2}$$

$$+ \frac{dH}{4\pi^2}\int_0^\infty \frac{ds}{s^2}\exp(-s(\sigma^2 + 4|\Delta|^2))\coth(gHs/2) \qquad (15)$$

$$- 4\int \frac{d^3k}{(2\pi)^3}\sqrt{\sigma^2 + k^2}.$$

Potential (15) diverges in the ultraviolet limit. After regularization, it reduces to the form

$$\nu_h(x, y) = \nu_0(x, y)$$

$$- \frac{h^2}{2}\left\{\zeta'(-1, z) - \frac{1}{2}[z^2 - z]\ln z + \frac{z^2}{4}\right\}, \qquad (16)$$

where the same notations are used as in Eqs. (9) and (10) and the new notations are also introduced:

$$V_H(\sigma, \Delta, \Delta^*) = \frac{\Lambda^4}{\pi^2}\nu_h(x, y),$$
$$h = \frac{gH}{\Lambda^2}, \quad z = \frac{x^2 + y^2}{h}. \qquad (17)$$

In addition, $\zeta'(-1, x) = d\zeta(\nu, x)/d\nu|_{\nu = -1}$, where $\zeta(\nu, x)$ is the generalized Riemann zeta function. The stationarity equations for potential (16) have the form

$$\frac{\partial \nu_h(x, y)}{\partial x} \equiv x\{3A - F(x)$$
$$- 2F(\sqrt{x^2 + y^2}) - hI(z)\} = 0, \qquad (18)$$

$$\frac{\partial \nu_h(x, y)}{\partial y} \equiv y\{2B - 2F(\sqrt{x^2 + y^2}) - hI(z)\} = 0, \quad (19)$$

where the function $F(x)$ is defined in Eq. (10), and

$$I(z) = \frac{1}{2}\int_0^\infty \frac{ds}{s^2}\exp(-2sz)[s\coth(s) - 1]. \qquad (20)$$

It is easy to show that the function $I(z)$ decreases monotonically from $+\infty$ to zero on the interval $z \in (0, \infty)$. Taking into account a monotonic decrease of the function $F(x)$, from Eqs. (18) and (19) one can obtain the partial derivatives $\partial \nu_h(x, 0)/\partial x$ and $\partial \nu_h(0, y)/\partial y$, which are negative at small x or y values, respectively. In other words, the potential $\nu_h(x, y)$ at the origin of coordinates decreases along both the x and y axes. This simple observation leads to a very important conclusion. For nonzero, including arbitrarily weak, external fields (5), the point (0, 0) cannot be the global minimum of the effective potential; i.e., the original symmetry of the model is necessarily spontaneously broken, irrespective of the value of the coupling constant. In particular, if the vacuum of the model is symmetric for some G_1 and G_2 values, then either chiral, or color, or both symmetries simultaneously are broken at $H \neq 0$. This phenomenon is referred to as chromomagnetic catalysis of dynamical symmetry breaking. Previously [14], it was observed in the simplest NJL model, where the chromomagnetic field induced SCSB.

Using numerical methods, one can gain more detailed information about the phase structure. In particular, Fig. 2 shows the (*A*, *B*) phase portrait of model (1) for several values of variable h. It is seen that the straight line $3A - 2B = 1$ is the boundary between CS phase III and mixed phase IV, while the boundary between phase IV and SBCS phase II depends on the parameter h. For each given h value, the left and right boundaries of phase IV coincide with each other only asymptotically at $A, B \longrightarrow \infty$. For all h values, mixed phase IV lies inside the domain $\Omega = \{(A, B): 0 < 3A - 2B < 1\}$ and $\omega \subset \Omega$. One can show that, for an arbi-

trarily fixed point $(A, B) \in \Omega$, there exists a critical field $H_{cr}(A, B)$ such that the transition to phase IV occurs at $H > H_{cr}(A, B)$. Figure 3 shows the values $h_{cr}(A, B) = gH_{cr}(A, B)/\Lambda^2$ for some (A, B) points. In this figure, one curve is the graph of function $h_{cr}(A, B=1.5)$ [the parameter A varies so that the point $(A, B = 1.5)$ moves along the straight line within Ω] and the second curve is the function $h_{cr}(A = 1.2, B)$ (the arguments A and B of these functions correspond to the same axis in Fig. 3). It is seen that, as the point $(A, B =1.5)$ approaches the left boundary of the domain Ω, i.e., as $A \longrightarrow 1$, the critical field $H_{cr}(A, B = 1.5)$ tends toward infinity [the left dashed line in Fig. 3 is the vertical asymptote for the function $h_{cr}(A, B = 1.5)$]. The function $h_{cr}(A = 1.2, B)$ behaves in a similar way and tends toward infinity as $B \longrightarrow 1.8$.

DISCUSSION

Comparison of the phase diagrams in Figs. 1 and 2 indicates that, under the action of an external chromomagnetic field (5), CS phase III expands at the sacrifice of phase I, whereas mixed phase IV expands at the sacrifice of phases I and II. In this connection, the chromomagnetic catalysis of CS (i.e., a chromomagnetic-field-induced dynamical color symmetry breaking and appearance of a nonzero diquark condensate) in model (1) has three qualitatively different singularities: (i) if a point (A, B) is in domain I (Fig. 1) but is below the straight line $3A - 2B = 1$, then the arbitrarily weak field $H = 0_+$ induces color symmetry breaking. In this case, $\langle \bar{q}q \rangle = 0$ and $\langle qq \rangle \neq 0$; (ii) if a point (A, B) is in domain I and $(A, B) \in \Omega$, then the SCSB phase with $\langle \bar{q}q \rangle \neq 0$ and $\langle qq \rangle = 0$ is spontaneously generated at $H = 0_+$, and, for sufficiently high $H > H_{cr}(A, B)$, the system undergoes transition to mixed phase IV, where both condensates are nonzero; (iii) if the coupling constants are such that a point (A, B) is in domain II (Fig. 1) and $(A, B) \in \Omega$, then the external field induces transition from the SCSB phase to mixed phase IV at sufficiently high $H > H_{cr}(A, B)$.

As in the simplest NJL model [14], this model also allows the chromomagnetic catalysis of SCSB. Indeed, if a point (A, B) from domain I lies above the straight line $3A - 2B = 0$, then the SCSB phase is generated at $H > 0_+$.

Recall that, at $\mu = 0$ and $H = 0$, the formation of a diquark condensate is impossible under some general constraint on the quark coupling constants in the $\bar{q}q$ and qq channels [16]. We have demonstrated that, at $\mu = 0$ and $H \neq 0$, there is an even more stringent constraint on the domain forbidden for the CS and mixed phases. Indeed, the $\langle qq \rangle$ condensate is forbidden in the domain $B > A$ (Fig. 1) in model (1) at $\mu = 0$ and $H = 0$. However, at $\mu = 0$ and $H \neq 0$, the CS and mixed phases cannot exist in the narrower domain $2B > 3A$ (Fig. 2).

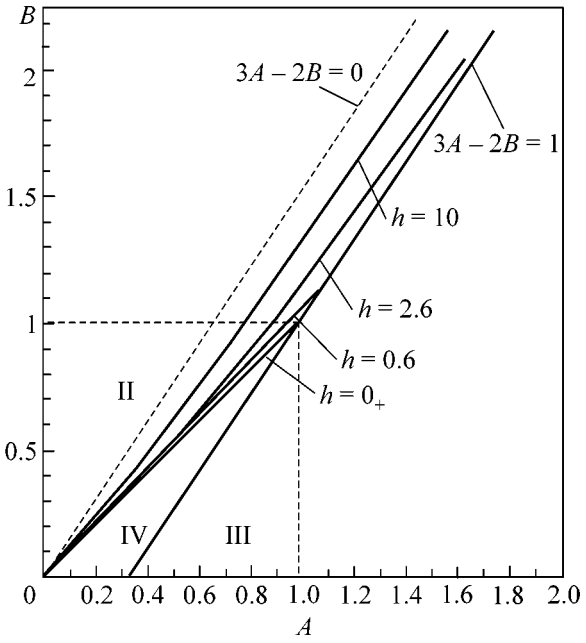

Fig. 2. The (A, B) phase portrait of the model for several values of $h = gH/\Lambda^2$.

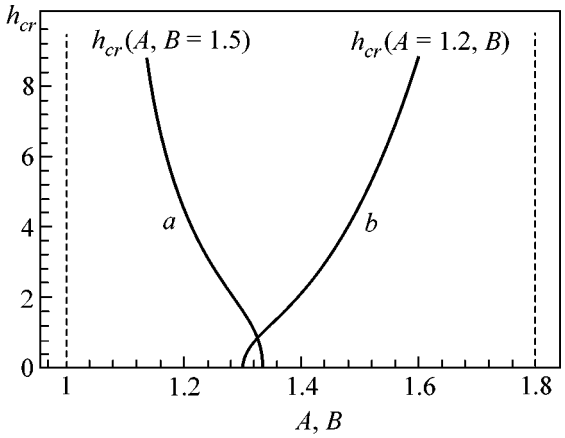

Fig. 3. The critical h values for the transition of the system from the SCSB phase to the mixed phase in two cases: (*a*) $B = 1.5$ and A variable and (*b*) $A = 1.2$ and B variable (for more detail, see text).

Finally, if a point (A, B) belongs to domain II (Fig. 1) and lies above the straight line $3A - 2B = 0$, then the system remains in the SCSB phase for all H values. Nevertheless, the chiral condensate $\langle \bar{q}q \rangle$ depends on H in this case; and, as a result, the commonly accepted picture of CS formation can alter, at least quantitatively, at a nonzero chemical potential.

This work was supported by the Deutsche Forschungs Gesellschaft (DFG project nos. 436 RUS and 113/477/4).

REFERENCES

1. B. C. Barrois, Nucl. Phys. B **129**, 390 (1977); S. C. Frautschi, in *Proceedings of the Workshop on Hadronic Matter at Extreme Energy Density, Erice, Italy, 1978*, Ed. by N. Cabibbo; D. Bailin and A. Love, Phys. Rep. **107**, 325 (1984).
2. D. T. Son, Phys. Rev. D **59**, 094019 (1999); D. K. Hong, Nucl. Phys. B **582**, 451 (2000); S. D. H. Hsu and M. Schwetz, Nucl. Phys. B **572**, 211 (2000); R. D. Pisarsky and D. H. Rischke, Phys. Rev. D **61**, 074017 (2000).
3. K. Rajagopal and E. Shuster, Phys. Rev. D **62**, 085007 (2000).
4. R. Rapp, T. Schafer, E. A. Shuryak, *et al.*, Phys. Rev. Lett. **81**, 53 (1998); Ann. Phys. **280**, 35 (2000); M. Alford, K. Rajagopal, and F. Wilczek, Phys. Lett. B **422**, 247 (1998); Nucl. Phys. B **537**, 443 (1999); K. Langfeld and M. Rho, Nucl. Phys. A **660**, 475 (1999); R. Nebauer, F. Gastineau, and J. Aichelin, hep-ph/0101289.
5. J. Berges and K. Rajagopal, Nucl. Phys. B **538**, 215 (1999).
6. T. M. Schwarz, S. P. Klevansky, and G. Papp, Phys. Rev. C **60**, 055205 (1999).
7. M. Alford, hep-ph/0102047.
8. S. Kawati and H. Miyata, Phys. Rev. D **23**, 3010 (1981); V. Bernard, U.-G. Meissner, and I. Zahed, Phys. Rev. D **36**, 819 (1987); Chr. V. Christov and K. Goeke, Acta Phys. Pol. B **22**, 187 (1991); D. Ebert, Yu. L. Kalinovsky, L. Munchow, *et al.*, Int. J. Mod. Phys. A **8**, 1295 (1993); A. S. Vshivtsev, K. G. Klimenko, and V. Ch. Zhukovsky, Pis'ma Zh. Éksp. Teor. Fiz. **64**, 313 (1996) [JETP Lett. **64**, 338 (1996)]; Zh. Éksp. Teor. Fiz. **111**, 1921 (1997) [JETP **84**, 1047 (1997)].
9. S. P. Klevansky and R. H. Lemmer, Phys. Rev. D **39**, 3478 (1989); H. Suganuma and T. Tatsumi, Ann. Phys. **208**, 470 (1991); T. Inagaki, S. D. Odintsov, and Yu. I. Shil'nov, Int. J. Mod. Phys. A **14**, 481 (1999).
10. A. S. Vshivtsev, K. G. Klimenko, and B. V. Magnitsky, Pis'ma Zh. Éksp. Teor. Fiz. **62**, 265 (1995) [JETP Lett. **62**, 283 (1995)]; Teor. Mat. Fiz. **106**, 390 (1996); D. Ebert, M. A. Vdovichenko, K. G. Klimenko, *et al.*, Phys. Rev. D **61**, 025005 (2000); Yad. Fiz. **64**, 386 (2001) [Phys. At. Nucl. **64**, 336 (2001)]; M. A. Vdovichenko, A. S. Vshivtsev, and K. G. Klimenko, Yad. Fiz. **63**, 542 (2000) [Phys. At. Nucl. **63**, 470 (2000)].
11. K. G. Klimenko, Teor. Mat. Fiz. **89**, 211 (1991); **90**, 3 (1992); Z. Phys. C **54**, 323 (1992); I. V. Krive and S. A. Naftulin, Phys. Rev. D **46**, 2737 (1992); V. P. Gusynin, V. A. Miransky, and I. A. Shovkovy, Phys. Rev. Lett. **73**, 3499 (1994).
12. A. S. Vshivtsev, V. Ch. Zhukovsky, K. G. Klimenko, *et al.*, Fiz. Élem. Chastits At. Yadra **29**, 1259 (1998) [Phys. Part. Nucl. **29**, 523 (1998)]; V. P. Gusynin, Ukr. J. Phys. **45**, 603 (2000).
13. D. Ebert and M. K. Volkov, Phys. Lett. B **272**, 86 (1991); D. Ebert, Yu. L. Kalinovsky, and M. K. Volkov, Phys. Lett. B **301**, 231 (1993).
14. K. G. Klimenko, B. V. Magnitsky, A. S. Vshivtsev, *et al.*, Nuovo Cimento A **107**, 439 (1994); Teor. Mat. Fiz. **101**, 391 (1994); Yad. Fiz. **57**, 2260 (1994) [Phys. At. Nucl. **57**, 2171 (1994)]; I. A. Shovkovy and V. M. Turkowski, Phys. Lett. B **367**, 213 (1996); D. Ebert and V. Ch. Zhukovsky, Mod. Phys. Lett. A **12**, 2567 (1997).
15. A. Chodos, F. Cooper, and H. Minakata, hep-ph/9905521; D. Diakonov *et al.*, Phys. Lett. B **373**, 147 (1996).
16. B. Vanderheyden and A. D. Jackson, Phys. Rev. D **61**, 076004 (2000).
17. D. Ebert, Yu. L. Kalinovsky, L. Munchow, and M. K. Volkov, Int. J. Mod. Phys. A **8**, 1295 (1993); D. Ebert, L. Kaschluhn, and G. Kastelewicz, Phys. Lett. B **264**, 420 (1991).
18. D. Ebert, K. G. Klimenko, and H. Toki, Phys. Rev. D **64**, 014038 (2001); D. Ebert, K. G. Klimenko, H. Toki, *et al.*, hep-th/0106049; D. Ebert, V. V. Khudyakov, K. G. Klimenko, *et al.*, hep-ph/0106110; hep-ph/0108185.

Translated by R. Tyapaev

JETP Letters, Vol. 74, No. 11, 2001, pp. 529–531. Translated from Pis'ma v Zhurnal Éksperimental'noĭ i Teoreticheskoĭ Fiziki, Vol. 74, No. 11, 2001, pp. 601–604.

Double Beta Decay of ^{100}Mo

V. D. Ashitkov[1], A. S. Barabash[1,*], S. G. Belogurov[1], G. Carugno[2], S. I. Konovalov[1], F. Massera[3], G. Puglierin[2], R. R. Saakyan[1,4], V. N. Stekhanov[1], and V. I. Umatov[1]

[1] *Institute of Theoretical and Experimental Physics, ul. Bol'shaya Cheremushkinskaya 25, Moscow, 117259 Russia*
** e-mail: barabash@vxitep.itep.ru*
[2] *Dipartimento di Fisica e INFN, Università di Padova, I-35131 Padova, Italy*
[3] *INFN, Serzione di Bologna, 40126 Bologna, Italy*
[4] *Laboratory Nazionali del Gran Sasso dell'INFN, I-67010 Assergi (L'Aquila), Italy*

Received November 2, 2001

Two-neutrino double beta decay of ^{100}Mo with half-life $T_{1/2} = [7.2 \pm 0.9(stat) \pm 1.8(syst)] \times 10^{18}$ yr was detected using a liquid argon ionization chamber. With a C.L. of 68% (90%), the bounds on neutrinoless decay and decay with majoron emission were found to be $8.4(4.9) \times 10^{21}$ and $4.1(3.2) \times 10^{20}$ yr, respectively. An analysis of all available results provides the average "world" value $T_{1/2} = (8.0 \pm 0.7) \times 10^{18}$ yr for the two-neutrino decay of ^{100}Mo, and the corresponding nuclear matrix element is $M_{GT} = 0.118 \pm 0.005$. © *2001 MAIK "Nauka/Interperiodica".*

PACS numbers: 23.40.Bw

Neutrinoless double beta decay, $2\beta(0\nu)$, is being actively searched, because it is closely related to many fundamental concepts of the physics of elementary particles (see, e.g., reviews [1–3]): lepton-number nonconservation; the existence of neutrino mass and its origin; the presence of right-handed currents in electroweak interaction; the existence of majoron; the structure of the Higgs sector; supersymmetry; and the existence of leptoquarks, heavy sterile neutrinos, and composed neutrinos.

All these problems are beyond the scope of the Standard Model of electroweak interaction. Therefore, the detection of $2\beta(0\nu)$ decay will signify the discovery of a new physics. Of course, the principal interest in this process is associated with the problem of neutrino mass, because the detection of the $2\beta(0\nu)$ decay will mean, according to current concepts, that the rest mass of at least one neutrino type is nonzero, and this is the Majorana-type mass.[1]

To date, only the lower bounds on the half-lives with respect to the neutrinoless decay have been experimentally determined for various nuclei. These bounds are used to obtain the limits on the neutrino Majorana mass, the right-handed current admixture parameters, the majoron–neutrino coupling constant, and so on. However, because of the uncertainties in the calculations of the nuclear matrix elements (NMEs), one cannot obtain sufficiently reliable limits on these fundamental quantities. In this connection, of particular importance is the detection of two-neutrino double beta decay, $2\beta(2\nu)$, because it can provide information about the NME(2ν) values for various nuclei, which, in turn, will aid in refining theoretical insight into 2β decay and in improving the accuracy of calculations of NME(2ν) and NME(0ν) (see, e.g., [6]). Moreover, the precision investigation of this process is of interest from the viewpoint of searching for the possible time dependence of the weak interaction constant [7, 8].

The ^{100}Mo nucleus is one of the most promising nuclei for examining 2β decay. This is primarily due to the sufficiently high energy (3034 keV) of the 2β transition. In addition, the $^{100}\mathrm{Mo}(0^+_{g.s.})$–$^{100}\mathrm{Ru}(0^+_{g.s.})$ transition is characterized by the largest values of both NME(2ν) (as follows from experimental data; see, e.g., review [9]) and NME(0ν) (according to the recent calculations [2, 6, 10]). It was also pointed out in [7, 8] that the ^{100}Mo nucleus is a good candidate for a geochemical $2\beta(2\nu)$ experiment. The subsequent comparison of the geochemical result with the results of direct (counter) experiments will make it possible to draw a conclusion about the constancy of the weak interaction constant (for more detail, see [7, 8]). In this connection, the accurate direct measurement of the $2\beta(2\nu)$ half-life of ^{100}Mo is of particular importance. By now, positive results on the $2\beta(2\nu)$ decay of ^{100}Mo have already been obtained in [11–15], where the half-life values from $[6.75^{+0.37}_{-0.42}(stat) \pm 0.68(syst)] \times 10^{18}$ yr [15] to $11.5^{+3.0}_{-2.0} \times 10^{18}$ yr [11] were found.

[1] The results of recent Super-Kamiokande [4] and SNO [5] experiments are treated as the observation of neutrino oscillations. If these conclusions are corroborated, this will mean that a neutrino has nonzero mass. However, the oscillatory experiments cannot solve the problem of the origin of neutrino mass (Dirac or Majorana?) and cannot provide information about the absolute value of mass (because the Δm^2 value is measured).

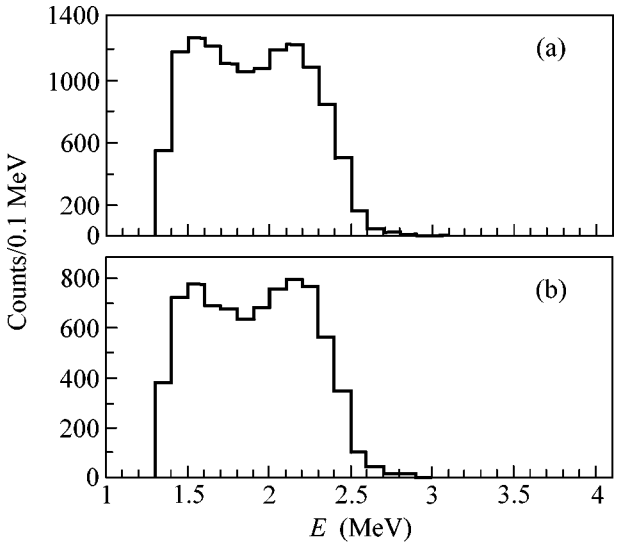

Fig. 1. The total spectra of two-electron events for (a) enriched (848.2 kg h) and (b) natural (592.9 kg h) molybdenum.

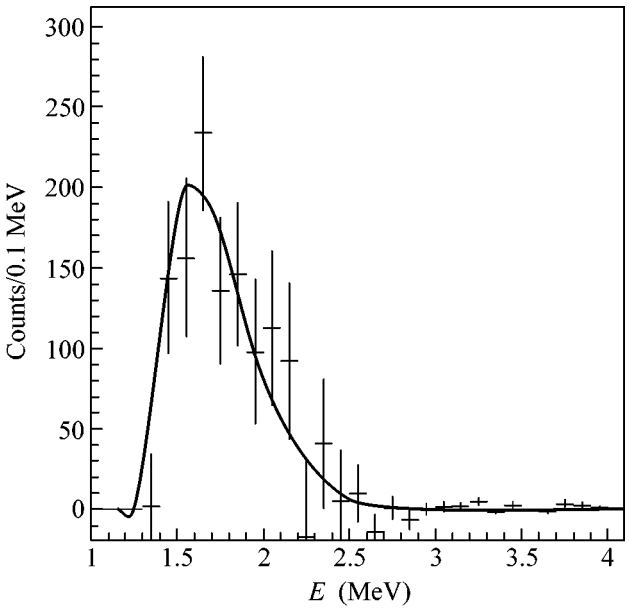

Fig. 2. Difference between the two-electron spectra of the molybdenum-enriched and natural-molybdenum samples. The curve is the calculated spectrum of the $2\beta(2\nu)$ events for ^{100}Mo with the half-life $T_{1/2} = 7.2 \times 10^{18}$ yr.

This work reports on a new independent observation of the $2\beta(2\nu)$ decay of ^{100}Mo in an experiment with liquid ionization chambers. In addition, the current average (world) value of the ^{100}Mo half-life and the corresponding value of the NME for the $2\beta(2\nu)$ transition are presented.

The experiment was carried out at the Gran Sasso Underground Laboratory (Italy) at a depth of 3500 m w.e. The setup consists of a liquid-argon multisection ionization chamber placed in a passive shield (15-cm lead, 1-cm boric acid, and 25-cm water), a gas system, and electronics. The detecting part of the ionization chamber is comprised of identical measuring sections. Each such section is composed of two twin ionization chambers with shielding grids and a common anode. Cathodes were fabricated from molybdenum foil ~50 mg/cm^2 in thickness. Eight and six cathodes were made from enriched (98.4% ^{100}Mo) and natural (9.6% ^{100}Mo) molybdenum, respectively.[2] The natural-molybdenum and molybdenum-enriched cathodes alternate with each other. The activity of radioactive impurities in the molybdenum samples does not exceed 0.015, 0.0015, and 0.04 Bq/kg for ^{214}Bi, ^{208}Tl, and ^{234m}Pa, respectively. The total weight of ^{100}Mo under investigation is equal to 306 g. The chamber includes 14 cathodes, 15 anodes, and 28 shielding grids. An ionization signal is picked off each anode using a charge-sensitive preamplifier, an amplifier, and an amplitude-to-digital converter with a step of 50 ns (15 independent electronic channels). The energy resolution is 6% (FWHM) for an energy of 3 MeV. The appearance of a signal exceeding 0.8 MeV at least in one channel serves as a trigger. As the trigger fires, information from all 15 channels is recorded on a magnetic tape. This information was processed in the off-line regime. Two-electron events were selected (i.e., events with signals in neighboring channels and with a time interval between them shorter than 0.6 μs). The efficiency of detecting the useful events was calculated by the Monte Carlo method. The setup and the method of data acquisition and processing are described in detail in [16–18].

This work presents the results obtained with 137.8 and 306 g of ^{100}Mo (313 and 2706 h of measurements, respectively). Figure 1 shows the total spectra of two-electron events for (a) enriched (848.2 kg h) and (b) natural (592.9 kg h) molybdenum. The thresholds for the first and second electrons are 0.8 and 0.5 MeV, respectively. The events in the sections with natural molybdenum were used to estimate the external and internal backgrounds.

0ν decay. To reduce the background, the energy threshold for each electron in a pair was, in this case, taken to be 1 MeV. The energy range 2.8–3.1 MeV was studied, where the ionization signals were additionally selected according to the pulse shape. As a result, 6 and 4 candidate events were selected in the molybdenum-enriched and natural-molybdenum samples, respectively (5.8 events in the natural molybdenum when recalculated to 848.2 kg h). With account taken of the efficiency (6.9%) of detecting useful events, the following bound on the neutrinoless 2β decay of ^{100}Mo was

[2] At the first stage of measurements, only four cathodes were manufactured from enriched molybdenum (the total weight of ^{100}Mo was equal to 137.8 g in this case).

The ^{100}Mo decay period through the 2β(2ν) channel

Year, reference	$T_{1/2}^{2\nu}$, $\times 10^{18}$ yr
1991 [11]	$11.5^{+3.0}_{-2.0}$
1995 [13]	$9.5 \pm 0.4(stat) \pm 0.9(syst)$
1997 [14]	$7.6^{+2.2}_{-1.4}$
1997 [15]	$6.75^{+0.37(stat)}_{-0.42(stat)} \pm 0.68(syst)$
2001, this work	$7.2 \pm 0.9(stat) \pm 1.8(syst)$
Average value	8.0 ± 0.7

obtained: $T_{1/2} > 8.4(4.9) \times 10^{21}$ yr with C.L. of 68%(90%).

$0\nu\chi^0$ decay. The energy thresholds for electrons in a two-electron event were taken to be 0.8 and 0.5 MeV. The energy range 2.3–3.0 MeV was examined. A total of 1613 and 1577 events in the molybdenum-enriched and natural-molybdenum samples were detected, respectively (when recalculated to 848.2 kg h). With account taken of the efficiency (5.7%) of detecting useful events, the following bound on the 2β decay of ^{100}Mo with majoron emission was obtained: $T_{1/2} > 4.1(3.2) \times 10^{20}$ yr with a C.L. of 68%(90%).

2ν decay. The events in the energy range 1.4–2.4 MeV were analyzed, where the signal-to-background ratio is maximal. After subtraction of the background, the number of useful events was 1140 ± 146. With the detection efficiency (2.2%) calculated for the 2β(2ν) events, the following half-life value was obtained:

$$T_{1/2} = [7.2 \times 0.9(stat) \pm 1.8(syst)] \times 10^{18} \text{ yr}.$$

The systematic error is determined by the possible contribution of the background events from the radioactive impurities in the molybdenum samples. The difference between the two-electron spectra of the molybdenum-enriched and natural-molybdenum samples is shown in Fig. 2. The curve in Fig. 2 is the spectrum calculated for the 2β(2ν) decay of ^{100}Mo with the half-life $T_{1/2} = 7.2 \times 10^{18}$ yr.

The table presents all of the presently available positive results of measuring the ^{100}Mo half-life. Only the preliminary results obtained by M. Moe *et al.* [12] are not presented, because we use their more accurate final result from [15].[3] The half-life averaged over all five experiments is given in the lower row. The average value was calculated using the standard procedure of determining the average for different-accuracy measurements (see, e.g., [20]), and the statistical and systematic errors were summed quadratically. Thus, the half-life value obtained for ^{100}Mo is one of the most accurate values among all nuclei undergoing 2β decay.

Using the obtained average half-life and the phase-space volume $G = 8.9 \times 10^{-18}$ yr^{-1} (for $g_A = 1.25$) [9], one can calculate the accurate value of NME(2ν) for the ^{100}Mo($0^+_{g.s.}$)–^{100}Ru($0^+_{g.s.}$) transition: $M_{GT} = (0.23 \pm 0.01)$ MeV^{-1} or, scaled by electron rest mass, $M_{GT} = (0.118 \pm 0.005)$.

[3] The result from [19], where the possibility of a considerable contribution to the observed effect from the background processes was not excluded, was also not used.

REFERENCES

1. H.V. Klapdor-Kleingrothaus and A. Staudt, *Non-accelerator Particle Physics* (Institute of Physics Publ., Bristol, 1995; Nauka, Moscow, 1997).
2. A. Faessler and F. Simkovic, J. Phys. G **24**, 2139 (1998).
3. H. V. Klapdor-Kleingrothaus, in *Proceedings of 5th International WEIN Symposium on Physics Beyond the Standard Model*, Ed. by P. Herczeg, C. M. Hoffman, and H. V. Klapdor-Kleingrothaus (World Scientific, Singapore, 1999), p. 275.
4. Y. Fukuda, T. Hayakawa, E. Ichihara, *et al.*, Phys. Rev. Lett. **81**, 1562 (1998).
5. Q. R. Ahmad, R. C. Allen, T. C. Andersen, *et al.*, Phys. Rev. Lett. **87**, 071301 (2001).
6. S. Stoica and H. V. Klapdor-Kleingrothaus, Nucl. Phys. A **694**, 269 (2001).
7. A. S. Barabash, Pis'ma Zh. Éksp. Teor. Fiz. **68**, 3 (1998) [JETP Lett. **68**, 1 (1998)].
8. A. S. Barabash, Eur. Phys. J. A **8**, 137 (2000).
9. J. Suhonen and O. Civitarese, Phys. Rep. **309**, 123 (1998).
10. F. Simkovic, G. Pantis, J. D. Vergados, and A. Faessler, Phys. Rev. C **60**, 055502 (1999).
11. H. Ejiri, K. Fushimi, T. Kamada, *et al.*, Phys. Lett. B **258**, 17 (1991).
12. S. R. Elliot, A. A. Hahn, and M. K. Moe, J. Phys. G **17**, S145 (1991).
13. D. Dassie, R. Eschbach, F. Hubert, *et al.*, Phys. Rev. D **51**, 2090 (1995).
14. M. Alston-Garnjost, B. L. Dougherty, R. W. Kenney, *et al.*, Phys. Rev. C **55**, 474 (1997).
15. A. De Silva, M. K. Moe, M. A. Nelson, and M. A. Vient, Phys. Rev. C **56**, 2451 (1997).
16. V. D. Ashitkov, A. S. Barabash, S. G. Belogurov, *et al.*, Yad. Fiz. **61**, 1002 (1998) [Phys. At. Nucl. **61**, 910 (1998)].
17. V. D. Ashitkov, A. S. Barabash, S. G. Belogurov, *et al.*, Nucl. Phys. B (Proc. Suppl.) **70**, 233 (1999).
18. V. D. Ashitkov, A. S. Barabash, S. G. Belogurov, *et al.*, Yad. Fiz. **62**, 2217 (1999) [Phys. At. Nucl. **62**, 2044 (1999)].
19. S. I. Vasil'ev *et al.*, Pis'ma Zh. Éksp. Teor. Fiz. **51**, 550 (1990) [JETP Lett. **51**, 622 (1990)].
20. Particle Data Group, Eur. Phys. J. C **15**, 10 (2000).

Translated by R. Tyapaev

JETP Letters, Vol. 74, No. 11, 2001, pp. 532–534. From Pis'ma v Zhurnal Éksperimental'noĭ i Teoreticheskoĭ Fiziki, Vol. 74, No. 11, 2001, pp. 605–607.

PJLZ Gauge-Fixing Approach in *SU*(2) Lattice Gauge Theory[1]

V. K. Mitrjushkin[1, 2, *] and A. I. Veselov[2, **]

[1] *Joint Institute for Nuclear Research, Dubna, Moscow region, 141980 Russia*

** e-mail: vmitr@thsunl.jinr.ru*

[2] *Institute of Theoretical and Experimental Physics, ul. Bol'shaya Cheremushkinskaya 25, Moscow, 117259 Russia*

*** e-mail: veselov@heron.itep.ru*

Received November 2, 2001

We study the *SU*(2) gauge theory with the interpolating gauge *a la* Parrinello–Jona–Lasinio–Zwanziger (PJLZ) with the gauge-fixing functional $F = \sum_{x\mu}\frac{1}{2}\mathrm{Tr}(U_{x\mu}\sigma_3 U^{\dagger}_{x\mu}\sigma_3)$. We find a strong indication of the nonanaliticity with respect to the interpolating parameter λ at $c \sim 0.8$. © *2001 MAIK "Nauka/Interperiodica".*

PACS numbers: 11.15.Ha

Gauge-variant objects, i.e., Green's functions for gluons and/or quarks, are among the most popular objects of study in continuum physics. A comparison of nonperturbatively calculated Green's functions on the lattice with continuum (mainly, perturbative) ones can give insight into the structure of the lattice theories and the role of nonperturbative effects. Another important point is that Green's functions are supposed to contain information about the physical "observables" which must not depend on the gauge chosen, e.g., dynamical gluon masses, screening masses, etc. Therefore, it is important to disentangle gauge-dependent features from the gauge-independent ones.

A somewhat special reason for studying the gauge, interpolating between no-gauge and maximally Abelian gauge (MAG), is associated with the fate of the so-called Abelian dominance. Recently, Ogilvie has shown [1] (see also [2]) that gauge fixing is unnecessary for Abelian projection (AP), i.e., AP without gauge fixing yields the exact string tension of the underlying non-Abelian theory: $\sigma_{Abel} = \sigma_{SU(2)}$.

These observations shed new light on the problem of Abelian dominance. Indeed, without MAG the Abelian projection ensures the exact equality between σ_{Abel} and $\sigma_{SU(2)}$, while with MAG Abelian σ_{Abel} and full $\sigma_{SU(2)}$ string tensions are close but not equal: $\sigma_{Abel} \neq \sigma_{SU(2)}$, at least, for β values used (see, e.g., [3, 4]).

The question arises of whether it is possible to interpolate "smoothly" from the no-gauge case to the gauge-fixed case. The main goal of this work is to answer this question.

Gauge-fixing procedure and algorithm. We consider the pure gauge *SU*(2) theory with standard Wilson action $\beta S(U)$[5]. According to the PJLZ approach [6, 7], the average of any gauge-noninvariant functional $\mathbb{O}(U)$ is given by

$$\langle\mathbb{O}\rangle = \frac{1}{Z}\int [dU]\tilde{\mathbb{O}}(U;\lambda)e^{-\beta S(U)}, \tag{1}$$

where $\tilde{\mathbb{O}}(U;\lambda) = \langle\mathbb{O}\rangle_\Omega$ and

$$\langle\mathbb{O}\rangle_\Omega = \frac{1}{I(U;\lambda)}\int [d\Omega]\mathbb{O}(U^\Omega)e^{\lambda F(U^\Omega)};$$
$$I(U;\lambda) = \int [d\Omega]e^{\lambda F(U^\Omega)}, \tag{2}$$

where $F(U)$ is the gauge-fixing functional and $U^\Omega_{x\mu} = \Omega_x U_{x\mu}\Omega^{\dagger}_{x+\mu}$. We have chosen

$$F = \sum_{x\mu}\frac{1}{2}\mathrm{Tr}(U_{x\mu}\sigma_3 U^{\dagger}_{x\mu}\sigma_3). \tag{3}$$

In Eq. (2), the functional $F_U(\Omega)$ plays the role of effective action with unitary "spins" Ω_x and random bonds described by fields $U_{x\mu}$ (similar to spin-glass model).

Evidently, the maximization of $F(U^\Omega)$ with respect to gauge transformations Ω defines MAG, and for the gauge-invariant functional $\tilde{\mathbb{O}}(U;\lambda) = \mathbb{O}(U;\lambda)$.

In Eqs. (2), λ is some "interpolating" parameter between 0 and ∞. The choice $\lambda = 0$ corresponds to the no-gauge case and the limit $\lambda \longrightarrow \infty$ corresponds to the case of the maximally Abelian gauge. Any physical, i.e., gauge-invariant, observable (screening masses, etc.) must not depend on λ. In general, there are no grounds for saying that one value of λ is more physical than the other one. However, the situation can be different in the case of the Abelian projection if $\lambda = 0$ and $\lambda = \infty$ belong to two different phases.

[1] This work was submitted by the authors in English.

In our study, we use $\mathbb{O} = F(U)$ defined in Eq. (3) and $F_{norm}(U) = F(U)/4V_4$. In the "strong coupling" approximation ($\lambda \sim 0$) one obtains

$$\langle F_{norm}\rangle_{str} = \lambda/3 + \ldots, \quad (4)$$

where V_4 is the number of sites.

Definitions in Eqs. (1) and (2) presume the following numerical algorithm [8].

(i) Generation of a set of link configurations $\{U^{(1)}_{x\mu}\}$, $\{U^{(2)}_{x\mu}\}$, … using a standard gauge-invariant algorithm with Wilson action $S(U)$ for some value of β.

(ii) Generation, for every configuration $\{U^{(i)}_{x\mu}\}$, of a sequence of configurations $\{\Omega^{(1)}_x\}$, $\{\Omega^{(2)}_x\}$, … weighted by the factor $\exp(\lambda F(U^{\Omega}))$ for some value of λ. Therefore, one obtains the estimator for $\tilde{\mathbb{O}}(U; \lambda) = \langle \mathbb{O}\rangle_{\Omega}$

$$\tilde{\mathbb{O}}(U; \lambda) = \frac{1}{N_\Omega}\sum_{j=1}^{N_\Omega} \mathbb{O}(U^{\Omega^{(j)}}). \quad (5)$$

(iii) The estimator for the expectation value $\langle \mathbb{O}\rangle$ is obtained as

$$\langle \mathbb{O}\rangle = \frac{1}{N_U}\sum_{i=1}^{N_U} \tilde{\mathbb{O}}(U^{(i)}; \lambda). \quad (6)$$

Numerical results. Most of our calculations were performed on an 8^4 lattice for $\beta = 2.4$. Some calculations were done also on 6^4 and 10^4 lattices to control finite-volume effects.

In Fig. 1, one can see the dependence of the $\langle F_{norm}\rangle$ on λ at $\beta = 2.4$. The dashed line correspondes to the lowest-order strong coupling approximation $\langle F\rangle_{strong} = \lambda/3$. The upper dotted line corresponds to the maximally Abelian gauge. The agreement between the numerical data and strong coupling expansion in Eq. (4) is very good up to $\lambda \simeq 0.6$. $\langle F_{norm}\rangle$ shows a clearly defined change in regime at $\lambda \sim 0.8$. It is interesting to note that this dependence is very similar to that occurring for another choice of the functional $F = F_{LG}$ [8], which corresponds to the Lorentz (or Landau) gauge at infinite values of the interpolating parameter.

For any $\{U_{x\mu}\}$ configuration, the "specific heat" $C(U; \lambda)$ is defined as

$$C_U(\lambda) = \frac{1}{4V_4}\frac{d\tilde{F}(U; \lambda)}{d\lambda} = \frac{\langle F^2\rangle_\Omega - \langle F\rangle^2_\Omega}{4V_4}. \quad (7)$$

In Fig. 2, we show the dependence of $C_U(\lambda)$ on λ for some typical configuration $\{U_{x\mu}\}$. One can see a sharp peak (cusp) at $\lambda_c \sim 0.8$. Of course, the position and size of this peak depend on the choice of configuration.

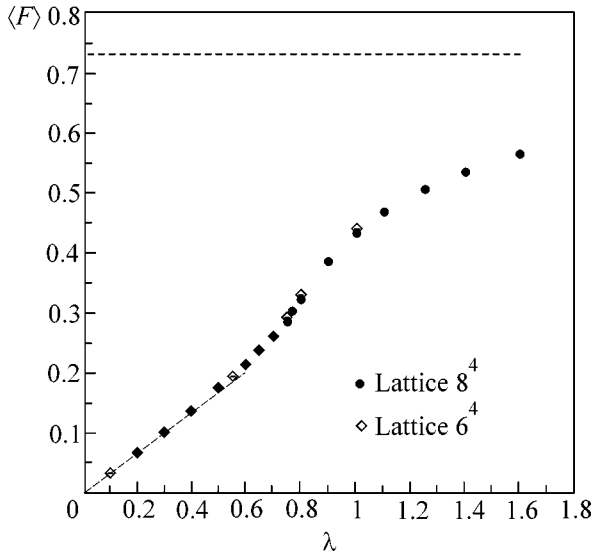

Fig. 1. The dependence of $\langle F_{norm}\rangle$ on λ. Symbols are explained in the text.

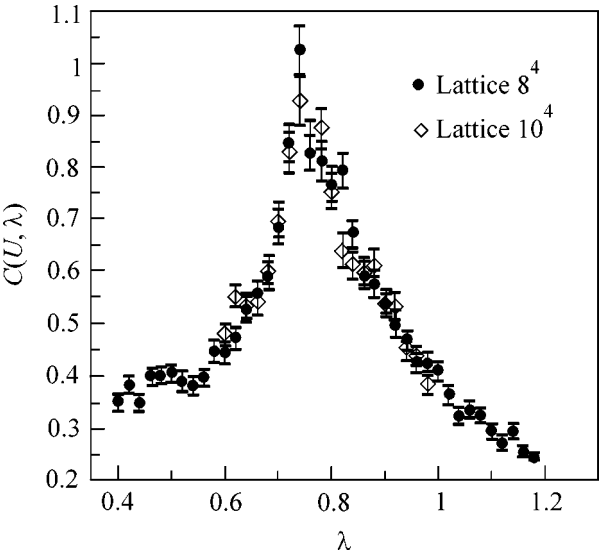

Fig. 2. The dependence of $C(U; \lambda)$ on λ for some typical configuration $\{U_{x\mu}\}$.

However, this peak demonstrates a rather weak dependence on the volume (compare 8^4 and 10^4 data).

Let us define the variance $\sigma(F)$ in a standard way:

$$\sigma^2(F) = \frac{1}{N_U}\sum_i^{N_U} \tilde{F}_i^2 - \left(\frac{1}{N_U}\sum_i^{N_U} \tilde{F}_i\right)^2. \quad (8)$$

Figure 3 demonstrates the dependence $\sigma(F)$ on λ for 8^4 lattice. For comparatively small values of λ, i.e., tail values $\lambda \lesssim 0.6$, where the strong coupling approximation for $\langle F\rangle$ works well, this variance is practically sta-

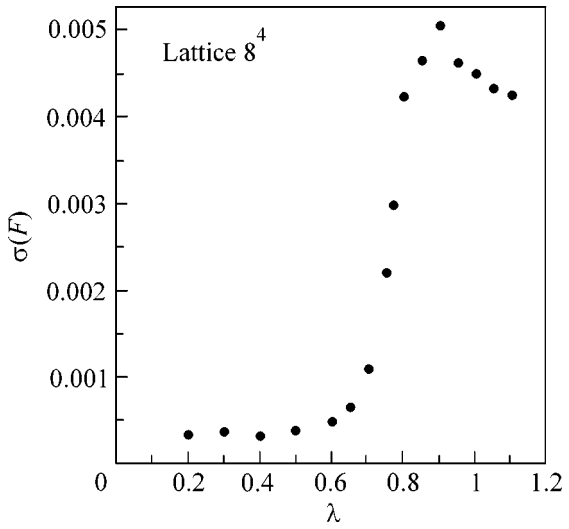

Fig. 3. The dependence of $\sigma(F)$ on λ.

ble. However, for λ's between 0.65 and 0.8 one can see a drastic increase in the variance.

To summarize, we have performed an exploratory study of the pure gauge $SU(2)$ theory with the interpolating gauge *a la* Parrinello–Jona–Lasinio–Zwanziger with the gauge-fixing functional defined in Eq. (3). Therefore, this gauge interpolates between the no-gauge case and the maximally Abelian gauge.

Our data indicate the existence of a strong nonanalyticity with respect to λ (phase transition) at $\lambda_c \sim 0.8$. Most probably, the mechanism of this transition is similar to that in the spin-glass models. At the moment, it is rather difficult to specify the order of this phase transition. It is interesting to note that the existence of a transition with respect to the interpolating parameter λ was also found for another choice of the functional $F = F_{LG}$ [8], which corresponds to the Lorentz (or Landau) gauge at infinite values of λ.

The existence of this transition makes it clear that there is no smooth interpolation between the no-gauge case and the case with MAG. This observation is of importance for gauge-dependent objects (e.g., σ_{abel}), especially taking into account that the Abelian projection $\{U_{x\mu}\} \longrightarrow \{h(U_{x\mu})\}$ is an (not very well controllable) approximation. We conclude that the "physics" of Abelian projection is assumed to be different at $\lambda = 0$ (where $\sigma_{abel} = \sigma_{SU(2)}$) and the case with MAG.

The above conclusion needs further confirmation. Finite-volume effects, as well as the dependence of other observables (e.g., σ_{abel}) on λ, should be given more attention. The corresponding work is in progress.

This work was supported in part by the INTAS (grant no. 00-00111) and the Russian Foundation for Basic Research (project nos. 99-01-01230 and 01-02-17456).

REFERENCES

1. M. C. Ogilvie, Phys. Rev. D **59**, 074505 (1999).
2. M. Faber, J. Greensite, and S. Olejnik, J. High Energy Phys. **01**, 008 (1999); hep-lat/9810008; J. Ambjorn and J. Greensite, J. High Energy Phys. **05**, 004 (1998).
3. J. D. Stack and W. W. Tucker, Nucl. Phys. (Proc. Suppl.) **94**, 529 (2001); hep-lat/0011034.
4. V. G. Bornyakov, D. A. Komarov, M. I. Polikarpov, and A. I. Veselov, Pis'ma Zh. Éksp. Teor. Fiz. **71**, 333 (2000) [JETP Lett. **71**, 231 (2000)].
5. K. Wilson, Phys. Rev. D **10**, 2445 (1974).
6. C. Parrinello and G. Jona-Lasinio, Phys. Lett. B **251**, 175 (1990).
7. D. Zwanziger, Nucl. Phys. B **345**, 461 (1990).
8. D. S. Henty, O. Oliveira, C. Parrinello, and S. Ryan, Phys. Rev. D **54**, 6923 (1996).

JETP Letters, Vol. 74, No. 11, 2001, pp. 535–538. From Pis'ma v Zhurnal Éksperimental'noĭ i Teoreticheskoĭ Fiziki, Vol. 74, No. 11, 2001, pp. 608–611.

Solitons in a Disordered Anisotropic Optical Medium[1]

M. Chertkov[1], I. Gabitov[1], I. Kolokolov[2], and V. Lebedev[3, *]

[1] *Theoretical Division, LANL, Los Alamos, NM 87545, USA*

[2] *Budker Institute of Nuclear Physics, Siberian Division, Russian Academy of Sciences, pr. Akademika Lavrent'eva 11, Novosibirsk, 630090 Russia*

[3] *Landau Institute for Theoretical Physics, Russian Academy of Sciences, ul. Kosygina 2, Moscow, 117334 Russia*

**e-mail: lwlebede@yahoo.com*

Received October 29, 2001

The radiation-mediated interaction of solitons in a one-dimensional nonlinear medium (optical fiber) with birefringent disorder is shown to be independent of the separation between solitons. The effect produces a potentially dangerous contribution to the signal lost. © *2001 MAIK "Nauka/Interperiodica".*

PACS numbers: 42.65.Tg; 42.81.Dp

The propagation of a pulse through an optical fiber with randomly varying anisotropy is usually addressed in the context of the Polarization Mode Dispersion (PMD). PMD is signal broadening caused by inhomogeneity of the medium birefringence. In the linear case, the study of PMD was pioneered by Poole [1], who showed that the pulse broadens as the two principal states of polarization split under the action of the random birefringence (see also [2]). Mollenauer *et al.* have numerically studied a nonlinear model of birefringent disorder in [3], where it was shown that a soliton, launched into the birefringent fiber, does not split, but it does undergo spreading [3] (see also [4]). In this letter, we develop an analytical approach and confirm that a single soliton does degrade due to disorder in the birefringence. The degradation is observable once the soliton traverses the distance $z_{\rm degr} \sim D^{-1}$, where D stands for the strength of the noise in the birefringence, measured in units of the soliton width and period ($D \ll 1$ is assumed, the typical case for telecommunication fibers).

The *major* finding of this letter is a new phenomenon which occurs on scales much shorter than $z_{\rm degr}$. We report that the interaction between solitons induced by their combined radiation (generated by disorder) is an important factor affecting the soliton dynamics. Initially stationary solitons experience a relative acceleration, $\sim D$. The intersoliton separation changes on the order of the soliton width at $z_{\rm int} \sim 1/\sqrt{D} \ll z_{\rm degr}$. We use and generalize here an approach developed previously to describe solitons interacting in an isotropic medium with fluctuating dispersion [5]. The soliton interaction, in the case of [5], decays algebraically. By contrast, in the anisotropic case discussed in this letter, the interaction is separation-independent. The reason is that, in this case, a different type of wave scatters from the solitons. In the isotropic case, the scattering of the radiated waves, emitted by a soliton, by another soliton is not refracted. In the anisotropic case, radiation from one soliton pushes (literally) the other soliton, because the scattering potential is not transparent.

Let us briefly formulate the problem. The electric field $\mathbf{E}$, corresponding to a wave packet carrying frequency ω, can be decomposed into complex components $\mathbf{E} = 2\,\mathrm{Re}[\mathbf{E}_\omega \exp(ik_0 z - i\omega t)]$, where z is the coordinate along the fiber. Concomitant averaging over fast oscillations and over the structure of fundamental mode (a monomode regime is assumed) constitutes the coarse-grained description for the signal envelope described by the two-component complex field Ψ_α, $\bar{\mathbf{E}}_\omega = \Psi_1(z)\mathbf{e}_1 + \Psi_2(z)\mathbf{e}_2$, where $\mathbf{e}_{1,2}$ are unit vectors orthogonal to each other and to the waveguide direction. The averaging results in the envelope equation [6, 7]

$$i\partial_z \Psi_\alpha - \Delta_{\alpha\beta}\Psi_\beta - im_{\alpha\beta}\partial_t \Psi_\beta + \partial_t^2 \Psi_\alpha + \frac{4}{3}(|\Psi_1|^2 + |\Psi_2|^2)\Psi_\alpha + \frac{2}{3}(\Psi_1^2 + \Psi_2^2)\Psi_\alpha^* = 0. \quad (1)$$

Here, the wave packet is subjected to dispersion in retarded time t and to the Kerr nonlinearity, which is described by the last two terms on the left-hand side of (1). The matrix $\hat{\Delta}$ describes the differences in the wavevectors. The matrix $\hat{m}$ describes the anisotropy in the group velocity for the two distinct states of polarization (of the respective linear problem). The isotropy is broken in Eq. (1), because the core of any fiber is elliptic rather than circular in cross section. It is assumed in Eq. (1) that the dispersion term and the nonlinear term are isotropic, since in real fibers anisotropy of dispersion and nonlinearity is usually less important than the

[1] This work was submitted by the authors in English.

effects of anisotropy described by the matrices $\hat{\Delta}$ and $\hat{m}$. The coefficients of nonlinearity and dispersion are rescaled to unity; i.e., t and z are already dimensionless in Eq. (1). If the matrices $\hat{\Delta}$ and $\hat{m}$ are zero, the full problem is isotropic and Eq. (1) supports the constant polarization solution, e.g., $\Psi_2 = 0$. Then, the equation for Ψ_1 is the scalar nonlinear Shrödinger (SNLS) equation. The self-conjugate matrix $\hat{\Delta}$ is traceless, since the trace can be excluded by a simple phase transformation. The (also self-conjugate) matrix $\hat{m}$ is traceless, as Eq. (1) is written in the reference frame moving with the mean group velocity. Both $\hat{\Delta}$ and $\hat{m}$ may contain regular and disordered parts. In a polarization-maintaining fiber, at least one of the regular parts is nonzero. If the phase change between the two polarizations caused by a regular part (say $\hat{\Delta}_{\text{reg}}$) becomes ~1 on a scale z_{reg}, an additional averaging over the distances larger than z_{reg} reduces Eq. (1) to [6, 7]

$$(i\partial_z + \partial_t^2 + 2|\Psi_1|^2 + 2\varepsilon|\Psi_2|^2)\Psi_1 = (\Delta_{1\beta} + im_{1\beta}\partial_t)\Psi_\beta, \tag{2}$$

and analogously for Ψ_2. The quantities $\hat{\Delta}$ and $\hat{m}$ left in Eq. (2) represent random contributions. Generically, eigenvectors of $\hat{\Delta}_{\text{reg}}$ correspond to elliptic polarizations, and the corresponding eigenvalues are complex. The quantity ε in Eq. (2) measures the degree of ellipticity, $2/3 \le \varepsilon \le 2$. In the degenerate limit of linear polarization (the eigenvectors are real), $\varepsilon = 2/3$. Subsequent analysis is devoted to models (1) and (2) with $\hat{\Delta} = 0$ and random zero mean $\hat{m}$. The anisotropy matrix $\hat{m}$ can be written in terms of Pauli matrices as follows: $\hat{m} = \sum_k h_k(z)\hat{\sigma}_k$, where $k = 1, 2, 3$ and the real field h_k is a function of z only because the disorder is frozen in the fiber. The correlation scale of the random field $h_j(z)$ is short. (It is typically constrained by the process of fiber pulling from a silica preform, cabling, and spooling into a bobbin). Therefore, according to the central limit theorem, $h_j(z)$ on the larger scales can be treated as a Gaussian random process. The noise intensity is described by the matrix $\hat{D}$, $D_{ik} = \int dz \langle h_i(z)h_k(z')\rangle$. One assumes that the isotropy is restored on average, $D_{ik} \propto \delta_{ik}$. Then, the statistics of $\hat{m}$ is characterized by

$$\langle h_i(z_1)h_k(z_2)\rangle = D\delta_{ik}\delta(z_1 - z_2). \tag{3}$$

Similarly, one assumes that $\hat{\Delta} = \sum_k b_k(z)\hat{\sigma}_k$ and $\langle b_i(z_1)b_k(z_2)\rangle = D_b\delta_{ik}\delta(z_1 - z_2)$.

We start with the single-soliton story. One looks for a solution to Eq. (1) or (2) in the form

$$\Psi_\alpha = \delta_{1\alpha}\exp(iz)\cosh^{-1}t + v_\alpha. \tag{4}$$

For $v_{1,2} = 0$, Eq. (4) represents a single-soliton solution of the ideal, $\hat{m} = 0$, problem. If the disorder is weak, one can substitute Eq. (4) into Eq. (1) or (2) and linearize with respect to $v_{1,2}$ to get

$$(\partial_z - i\hat{L}_{1,2})\begin{pmatrix} v_{1,2} \\ v_{1,2}^* \end{pmatrix} = \begin{pmatrix} R_{1,2} \\ R_{1,2}^* \end{pmatrix}\frac{\tanh t}{\cosh t} + \begin{pmatrix} Q_{1,2} \\ Q_{1,2}^* \end{pmatrix}\frac{1}{\cosh t}, \tag{5}$$

where $R_1 = h_3$, $R_2 = h_1 + ih_2$, $Q_1 = ib_3$, $Q_2 = ib_1 - b_2$, and $\hat{L}_{1,2}$ are differential (second order in t) operators of the linear Schrödinger type with soliton-shaped ($\propto 1/\cosh$) potentials. It is convenient to expand $v_{1,2}$ in series in eigenfunctions of the operators $\hat{L}_{1,2}$. Spectra of the operators are separated into continuous and discrete parts, $v_{1,2} = v_{1,2}^{(0)} + \tilde{v}_{1,2}$. The four zero modes of $\hat{L}_1$ are related to variations of the soliton amplitude, position, phase, and phase velocity. There is also a localized eigenmode of $\hat{L}_2$ identified with variations of the soliton polarization. In the case of model (1), the polarization eigenmode becomes a zero mode of $\hat{L}_2$ corresponding to the free rotation of polarization axes and an additional zero mode appears that is related to ellipticity. Some localized modes are subjected to the linear, first-order, in disorder response. Thus, the position of the soliton y varies randomly in z: $\langle y^2\rangle = Dz$. Second-order effects in radiation lead to variations of the soliton amplitude η. From the conservation law, which accounts for the balance of "energy" among the soliton and the continuous radiation ($v_{1,2} = 0$ at $z = 0$ is assumed), one derives $\tilde{D}\int_0^z dz'\eta^3(z') = 1 - \eta$, where the left- and right-hand sides represent, respectively, the radiative and the soliton contributions to the energy balance, and $\tilde{D} \sim D$. The solution to the integral equation, valid at any z, is

$$\eta = (1 + 2\tilde{D}z)^{-1/2}. \tag{6}$$

[Note that the single-soliton radiation in the degenerate case of Eq. (2) with $\varepsilon = 1$ was studied in [8], where analogues of the aforementioned integral equation were derived. The equation was analyzed in [8] under the assumption that $zd\eta/dz \ll 1$, which led to the answer that the soliton amplitude degradation valid at $zD \ll 1$ only, where it coincides with Eq. (6)].

We now turn to the multisoliton case. Only scales shorter than $z_{\text{degr}} = 1/D$ are discussed, so the random walk of y and the degradation of the soliton amplitude can be neglected. The same argument applies to the polarization angle ϕ in the case of model (2). In the isotropic model case (1), the jitter of ϕ becomes important

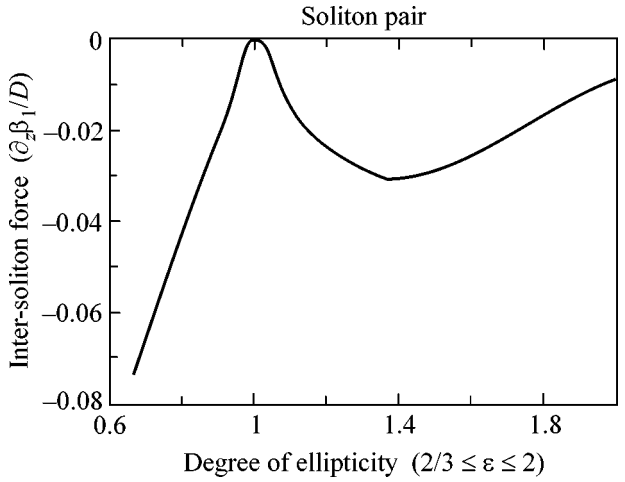

Fig. 1. Two solitons. Intersoliton force vs. degree of ellipticity.

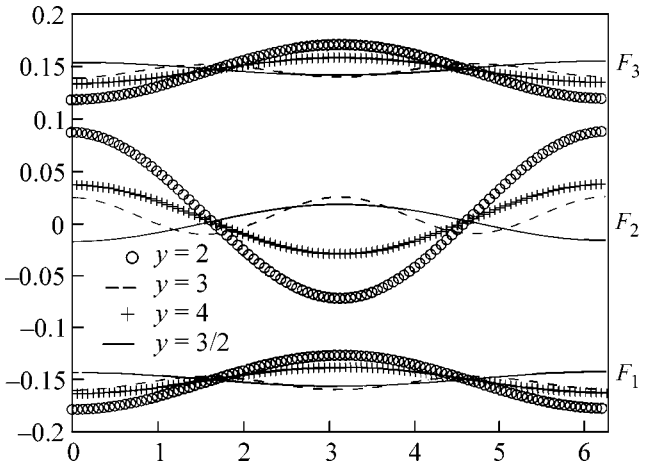

Fig. 2. Three solitons. Forces vs. intersoliton phase mismatch.

at $z_\phi \sim 1/D^{1/3}$. The effect, however, is collective: polarizations of different solitons rotate through the same angle, so that the relative polarization angle is unchanged at $z \ll z_{\text{degr}}$. We consider the N-soliton solution,

$$\Psi_\alpha = \sum_{j=1}^{N} \exp[i\alpha_j + i\beta_j(t-y_j)]\cosh^{-1}(t-y_j)\delta_{1\alpha} + v_\alpha$$

of Eqs. (1) and (2). One derives (and solves) the generalization of Eq. (5) and equations for the slow variables y_i, α_i, and β_i, keeping in the latter the terms up to the second order in v. Direct averaging of the slow modes over the h-statistics is the next step. At $z \ll z_{\text{degr}}$, the relative phases $\alpha_i - \alpha_j$ do not change, while the soliton positions y_j and phase velocities β_i evolve according to

$$\partial_z y_j = -2\beta_j, \quad \partial_z \beta_j = F_j,$$
$$F_j = \int dt U(t)\tanh(t-y_j)\cosh^{-2}(t-y_j), \tag{7}$$

where $U(t)$ is a quadratic form of $\tilde{v}$, $U(t) = 4|\tilde{v}_1|^2 + \tilde{v}_1^2 + \tilde{v}_1^{*2} + 2\varepsilon|\tilde{v}_2|^2$ for model 2. The force F_j acting on the soliton is self-averaged at $z \gg 1$. Therefore, we come to a set of deterministic (like in classical mechanics) equations for the soliton positions and the phase velocities (the latter play the role of classical momenta). The general setting is familiar from [5]. However, the dependence of the intersoliton forces on the separation between the solitons in the polarization problems is different: the force does not depend on the separation. The key feature of the polarization problems is the refractive nature of $\hat{L}_2$, which is closely related to the nonintegrability of the no-disorder ($\hat{m} = 0$) problem in both of our settings (1), (2). This is in contrast to the integrability of SNLS, which is the no-disorder limit of the scalar problem. Due to nonzero refraction, standing waves are formed in between the solitons in such a way that the wave amplitude does not depend on the intersoliton separation.

We present here quantitative results for model (2), obtained by numerical evaluation of the integral in Eq. (7) [with $U_{1,2}$ found via analytical integration of the generalized version of Eq. (5) and averaged over Eq. (3)]. A description of the calculation details will be published elsewhere. The y-independent $O(D)$ contribution to the intersoliton force for the two-soliton pattern is shown in Fig. 1. The force is independent of the phase mismatch, $\alpha_1 - \alpha_2$. It is always negative (the solitons repel). The minimum value of the force is achieved at the boundary value, $\varepsilon = 2/3$. The separation-independent contribution is zero at $\varepsilon = 1$. This corresponds to transparent scattering, for the no-disorder limit is integrable in this case [9]. The independence of the force of the overall size of the soliton pattern persists in the multisoliton case, although a new feature—sensitivity to the phase mismatches—emerges. The dependence of the forces in the three-soliton pattern on the phase mismatch, in the special case $\alpha_2 = 0$, $\alpha_3 = -\alpha_1 = \alpha$, and $\epsilon = 2/3$, for various values of the relative separation, $y = (y_3 - y_2)/(y_2 - y_1)$, is shown in Fig. 2. In the "symmetric" case, $y = 1$, $F_2 = 0$, while $F_3 = -F_1$, and the value is twice as large as the force acting on the second particle in the two-soliton case. In all other $y \neq 1$ situations, the forces do depend on α. The values of the forces oscillate about the symmetric ($y = 1$) values.

To conclude, we have shown that the major destructive factor for a set of well-separated pulses in random birefrengent fibers is due to soliton–soliton interaction mediated by radiation. Note that the analytical method described in this paper can easily be generalized to a variety of more complicated sources of anisotropy in optical fibers.

We are grateful to G.D. Doolen, E.A. Kuznetsov, and V.E. Zakharov for useful comments. This work was supported by the LDRD ER on "Statistical Physics of Fiber Optics Communications" at LANL, the J. R. Oppenheimer fellowship (MC), the DOE (contract W-7-405-ENG-36) and its Program in AMS [KJ-01-01 (IG)], the Russian Foundation for Basic Research (project no. 00-02-17652), and the Russian Foundation for Promoting Science Personal Grant (IK).

REFERENCES

1. C. D. Poole, Opt. Lett. **13**, 687 (1988); **14**, 523 (1989); C. D. Poole, J. H. Winters, and J. A. Nagel, Opt. Lett. **16**, 372 (1991).
2. N. Gisin and J. P. Pellaux, Opt. Commun. **89**, 316 (1992).
3. L. F. Mollenauer *et al.*, Opt. Lett. **14**, 1219 (1989).
4. P. K. A. Wai, C. R. Menyuk, and H. H. Chen, Opt. Lett. **16**, 1231 (1991); **16**, 1735 (1991).
5. M. Chertkov, I. Gabitov, I. Kolokolov, and V. Lebedev, Pis'ma Zh. Éksp. Teor. Fiz. **74**, 391 (2001) [JETP Lett. **74**, 357 (2001)].
6. A. L. Berkhoer and V. E. Zakharov, Zh. Éksp. Teor. Fiz. **58**, 903 (1970) [Sov. Phys. JETP **31**, 486 (1970)].
7. C. R. Menyuk, IEEE J. Quantum Electron. **25**, 2674 (1989).
8. T. I. Lakoba and D. J. Kaup, Phys. Rev. E **56**, 6147 (1997); M. Matsumoto, Y. Akagi, and A. Hasegawa, J. Lightwave Technol. **15**, 584 (1997); L. F. Mollenauer *et al.*, in *Optical Fiber Telecommunications*, Ed. by I. P. Kaminow and T. L. Koch (Academic, San Diego, 1997), Part IIIA; H. H. Chen and H. A. Haus, Opt. Lett. **25**, 290 (2000).
9. S. V. Manakov, Zh. Éksp. Teor. Fiz. **65**, 505 (1973) [Sov. Phys. JETP **38**, 248 (1974)].

JETP Letters, Vol. 74, No. 11, 2001, pp. 539–542. Translated from Pis'ma v Zhurnal Éksperimental'noĭ i Teoreticheskoĭ Fiziki, Vol. 74, No. 11, 2001, pp. 612–615.

Cooperative Quenching Kinetics: Theory and Monte-Carlo Simulation

I. T. Basieva, K. K. Pukhov*, and T. T. Basiev

Laser Materials and Technologies, Research Center of General Physics Institute, Russian Academy of Sciences, Moscow, 119991 Russia

**e-mail: pukhov@lst.gpi.ru*

Received May 29, 2001; in final form, October 31, 2001

Analytic expression is given for the static cooperative quenching kinetics in crystals with arbitrary acceptor concentration and arbitrary multipolarity of interaction. For the quenching by two acceptors, the results of Monte-Carlo simulation are also presented which can be approximated in the long-time domain by the nonexponential law $I(t) \cong \exp[-(wt)^k]$, with $k = 0.41$, 0.3, and 0.25 for the multipolarities $S = 6$, 8, and 10, respectively.

PACS numbers: 78.40.Fy; 71.55.-i; 61.72.Ss; 78.55.-m

Cooperative effects play an important role in the dynamic processes accompanying radiofrequency and optical pumping of materials doped with transition and rare-earth impurities, because these processes govern the sensitization and excitation relaxation processes, as well as the energy up- and down- conversion with excitation summation or splitting [1, 2].

To avoid association with superradiance [3, 4], note that in this work the term "cooperative" is related to the phenomena caused by the elementary incoherent processes occurring in several interacting particles (ions, atoms, or molecules). Among these are the excitation transfer from one donor to two acceptors (cooperative quenching); energy transfer from two excited donors to one acceptor (cooperative sensitization); cooperative absorption (absorption of a single photon by two particles; etc. [2, 5, 6].

After averaging over the ensemble of randomly distributed particles, the kinetics of resonant radiationless energy transfer from donor to acceptor becomes rather complex and nonexponential. For the dipole–dipole two-particle interactions, the kinetics was obtained in [7, 8] in the root-law form $I_D(t) \approx \exp(-\sqrt{wt})$. Later on, it was extended to higher multipolarities [9, 10], and it was found that $I_D(t) \approx \exp[-(wt)^{3/S}]$, where S is the interaction multipolarity: $S = 6$, 8, and 10 for the dipole–dipole, dipole–quadrupole, and quadrupole–quadrupole interactions, respectively. For crystals, where donors and acceptors with an arbitrary concentration are substitutional impurities, the exact solution was obtained in [11, 12].

In this work, we seek a solution for the ensemble-averaged kinetics of multiparticle interaction between a donor and two-, three-, and multiparticle (cooperative) acceptors.

The case where there is no resonance between a donor and a single acceptor but where the multipolar interaction is possible simultaneously with two or three particles (cooperative acceptors) was recently observed experimentally and examined in [13–15].

In this article, an analytic expression is given and the results of Monte-Carlo simulation are presented for the static cooperative quenching kinetics in crystals with an arbitrary acceptor concentration and the multipolarity $S = 6$, 8, and 10. In the long-time domain, these results can be approximated by the nonexponential law $I(t) \cong \exp[-(wt)^k]$, with $k = 0.41$, 0.3, and 0.25 for $S = 6$, 8, and 10, respectively.

Theory. Let W_{ij} be the excitation transition rate from one donor simultaneously to two acceptors occupying the ith and the jth lattice sites. The temporal excitation-decay kinetics of a donor ensemble is given by

$$n_2(t) = \left\langle \exp\left(-\sum_{i<j} W_{ij} t\right)\right\rangle. \qquad (1)$$

Here, the subscript *2* indicates the multiparticle (pair) character of acceptors in the elementary event of cooperative transfer; the symbol $\langle\ldots\rangle$ stands for the configurational averaging, i.e., averaging over all possible realizations of acceptor distribution over the lattice sites [11, 12]; and the symbol $\sum'$ signifies that the summation in Eq. (1) is taken over only the sites occupied by acceptors. Equation (1) can be written in the form

$$n_2(t) = \left\langle \prod_{i<j} [1 + p_i p_j \varphi_{ij}(t)]\right\rangle, \qquad (2)$$

where

$$\varphi_{ij} = \exp(-W_{ij}t) - 1, \quad (3)$$

and p_i is unity if the ith site is occupied by an acceptor and otherwise zero.

In what follows, it will be assumed that the acceptor distribution over the lattice sites is homogeneous:

$$\langle p_i \rangle = c, \quad (4)$$

$$\langle p_i p_j \rangle = \begin{cases} \langle p_i^2 \rangle = \langle p_i \rangle = c, & i = j \\ \langle p_i \rangle \langle p_j \rangle = c^2, & i \neq j. \end{cases} \quad (5)$$

An analogue of Eq. (1) in the well-known case of excitation transfer from a donor to a single-particle acceptor [7–12] is given by the expression

$$n_1(t) = \left\langle \prod_i [1 + p_i \varphi_i(t)] \right\rangle, \quad (6)$$

where

$$\varphi_i = \exp(-W_i t) - 1, \quad (7)$$

with W_i being the transition rate from a donor to an acceptor at the ith lattice site.

Taking into account relationships of type (5), one can replace the average of the products in Eq. (6) by the product of averages, i.e., perform decoupling

$$n_1(t) = \prod_i \langle 1 + p_i \varphi_i(t) \rangle = \prod_i [1 + \langle p_i \rangle \varphi_i(t)]. \quad (8)$$

Using Eq. (4), one arrives at the well-known expression [11, 12]

$$n_1 = \exp P_1(t) \quad (9)$$

with the exponent

$$P_1(t) = \sum_{i=1}^{N} \ln\{1 - c[1 - \exp(-W_i t)]\}. \quad (10)$$

In this expression, the summation is taken over all N lattice sites accessible to acceptors.

By applying a similar decoupling procedure to Eq. (1), one obtains for $n_2(t)$ the expression analogous to Eq. (9):

$$n_2 = \exp P_2(t), \quad (11)$$

where

$$P_2(t) = \sum_{i<j} \ln[1 + c^2 \varphi_{ij}(t)]. \quad (12)$$

Equation (12) properly describes the initial (exponential) portion of the decay curve:

$$\left(\frac{dn_2(t)}{dt}\right)_{t=0} = -c^2 \sum_{i<j} W_{ij}. \quad (13)$$

Note also that Eq. (12) is, evidently, valid for $c = 1$.

However, in the general case, one cannot replace the average of the products in Eq. (2) by the product of averages. This becomes clear even from the fact that the averages of the type $\langle (p_i p_j)(p_j p_k) \rangle = \langle p_i p_j p_k \rangle = c^3$ appear in Eq. (2) for any three acceptors i, j, and k ($i < j < k$). However, the decoupling of $\langle (p_i p_j)(p_j p_k) \rangle$ is equivalent to replacing them by $\langle (p_i p_j) \rangle \langle (p_j p_k) \rangle = c^4$. For this reason, the expansion of Eq. (12) in power series in concentration c does not contain terms with odd powers of c.

To derive the expression that is more correct than Eq. (12), let us rewrite Eq. (2) in the form

$$n_2(t) = \left\langle \prod_{j>1} (1 + p_1 p_j \varphi_{1j}) \prod_{j>2} (1 + p_2 p_j \varphi_{2j}) \times \prod_{j>3} (1 + p_3 p_j \varphi_{3j}) \times \ldots \right\rangle \quad (14)$$

and use the approximation

$$n_2(t) \approx \left\langle \prod_{j>1} (1 + p_1 p_j \varphi_{1j}) \right\rangle \times \left\langle \prod_{j>2} (1 + p_2 p_j \varphi_{2j}) \right\rangle \left\langle \prod_{j>3} (1 + p_3 p_j \varphi_{3j}) \right\rangle \times \ldots. \quad (15)$$

Such a "partial" decoupling results in the following expression for the kinetics of transfer to the pair cooperative acceptors:

$$n_2 = \exp P_2(t), \quad (16)$$

$$P_2(t) = \sum_{i=1}^{N-1} \ln\left\{1 - c\left[1 - \exp \sum_{j=i+1}^{N} \ln(1 + c\varphi_{ij})\right]\right\}. \quad (17)$$

For the excitation transfer to three-particle cooperative acceptors, a similar procedure leads to the expression

$$n_3 = \exp P_3(t), \quad (18)$$

where

$$P_3(t) = \sum_{i=1}^{N-2} \ln\left\{1 - c\left\{1 - \exp \sum_{j=i+1}^{N-1} \ln\left[1 - c \times \left[1 - \exp \sum_{k=j+1}^{N} \ln[1 + c\varphi_{ijk}(t)]\right]\right]\right\}\right\}, \quad (19)$$

$$\varphi_{ijk} = \exp(-W_{ijk}t) - 1, \quad (20)$$

and W_{ijk} is the transition rate simultaneously to three acceptors occupying the ith, jth, and kth lattice sites.

To generalize Eq. (18) to the case of energy transfer simultaneously to m (m = 4, 5, …) acceptors, one should use original Eqs. (16) and (18) and the following recurrent relation. Let us write $P_m(t)$ in the form

$$P_m = \sum_{i_1=1}^{N-m+1} P_m^{(i_1)}(t), \tag{21}$$

where $P_m^{(i_1)}(t)$ depends on the function

$$\sum_{i_m=i_{m-1}+1}^{N} \ln[1 + c\varphi_{i_1 i_2 \ldots i_m}(t)] \tag{22}$$

with $\varphi_{i_1 i_2 \ldots i_m} = \exp[-W_{i_1 i_2 \ldots i_m} t] - 1$ and $W_{i_1 i_2 \ldots i_m}$ being the transition rate to m particles forming the acceptor and occupying the sites i_1, i_2, …, i_m. Then $P_{m+1}(t)$ can be represented as

$$P_{m+1}(t) = \sum_{i_1=1}^{N-m} P_{m+1}^{(i_1)}(t), \tag{23}$$

where

$$P_{m+1}^{(i_1)} = \ln\left\{1 - c\left[1 - \exp\sum_{i_2=i_1+1}^{N-m+1} \tilde{P}_m^{(i_2)}(t)\right]\right\}, \tag{24}$$

and $\tilde{P}_m^{(i_2)}(t)$ is obtained from $P_m^{(i_2)}(t)$ through replacing the function

$$\sum_{i_m=i_{m-1}+1}^{N} \ln[1 + c\varphi_{i_1 i_2 \ldots i_m}(t)]$$

by the function

$$\sum_{i_{m+1}=i_m+1}^{N} \ln[1 + c\varphi_{i_1 i_2 \ldots i_{m+1}}(t)]$$

in the expression for $P_m^{(i_2)}(t)$.

Computer simulation of kinetics in face-centered cubic lattice. Let us consider the quenching kinetics for a particular model of two-particle cooperative acceptors in an fcc lattice, whose sites are randomly occupied by the acceptor and donor ions with concentrations c and c_D, respectively. We are interested in the case of zero interaction between the donor ions or, what is the same, absence of the energy migration over the donors (static regime). This program can easily be implemented in computer simulation by satisfying the condition $c_D \ll c$. The cooperative energy transition rate from one donor particle to a cooperative (two-particle) acceptor was taken in the same form as in [6] for the reverse process of cooperative energy summation from two particles by the third particle. For definiteness, W_{ij} was taken in the form

$$W_{ij} = \frac{a^{2S} W^0(R_{\min})}{3 \times 2^S} \times \left[\frac{1}{R_i^S R_j^S} + \frac{1}{R_{ij}^S}\left(\frac{1}{R_i^S} + \frac{1}{R_j^S}\right)\right], \tag{25}$$

where R_i is the separation between a donor and an acceptor particle at the ith site, R_{ij} is the separation between the acceptor particles at sites i and j, and a is the lattice constant.

To reduce all quantities to the dimensionless form, the cooperative transition rate was normalized to the transition rate $W^0(R_{\min})$ for the shortest possible distances between the three particles, one of which is a donor and the two others form a cooperative acceptor, so that $R_{DAi} = R_{DAj} = R_{AiAj} = R_{\min} = a/\sqrt{2}$, and time was normalized to the inverse quantity $t_0 = 1/W^0(R_{\min})$.

For different ion concentrations, the calculations of decay kinetics were carried out using Eq. (16), and the process was modeled by the Monte-Carlo method. The model size allowed 100 widely separated donors to be encompassed in computations. The quenching of each donor was influenced by an environment that included 344 different possible acceptor positions (the nearest 16 spheres), and the averaging was carried out over one hundred random configurations of the acceptor environment.

The results can conveniently be represented as log–log plots of intensity vs. logarithm of time.

Note that for small acceptor concentrations, $c < 0.01$, the kinetic curves calculated by Eq. (16) are similar to the computed curves but shifted relative to them by a certain constant value along the vertical axis, which is equivalent to multiplying by a constant factor.

To check for the correctness of the model, the simulation was carried out for some concentrations with inclusion of a larger number of spheres and 528 possible acceptor positions. The resulting curve had the same shape as in the case of simulation with a lower accuracy, but it was shifted along the vertical axis and became coincident at its initial portion with the curve calculated by Eq. (16).

The unity curve slopes in the short-time domain ($t < 0.1t_0$) suggests that, at small t, all curves are well described by the initial portion of exponential quenching. The corresponding quenching curve can be obtained analytically by substituting $c\varphi_{ij} \ll 1$ into Eq. (16) and subsequent first-order expansion.

At times much longer than t_0 and at small concentrations c, the simulated and calculated curve slopes also coincide with each other to within 10%. For example, one can see from the comparison of curves *1* and *2* in the figure that (for the dipolar interaction, S = 6, and

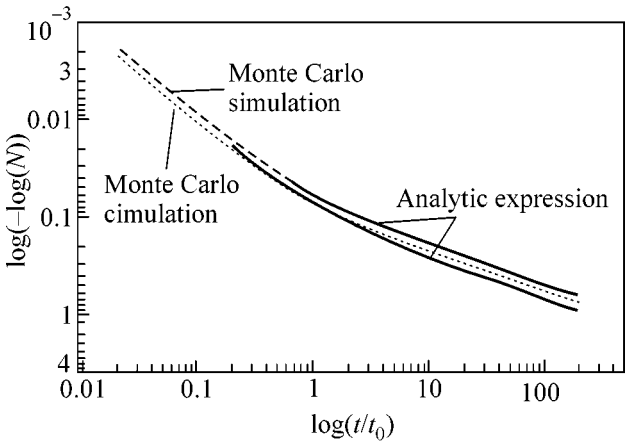

Excitation decay kinetics for the dipole–dipole transfer to two acceptors with a concentration of 0.05%.

acceptor concentration of 0.05%) the curves have the same shape. At the long-time decay stage ($t = 50t_0$), the curve slope calculated by Eq. (16) is equal to 0.43, while the simulation gives a value of 0.41. It is known from theory that the slope in the log–log plot of the decay curve reflects the exponent in which t enters the exponent of the expression for the nonexponential Förster kinetics [7]. In the standard model of quenching by single-particle acceptors, this exponent equals 0.5, while the kinetics has the form $\exp(-(wt)^{0.5})$ [7, 8].

As the concentration increases, the accuracy of computer simulation diminishes. However, the long-time behaviors of the curves modeled for different concentrations are well approximated by the straight lines with the following slopes: 0.41 for the dipole–dipole ($S = 6$) interaction ($\exp(-(wt)^{0.41}]$); 0.30 for the dipole–quadrupole ($S = 8$) interaction ($\exp(-(wt)^{0.3})$); and 0.25 for the quadrupole–quadrupole ($S = 10$) interaction ($\exp(-(wt)^{0.25})$).

This distinguishes them from the Förster decay kinetics $I(t) = \exp(-(wt)^{3/S})$ of a traditional one-particle quenching for an arbitrary multipolarity S [9, 10].

This work was supported by the CRDF, grant no. RP2-2257.

REFERENCES

1. A. A. Manenkov and A. M. Prokhorov, Zh. Éksp. Teor. Fiz. **42**, 75 (1962) [Sov. Phys. JETP **15**, 54 (1962)].
2. V. V. Ovsyankin and P. P. Feofilov, Izv. Akad. Nauk SSSR, Ser. Fiz. **37**, 262 (1973).
3. R. H. Dicke, Phys. Rev. **93**, 99 (1954).
4. L. Allen and J. H. Eberly, *Optical Resonance and Two-Level Atoms* (Wiley, New York, 1975; Mir, Moscow, 1978).
5. V. V. Ovsyankin and P. P. Feofilov, Pis'ma Zh. Éksp. Teor. Fiz. **4**, 471 (1966) [JETP Lett. **4**, 317 (1966)].
6. T. Kushida, J. Phys. Soc. Jpn. **34**, 1318 (1973); **34**, 1327 (1973); **34**, 1334 (1973).
7. Th. Förster, Zh. Naturforsch. A **4**, 321 (1949).
8. M. D. Galanin, Zh. Éksp. Teor. Fiz. **28**, 485 (1955) [Sov. Phys. JETP **1**, 317 (1955)].
9. B. Ya. Sveshnikov and V. I. Shirokov, Opt. Spektrosk. **12**, 5764 (1962).
10. M. Inokuti and F. Hirayama, J. Chem. Phys. **43**, 1978 (1965).
11. V. P. Sakun, Fiz. Tverd. Tela (Leningrad) **14**, 2199 (1972) [Sov. Phys. Solid State **14**, 1906 (1972)].
12. S. I. Golubov and D. V. Konobeev, Fiz. Tverd. Tela (Leningrad) **13**, 3185 (1971) [Sov. Phys. Solid State **13**, 2679 (1971)].
13. T. T. Basiev, M. E. Doroshenko, and V. V. Osiko, Pis'ma Zh. Éksp. Teor. Fiz. **71**, 14 (2000) [JETP Lett. **71**, 8 (2000)].
14. T. T. Basiev, M. E. Doroshenko, and V. V. Osiko, OSA TOPS **34**, 485 (2000).
15. T. T. Basiev, M. E. Doroshenko, V. V. Osiko, *et al.*, in *Advanced Solid State Lasers. Technical Digest* (Optical Society of America, Washington, 2001), p. 93.

Translated by V. Sakun

JETP Letters, Vol. 74, No. 11, 2001, pp. 543–546. Translated from Pis'ma v Zhurnal Éksperimental'noĭ i Teoreticheskoĭ Fiziki, Vol. 74, No. 11, 2001, pp. 616–619.

$^4T_2 \longrightarrow {}^4A_2$ Transition in the Luminescence Spectra of Mn^{4+} Ion in Gadolinium Gallium Garnet at Intense Laser Pumping

S. V. Bulyarskiĭ, A. V. Zhukov*, and V. V. Prikhod'ko

Ul'yanovsk State University, Ul'yanovsk, 432700 Russia

**e-mail: avg@ulsu.ru*

Received October 14, 2001

The Mn^{4+} $^4T_2 \longrightarrow {}^4A_2$ transition was observed in the luminescence spectrum of $Gd_3Ga_5O_{12}$:Mn^{4+} at intense laser pumping. It is shown that the $^4T_2 \longrightarrow {}^4A_2$ transition becomes more intense than $^2E \longrightarrow {}^4A_2$ because of an increase in the role of induced transitions with increasing pump power. This process is most efficient in the region of strongest overlap between the $^2E \longrightarrow {}^4A_2$ and $^4T_2 \longrightarrow {}^4A_2$ bands, where it leads to strengthening of the zero-phonon line of the latter at 694 nm. It is assumed that GGG:Mn^{4+} can be used as an active material in tunable lasers. © *2001 MAIK "Nauka/Interperiodica".*

PACS numbers: 78.55.-m

The transition-metal impurities with the d^3 configuration of the unfilled electronic shell, such as Cr^{3+}, Mn^{4+}, or V^{2+}, have drawn the attention of researchers in connection with the search for new materials for the active media of solid-state lasers. Crystals with garnet structure are promising matrices for the indicated impurities.

The Cr^{3+} ion is the most thoroughly studied d^3 impurity in the garnet structure [1, 2]. The luminescence spectra of chromium ion show two characteristic bands: a narrow R line (Cr^{3+} $^2E \longrightarrow {}^4A_2$ transition) near 695 nm in garnets and a broad band at longer wavelengths ($^4T_2 \longrightarrow {}^4A_2$ transition). Depending on the crystal field strength, either of these transitions may dominate in the spectra [3].

The structures of unfilled electronic shells of the Mn^{4+} and Cr^{3+} ions are similar. Although this implies the similarity of their optical properties, the luminescence and absorption spectra of the manganese ion display a number of distinctive features [4–7]. One of them is caused by a large crystal-field parameter (D_q) of Mn^{4+} in garnet crystals [8]. For instance, $D_q = 1960$ cm^{-1} for Mn^{3+} in gadolinium gallium garnet $Gd_3Ga_5O_{12}$ (GGG), whereas, for the Cr^{3+} ion, $D_q = 1585$ cm^{-1} in this material [4]. According to the Tanabe–Sugano diagram [3], the $^2E \longrightarrow {}^4A_2$ transition in this case dominates the luminescence spectra of Mn^{4+}, while the $^4T_2 \longrightarrow {}^4A_2$ transition (which is typical of the chromium ion in this material [2]) is virtually absent.

It will be shown in this work that, under certain conditions, namely, at temperatures above 300 K and at intense pumping, the relative intensity of the $^4T_2 \longrightarrow {}^4A_2$ transition increases in the luminescence spectra of GGG:Mn^{4+}. This is caused by two major factors: difference in the temperature dependences of the $^4T_2 \longrightarrow {}^4A_2$- and $^2E \longrightarrow {}^4A_2$-transition probabilities and enhancement of induced emission.

Samples and analysis of spectra at different pumping levels and temperatures. Samples for study were plates with ground 0.5-mm-thick plane-parallel [111]-oriented faces ~0.5 × 1 cm in size. All samples were transparent in the visible region and differed only by the pale coloration of some of them because of the uncontrolled inclusion of the so-called F-centers in the lattice [9].

The concentration of the Mn impurity in the samples was lower than 0.1 at.%. This allowed one to ignore the complexation process, which could give rise to new lines in the luminescence spectra [10, 11].

The luminescence spectra were measured on a SDL-2 or DFS-24 spectrometer. The luminescence was excited using a cw YAG:Nd laser with the wavelength $\lambda = 532$ nm and an output of 200 W and a pulse-periodic copper vapor laser with $\lambda = 510.6$ nm, output $P = 1000$ W, pulse repetition rate $f = 8$ kHz, and pulse duration $\tau = 20$ ns. These lasers were chosen because their radiation wavelengths fell within the Mn^{4+} absorption band corresponding to the $^4A_2 \longrightarrow {}^4T_2$ transition [4]. The spectra were measured at several fixed temperatures in the range from 100 to 390 K. For this purpose, the samples were placed into a cryostat in a special holder which provided beam incidence on the side cleavage. Heating was provided by a tungsten heating element, and temperature was controlled by a copper–constantan thermocouple.

The luminescence spectra measured for all manganese-doped GGG samples at a low pump power per surface unit (power density $P_L \sim 10$ W/cm^2) and room tem-

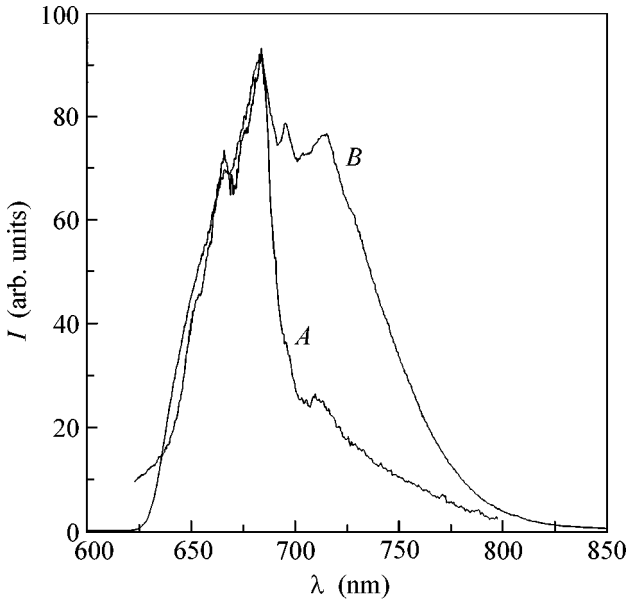

Fig. 1. Luminescence spectrum of GGG:Mn^{4+} at 300 K and power density P_L ~ (*A*) 10 W/cm^2 and (*B*) 10^6 W/cm^2.

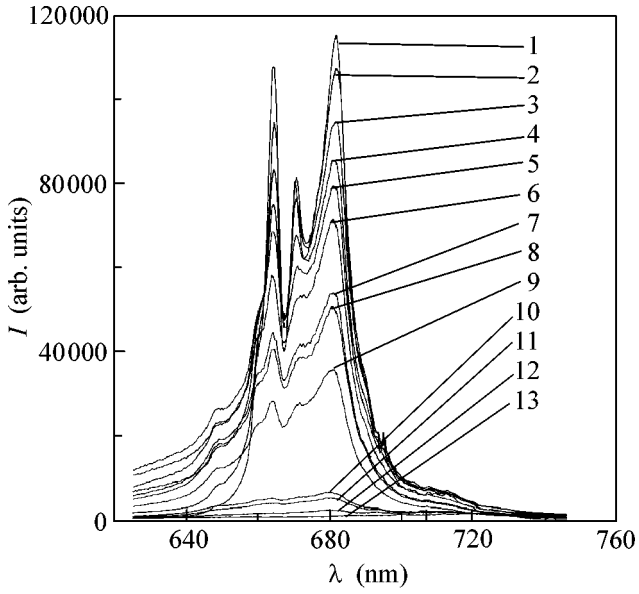

Fig. 2. Luminescence spectrum of GGG:Mn^{4+} at different temperatures: (*1*) 100, (*2*) 125, (*3*) 150, (*4*) 175, (*5*) 200, (*6*) 225, (*7*) 250, (*8*) 260, (*9*) 270, (*10*) 285, (*11*) 300, (*12*) 330, and (*13*) 390 K.

perature showed characteristic bands in the range 650–700 nm (Fig. 1). Following [4, 12], spectrum *A* was interpreted as an emission spectrum of the fourfold ionized manganese ion in GGG. The $^2E \longrightarrow {}^4A_2$ transition is clearly seen in the spectrum. It consists of the *R* line at 663.5 nm [4] and a complex, presumably vibronic, structure at longer wavelengths with a maximum at 682 nm.

At large power densities (P_L > 10 kW/cm^2), a new maximum appears at a wavelength of 714 nm in the spectra. In [4], where the Mn^{4+} $^2E \longrightarrow {}^4A_2$ transition was selectively excited, this peak was not observed. One can see from the comparison of spectra *A* and *B* in Fig. 1 that the new peak (with a maximum at 710–714 nm) is present in the luminescence spectrum under ordinary conditions as well (low pumping level), but in this case it is weak to such an extent that it cannot be distinguished from the vibronic satellite of the *R* line [4–7]. Based on the analogy with the spectrum of the tervalent chromium ion [2, 13, 14], we assumed that these new peaks are due to the $^4T_2 \longrightarrow {}^4A_2$ transition of the Mn^{4+} ion in gadolinium gallium garnet. Spectrum *B* of GGG:Mn^{4+} in Fig. 1 was obtained at the power density P_L ~ 10^6 W/cm^2. The $^4T_2 \longrightarrow {}^4A_2$-transition spectrum represents a broad wavy structure with weak equidistant peaks. A maximum at 694 nm, which is also invisible at a low pumping level, was tentatively assigned to the zero-phonon line of the $^4T_2 \longrightarrow {}^4A_2$ transition.

The shape analysis carried out for the GGG:Mn^{4+} spectra measured at different temperatures confirmed that the line with a maximum at 714 nm could be assigned to the $^4T_2 \longrightarrow {}^4A_2$ transition. The lines became broader with rise in temperature, and the integrated intensity of the entire band decreased drastically starting at 250–270 K (Fig. 2). Such a behavior of the spectrum cannot be explained solely by, for example, broadening and splitting of the $^2E \longrightarrow {}^4A_2$ band in the presence of crystal inhomogeneities [15, 16].

A sharp drop in the integrated intensity at temperatures above ~250–270 K is evidence of the thermoactivated character of radiationless transitions [17]. The temperature dependences of integrated intensities of the $^2E \longrightarrow {}^4A_2$ and $^4T_2 \longrightarrow {}^4A_2$ transitions are shown in Fig. 3. The temperature dependence of the ^2E-level lifetime [5] is shown in the same figure for the comparison. Close to room temperature, the intensities of both transitions sharply, though not synchronously, decreased. The observed temperature behavior of the luminescence in this temperature interval could be explained by a redistribution of the intensities of the $^2E \longrightarrow {}^4A_2$ and $^4T_2 \longrightarrow {}^4A_2$ transitions as a result of the sample heating due to an increase in pump power. However, temperature measurements at a high power density (P_L ~ 10^6 W/cm^2) showed that this effect could not be the only cause of the observed intensity redistribution. The obtained dependences of integrated intensities differed from those shown in Fig. 3 only by a shift along the temperature axis by 21 and 19 K for the $^2E \longrightarrow {}^4A_2$ and $^4T_2 \longrightarrow {}^4A_2$ transitions, respectively. Moreover, a sharp peak at 694 nm, which was assigned to the zero-phonon line of the $^4T_2 \longrightarrow {}^4A_2$ transition, became more intense.

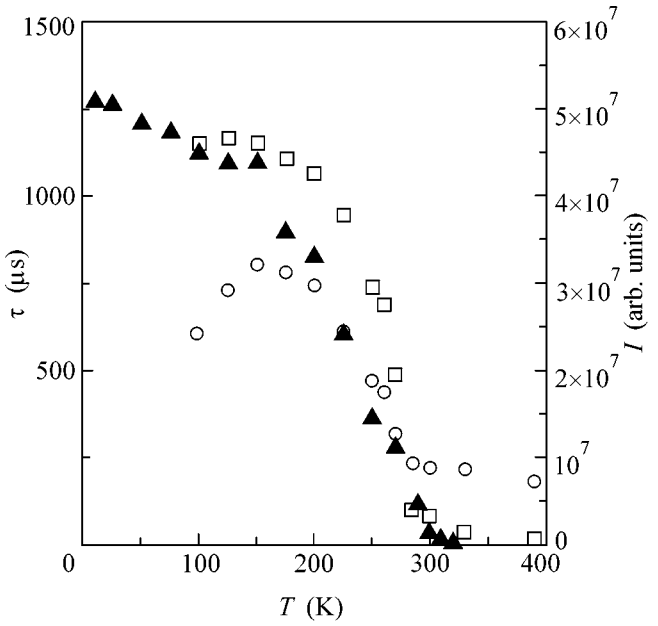

Fig. 3. Temperature dependences for the integrated intensities of optical transitions (squares) $^2E \longrightarrow {}^4A_2$ and (circles) $^4T_2 \longrightarrow {}^4A_2$, and (triangles; data from [4]) the same for the 2*E*-level lifetime.

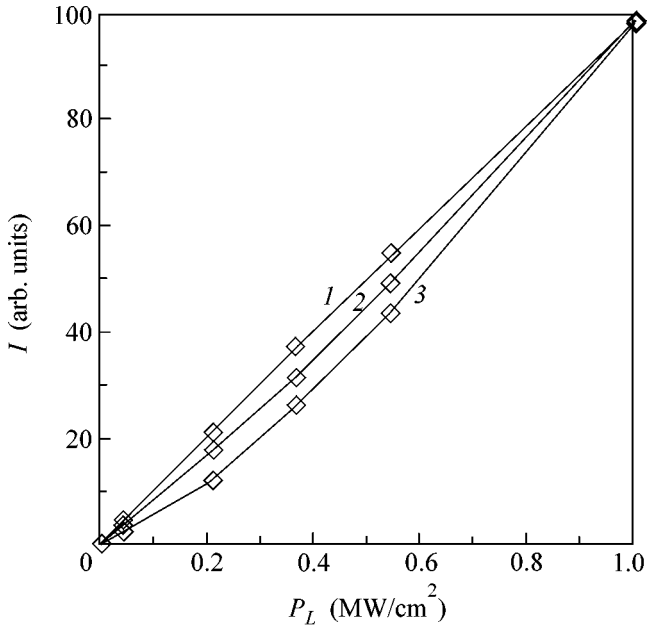

Fig. 4. Normalized experimental dependences for the integrated intensities of the (*1*) $^2E \longrightarrow {}^4A_2$ and (*2*) $^4T_2 \longrightarrow {}^4A_2$ transitions, and (*3*) $^4T_2 \longrightarrow {}^4A_2$ the same for the peak intensity of the zero-phonon line.

The integrated intensities of the $^2E \longrightarrow {}^4A_2$ and $^4T_2 \longrightarrow {}^4A_2$ transitions and the peak intensity of the $^4T_2 \longrightarrow {}^4A_2$ zero-phonon line are shown in Fig. 4 as functions of power density. The peak intensity of the zero-phonon line was obtained after the approximation and subtraction of the background level. The behavior of the curves points to the saturation of the $^4T_2 \longrightarrow {}^2E \longrightarrow {}^4A_2$ channel and the intensification of the transition from the $^4T_2$ level directly to the ground $^4A_2$ level. Indeed, according to [4], the 2*E* level is long-lived (τ = 1.2 ms at T = 77 K).

An increase in peak intensity of the zero-phonon line and a nonlinear power dependence of the integrated intensity of the $^4T_2 \longrightarrow {}^4A_2$ transition allow the assumption to be made that these effects are manifestations of the induced transitions. The $^4T_2 \longrightarrow {}^4A_2$ emission is caused not only by the transitions from the same level but also by the more intense $^2E \longrightarrow {}^4A_2$ transitions. This becomes possible because of the strong overlap of these bands. The overlap in the region of the $^4T_2 \longrightarrow {}^4A_2$ zero-phonon line is stronger than in the longer wavelength region, leading to the enhancement of the induced radiation effect precisely for the zero-phonon line.

In summary, the observation of the $^4T_2 \longrightarrow {}^4A_2$ transition in the luminescence spectra of GGG:Mn^{4+} has been reported in this work. This transition is particularly pronounced in the presence of intense laser pumping. The transition was identified by comparing the luminescence spectrum of GGG:Mn^{4+} with the spectra of the Cr^{3+} ion, for which the corresponding transition is observed in GGG and other garnets in the wavelength region redshifted from the *R* line.

It has been shown in this work that an increase in the $^4T_2 \longrightarrow {}^4A_2$-transition intensity in the luminescence spectra of GGG:Mn^{4+} becomes possible due to the increase in the role of induced transitions at high laser intensity. This process is more intense in the region of strongest overlap between the $^2E \longrightarrow {}^4A_2$ and $^4T_2 \longrightarrow {}^4A_2$ transitions, which results in strengthening of the zero-phonon line of the latter.

The observed considerable homogeneous broadening of the *R* line makes GGG:Mn^{4+} promising as an active element of tunable lasers.

REFERENCES

1. M. Yamaga, B. Henderson, *et al.*, Phys. Rev. B **46**, 3273 (1992).
2. U. Hoemmerich and K. L. Bray, Phys. Rev. B **51**, 12133 (1995).
3. J. F. Donegan, T. J. Glynn, and C. F. Imbusch, J. Lumin. **36**, 93 (1986).
4. A. Brenier, A. Suchocki, C. Pedrini, *et al.*, Phys. Rev. B **46**, 3219 (1992).
5. A. Suchocki, M. Potemski, A. Brenier, *et al.*, J. Appl. Spectrosc. **62**, 181 (1995).
6. B. R. Jovanic, J. Lumin. **75**, 171 (1997).

7. L. A. Riseberg and M. J. Weber, Solid State Commun. **9**, 791 (1971).
8. I. B. Bersuker, *Spectroscopy of Crystals* (Nauka, Leningrad, 1973), p. 22.
9. G. J. Pogatsnik, L. S. Cain, Y. Chen, *et al.*, Phys. Rev. B **43**, 1787 (1991).
10. M. Kh. Ashurov, Yu. K. Voron'ko, V. V. Osiko, *et al.*, *Spectroscopy of Crystals* (Nauka, Leningrad, 1978), p. 55.
11. E. G. Valyashko, S. V. Grum-Grzhimaĭlo, I. M. Kutovoĭ, *et al.*, *Spectroscopy of Crystals* (Nauka, Moscow, 1966), p. 55.
12. O. N. Boksha and S. V. Grum-Grzhimaĭlo, *Spectroscopy of Crystals* (Nauka, Moscow, 1970).
13. A. Monteil, M. Ferrari, and F. Rossi, Phys. Rev. B **43**, 3646 (1991).
14. B. Struve and G. Huber, Appl. Phys. B **B36**, 195 (1985).
15. A. A. Kaplyanskiĭ, S. P. Feofilov, and R. I. Zakharchenya, Opt. Spektrosk. **79**, 709 (1995).
16. S. V. Bulyarskii, A. E. Kozhevin, S. N. Mikov, *et al.*, Phys. Status Solidi A **180**, 408 (2000).
17. S. V. Bulyarskiĭ and N. S. Grushko, *Generation-Recombination Processes in Active Elements* (Mosk. Gos. Univ., Moscow, 1995).

Translated by V. Sakun

JETP Letters, Vol. 74, No. 11, 2001, pp. 547–551. Translated from Pis'ma v Zhurnal Éksperimental'noĭ i Teoreticheskoĭ Fiziki, Vol. 74, No. 11, 2001, pp. 620–624.

Turbulent Boundary Layer at the Border of Geomagnetic Trap

S. P. Savin[1, *], L. M. Zelenyi[1], S. A. Romanov[1], S. I. Klimov[1], A. A. Skalsky[1], A. A. Galeev[1], V. N. Smirnov[1], M. N. Nozdrachev[1], Yu. I. Yermolaev[1], L. A. Avanov[1], E. Amata[2], J. Blecki[3], J. Buechner[4], B. Nikutowski[4], É. M. Dubinin[4], Z. Nemecek[5], J. Safrankova[5], A. Pedersen[6], J. L. Rauch[7], J. Rustenbach[8], J. A. Sauvaud[9], P. Song[10], and K. Stasiewicz[11]

[1] *Space Research Institute, Russian Academy of Sciences, Moscow, 117997 Russia*
**e-mail: ssavin@iki.rssi.ru*
[2] *Istituto Fisica Spazio Interplanetario, 00133 Roma, Italy*
[3] *Centrum Badan Kosmicznych, 00716 Warsaw, Poland*
[4] *Institute Aeronomie, 37191 Katlenburg-Lindau, Germany*
[5] *Charles University, 18000 Prague, Czech Republic*
[6] *University of Oslo, 01235 Norway*
[7] *Lab Physics, Chemistry Environment, 30037 Orleans, France*
[8] *Institut Physics, 11240 Berlin, Germany*
[9] *Centre d'Etude Spatiale Rayonnements, 31028 Toulouse, France*
[10] *University of Massachusetts, 01854 Lowell, USA*
[11] *Institute of Space Physics, 75121 Uppsala, Sweden*
Received October 23, 2001; in final form, November 16, 2001

A new phenomenon was discovered on the basis of analysis of the Interball project data. A hot plasma flow is thermalized through the formation of "long-operating" vortex streets and local discontinuities and solitons in a distributed region over polar cusps. Plasma percolation through the structured boundary and secondary reconnection of fluctuating magnetic fields in a high-latitude turbulent boundary layer account for the main part of solar wind plasma inflow into the magnetospheric trap. Unlike local shocks, the ion thermalization is accompanied by the generation of coherent Alfvén waves on the scales ranging from ion gyroradius to the radius of curvature of the averaged magnetic field, as well as by the generation of diamagnetic bubbles with a demagnetized heated plasma inside. This "boiling" plasma has a frequency region where the spectrum is different from the Kolmogorov law (with slopes 1.2 and 2.4 instead of 5/3 or 3/2). The fluctuation self-organization in the boundary layer (synchronization of three-wave decays) was observed on certain frequency scales.

PACS numbers: 94.30.Fk; 52.35.Ra; 94.30.Tz

This work is devoted to the experimental study of singular regions at the high-latitude boundary of a geomagnetic trap, where the incoming solar plasma flow forms a zone of strong turbulence—a turbulent boundary layer (TBL). In the TBL, magnetic field fluctuations are on the order of field magnitude, while their total energy density (W_b) in the range from 0.1 to 1 Hz amounts to 10–30% of the density of ion thermal energy E_{th} [1]. The possible formation of TBL was predicted by Haerendel in [2]. More recently, a number of groups continued studying the region of the outer polar cusp in a high-latitude region of the magnetic-field minimum at the boundary between the nightside and dayside magnetic field lines. However, much of the effort was focused on the reconnection of field lines at low latitudes. In [3], it was shown that the TBL is virtually constantly present and that its fluctuations have an essentially nonlinear character. It is the purpose of this work to discuss the properties and nature of fluctuations in the TBL on the basis of the Interball-1 satellite data,

Turbulent boundary layer at April 2, 1996. A typical exit of the Interball-1 satellite from the polar cusp and its entry into the magnetosheath (MSH) between the collisionless shock in the solar wind and the magnetopause (MP) which occurred April 2, 1996, is shown in Fig. 1 (see also Fig. 4). The MP manifests itself by a transition of the magnetic field component B_x from large negative values to small (on average) values and by the predominance of E_{th} over the magnetic pressure $B^2/8\pi$ in the TBL and MSH. The region of transition to the plasma flow (PF), where $E_{th} \sim E_{kin}$ (ion kinetic energy density), is separated from the MP by the zone of enhanced turbulence (i.e., TBL), which is shown by black shadowing under the trace of the total energy

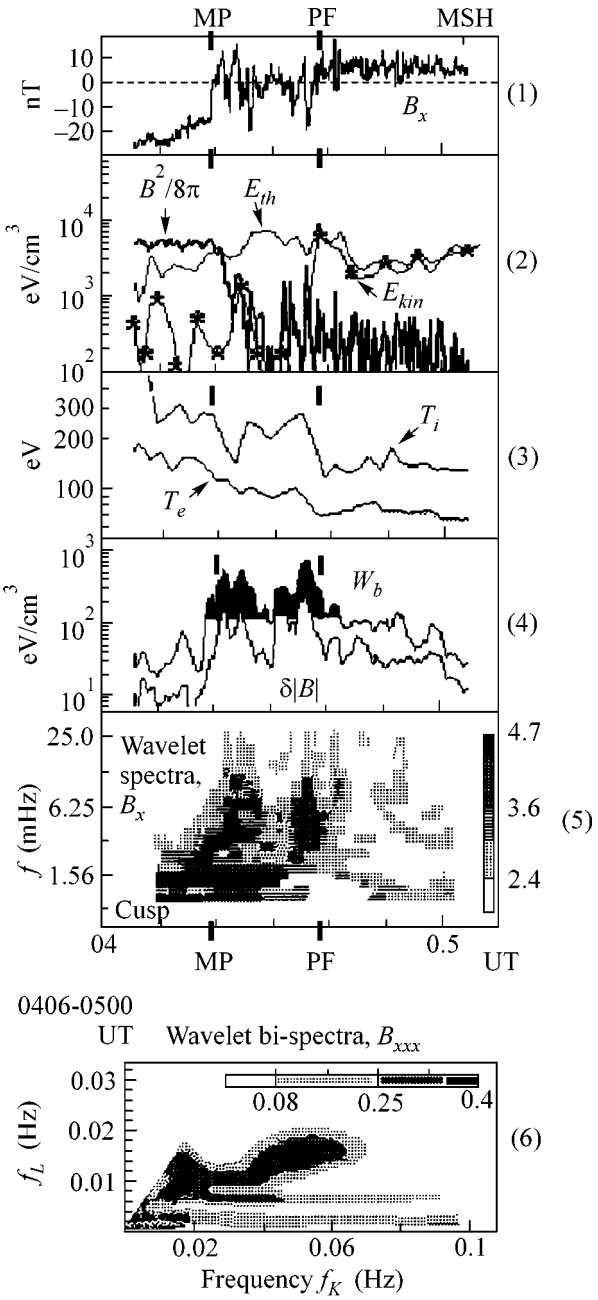

Fig. 1. The Interball-1 exit from the cusp and its entry into the MSH at April 2, 1996 (for details, see text). From top to bottom: (1) B_x is the magnetic field component, (2) ion and magnetic field energy densities, (3) ion and electron temperatures, (4) magnetic fluctuation power, (5) wavelet spectrum of B_x, and (6) wavelet bi-spectrum of B_x.

density W_b of magnetic field fluctuations. The W_b quantity includes the variations of field magnitude and its angular oscillations. A comparison of W_b with the fluctuation energy $\delta|\mathbf{B}|$ of the absolute value of magnetic field in the same energy range and with E_{th} indicates that, in this zone, W_b attains $3.5\delta|\mathbf{B}|$ and $0.1E_{th}$ (i.e., incompressible oscillations dominate). In this zone, the ion temperature T_i increases by a factor of 2.2 and the electron temperature T_e increases by a factor of 1.3, while the magnetic energy density $B^2/8\pi$ drops to low values corresponding to "diamagnetic bubbles" (DB; see [1, 3]). One can see in the lower left corner of the lower panel in Fig. 2 that $|\mathbf{B}| \sim 1$ nT inside DB; i.e., the magnetic field is expelled by hot plasma. The structure of the PF boundary differs substantially from the shock by the presence of a magnetic barrier with $B^2/8\pi \sim E_{th} \sim E_{kin}$ at its maximum in the MSH. This magnetic barrier is a soliton with scale ~130 km (on the order of the ion gyroradius in the MSH) along the direction of minimal magnetic variations (normal to the front) and trapped gyrotropic ions with energy <300 eV (this region is separated by vertical lines in the upper panel of Fig. 2). As for the ions with the gyroradius exceeding barrier size (>170 km), they freely overcome it. The scale was estimated from the delay between the satellite and the subsatellite; the estimate gave a value of ~12 km/s for the plasma velocity along the normal in the satellite coordinate system. Figure 3a shows the ion velocity hodograph (V_x, V_y) in the Sun–Earth ecliptic coordinate system for the transition from TBL to MSH. The velocity vector has a constant direction in the MSH, and the transition is characterized by a decrease in velocity from (–175; 75) to (–60; 0) km/s and the appearance of "loops," which are most naturally explained by the presence of a vortex street in the TBL (cf. [2, 1]). The maximal vortex scale, as estimated from the delay between the satellite and subsatellite transverse to the PF boundary, equals several thousand kilometers, while the estimation from the mean loop velocity (i.e., along the PF) gives ~10 000 km. For the smallest velocity vortices, the scale is ~1000 km. In Fig. 3b, the magnetic field vector at the PF barrier also displays vortex-like transition on a mean scale of 1000 km, together with the presence of small vortices with a size of ~100 km. High-resolution data suggest that the turbulent cascade in the TBL extends to several kilometers (to the electron inertial length). This indicates that field-line freezing in the TBL is broken. However, a considerably weaker electron heating is an indicator of the most intense energy dissipation in the ion gyroradius region (Figs. 2 and 3a). The wavelet spectrogram (see [3]) in Fig. 1 (panel 5) demonstrates a cascade-like development of the perturbations in the TBL; mutually related spectral maxima appear at several frequencies, and the transitions are observed both from low to high frequencies (direct cascade) and in the opposite direction (reverse cascade). Attention should also be given to the maximum at ~1.5 mHz, which is seen both in the TBL and in the MSH and cusp; judging from its intensity, it appears in the TBL near the MP. The cascade-like perturbations correspond to a slope of 1.18 for the B_x power spectrum at frequencies 1–45 mHz and to 2.4 at 0.05–0.4 Hz. Both are different from the slopes of the Kolmogorov spectra of hydrodynamic or Alfvén turbulence (5/3 or 3/2; see [4]). A slope of 1.18 is typical of

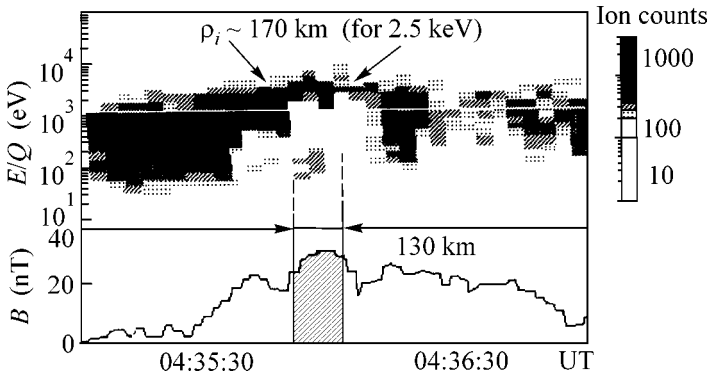

Fig. 2. Structure of the PF boundary; (top) energy distribution per a charge of ions flying from the Sun and (bottom) |**B**|.

a current layer in the critical self-organization state [5]. The detection of fluctuations with different properties indicates the presence of a two-phase (in the statistical meaning) plasma in the TBL; the DB inclusions are analogous to the formation of air bubbles in a boiling fluid.

Influence of turbulence properties on the transport processes. The process of plasma flow (double thick arrows) past the region of geomagnetic field-line divergence (thin lines with arrows) in the vicinity of the polar cusp is schematically illustrated in Fig. 4. The magnetopause MP is concave in this region (thick black line); the solar wind field lines (marked squares) are deformed and run along the MP; at April 2, 1996, the Interball-1 orbit passed over approximately along the diagonal from the bottom right to the top left; the boundary of regular flow is shown by thick dashes. In more than 80% of the cases (of ~400 crossings from 1995 to 2000), the magnetic field and the plasma flows inside the PF were irregular and display the features of vortex cascades [1, 3]. The TBL is adjacent to the MP (shown by vertical hatching). As in Fig. 1, the PF at the center of the region of interest is usually separated from the TBL by the region with reduced W_b and irregular plasma velocity. The average field direction in the TBL is controlled by the interplanetary magnetic field (IMF). Inside the MP, the field is controlled by the Earth dipole, whereas plasma enters the MP (into the cusp; shown by horizontal hatching in Fig. 4) with a slight decrease in E_{th} and an increase in T_i; i.e., the boundary is, in actuality, transparent with clearly seen current layers (cf. B_x in Fig. 1). This picture depends weakly on the IMF, which is important for the penetration of plasma inside the "foreign" magnetic field. The reconnection of the antiparallel field lines at the smooth laminar MP was assumed to be the major mechanism of plasma penetration inside the MP. However, the weak dependence of the cusp and TBL on the IMF direction and the observation of strong perturbations up to the electron inertial length indicate that there may also be different mechanisms. The author of [2] has assumed that the flow into the MSH is broken by an obstacle in the form of a step at the MP to form the TBL, where the ion kinetic energy transforms into heat. Indeed, on the large scales shown in Fig. 1 (for example, at 0430 and

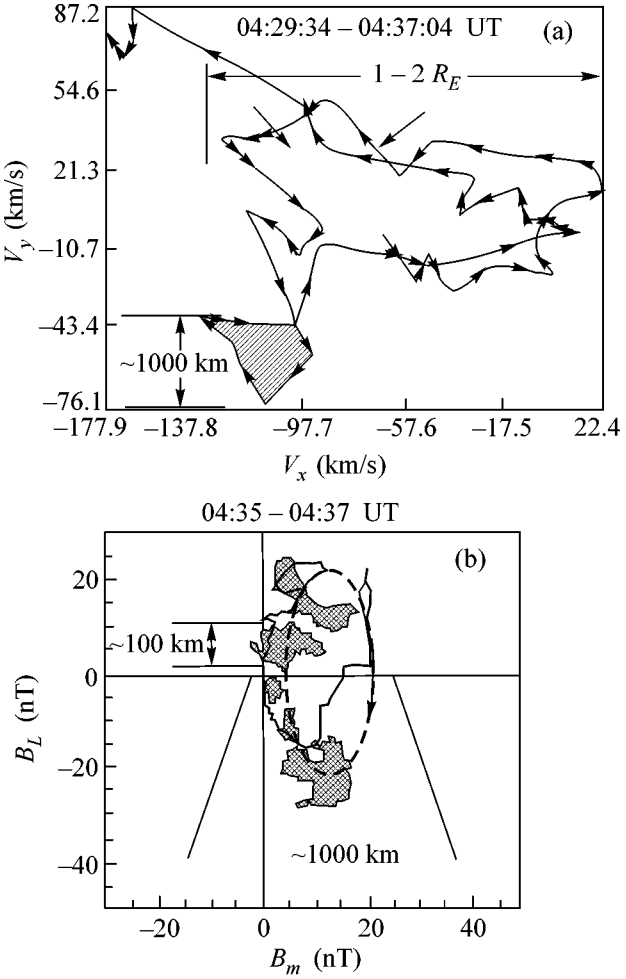

Fig. 3. (a) Ion velocity for the TBL and (b) magnetic-field hodograph for the PF.

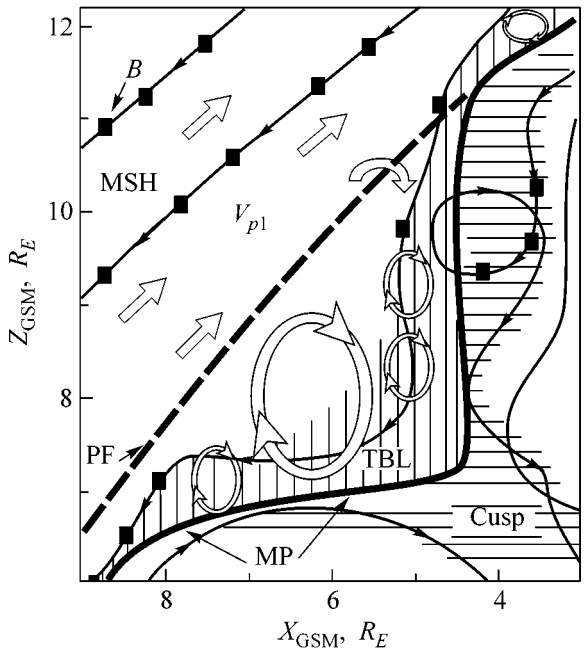

Fig. 4. Scheme of plasma flow along the high-latitude MP over the cusp (for details, see text).

0500 UT), $E_{th} + E_{kin} \sim$ const, with $E_{th} \gg E_{kin}$ inside the PF. Near the PF the flow is locally accelerated to the energies E_{kin} higher than in the MSH. This can really be explained by the acceleration due to the reconnected magnetic-field tension. The reconnection is possible both near the geomagnetic equator and in the cusp locality (an example of reconnection is illustrated in Fig. 4 by the field-line loop with squares). The small-scale fluctuating fields are reconnected efficiently in the TBL as well, as is evident from the breakdown of field-line freezing-in (by virtue of fluctuations on the electron inertial length scale). This allows plasma to penetrate inside the MP and provides efficient magnetic-flux transfer from the dayside of the magnetosphere to its nightside. Nevertheless, we assume that, in the essentially nonlinear situation occurring in the TBL, plasma percolation through the structured boundary makes the main contribution to the local mass transfer inside the MP. Taking the appropriate estimate of diffusion coefficient from [6], one obtains $D_p \sim 0.66\ (\delta B/B_0)\rho_i\Omega_i \sim (5–10) \times 10^9$ m^2/s for the typical MP parameters, where $\delta B/B_0$ is the ratio of the perturbed magnetic field to its average value, and ρ_i and Ω_i are the ion gyroradius and gyrofrequency, respectively. The resulting value; of (1–2) $\times 10^{27}$ particles/s obtained for the flow through the northern and southern TBL is sufficient for filling the magnetosphere with solar plasma.

Let us now turn to the nature of oscillations in TBL. Phase velocity is one of the properties that allows the low-frequency perturbations to be identified with the kinetic Alfvén waves (KAWs). We used the Interball-1 and Polar satellite data on the electric (E) and magnetic (B) fields in the TBL at August 26, 1995, May 5, 1996, June 19, 1998, and June 23, 1998 to verify that (a) like on April 2, 1996, the magnetic spectrum has two characteristic slopes and (b) the low-frequency phase velocity $V_{ph} = E/B$ is close to the Alfvén velocity V_A and shows, on the average, a tendency toward the frequency dependence characteristic of the satellite flight through the KAW spatial structures, up to a frequency of several hertz (which is several times lower than the hybrid frequency). This dependence is expressed by the formula [3]

$$(E/B)^2 \sim V_A^2(1 + (\rho_i\omega/V)^2) \qquad (1)$$

where ω is the frequency, V is the velocity of KAW structures relative to the satellite, and $(\rho_i\omega/V)^2$ is the kinetic addition allowing for the finiteness of the ion gyroradius (KAW takes its name precisely from this fact). In most cases, the asymptotic behavior of (E/B) had the form $\sim\omega$, i.e., corresponded to Eq. (1). This, however, cannot be distinguished from the detection of waves with a constant wave vector **k**, because the Fourier transform of plane waves obeys the Maxwell equation $kE \sim \omega B$. Therefore, Eq. (1) does not allow the identification of KAW in the asymptotic region. The TBL is also characterized by the three-wave decay processes satisfying the condition $f = f_L + f_K$ (for more detail, see [3]). In the frequency range of interest, the products of the appropriate three amplitudes show maxima up to 40% at frequencies $f_L \sim 1.5$, 5, and 15 mHz (vertical axis in the lower panel for the wavelet bi-spectrum in Fig. 1) and over a continuous range of 1.5–80 mHz for f_K. This signifies that the phase–frequency relations are fulfilled for the three-wave process (if the higher-order nonlinear processes are ignored) and the structures with the indicated frequencies f_L decay in a broad range of frequencies f_K and f. That is, the processes at these frequencies (on the vertical axis) synchronize cascades in a broad frequency range (along the horizontal axis). A well-defined maximum at (f_L, f_K) $\sim$ (15, 50) mHz indicates that the reverse cascade can be pumped at high KAW frequencies. We thus assume that the inhomogeneities in the incoming flow interact with the current layer of MP to generate KAWs, a part of which are reflected back, focused by the concave MP, and interact with the incoming flow. As a result, a number of cascades synchronized at the above-mentioned frequencies f_L arise self-consistently. If the estimate of the upper limit of the characteristic scale at 1.5 mHz is carried out using V_A, then $L \sim V_A/f_L \sim (3–7)R_E$ (Earth radii) is comparable with the TBL length, and L is also on the order of the radius of curvature of the unperturbed MP or the MSH thickness at the dayside. On the other hand, the presence of a maximum at 1.5 mHz both in the MSH and in the cusp inside the MP (Fig. 1) also suggests that the observed process is global. To understand the nature of this resonance in more detail, it is necessary to carry out additional measurements at several points and at distances of both several thousand

kilometers and several Earth radii. We used the magnetosonic Mach number M_m in MSH, the Alfvén number, for either the ion velocity projection normal to the PF ($M_{An} \sim M_m \sim 1.2$) or the total velocity ($M_A \sim 3.5$) to compare the ion heating in the TBL with the Rankine–Hugoniot relations at the shock and arrived, respectively, at the following results: $T_i/T_{MSH} \sim 1 + (\gamma - 1)M^2 \sim 1.6$ or ~5 for the adiabatic exponent $\gamma \sim 5/3$ (remembering that $E_{th} \gg E_{kin}$ in the TBL). The observed ion heating in the TBL (~2.2) is greater than at the oblique shock and considerably less than its maximum possible value. Therefore, the observed process of energy transformation differs substantially from the one in the collisionless shock; the entire perturbed region (Fig. 4) should be considered as a whole with long-operating KAW cascades and vortex streets, as well as with local discontinuities and solitons (MP and PF).

To conclude, we would like to note that the investigation into the role and properties of turbulence at the critical point of a geomagnetic trap (turbulent boundary layer) allows the revelation of the key role of turbulent microprocesses accompanying the interaction of plasma flows with magnetic obstacles, be it the fields of planers, starts, black holes, or laboratory traps, and demonstrates real mechanisms of energy transformation in collisionless plasmas.

This work was supported by the International Space Science Institution, the INTAS/ESA (grant no. 99-1006), the INTAS (grant no. 2000-465), the CLG (grant no. 975277), the Humbolt Foundation, and the State Contract [project no. 10-10(00)-P-D 01].

REFERENCES

1. S. P. Savin, N. L. Borodkova, E. Yu. Budnik, *et al.*, Geophys. Monogr., Am. Geophys. Union **104**, 25 (1998).
2. G. Haerendel, J. Atmos. Terr. Phys. **40**, 343 (1978).
3. S. Savin, L. Zelenyi, J. L. Rauch, *et al.*, Ann. Geophys. **19** (2001) (in press).
4. P. S. Iroshnikov, Astron. Zh. **40**, 742 (1963) [Sov. Astron. **7**, 566 (1963)].
5. L. M. Zelenyi and A. V. Milovanov, *Multiscale Magnetic Structure of the Distant Tail: Self-consistent Fractal Approach* (AGU, Washington, 1998), Geophys. Monograph **105**, p. 321.
6. A. A. Galeev, L. M. Zelenyĭ, and M. M. Kuznetsova, Pis'ma Zh. Éksp. Teor. Fiz. **41**, 316 (1985) [JETP Lett. **41**, 387 (1985)].

Translated by V. Sakun

JETP Letters, Vol. 74, No. 11, 2001, pp. 552–555. From Pis'ma v Zhurnal Éksperimental'noĭ i Teoreticheskoĭ Fiziki, Vol. 74, No. 11, 2001, pp. 625–629.

Microscopic Mechanism of Stability in Yttria-Doped Zirconia[1]

S. A. Ostanin and E. I. Salamatov*

Department of Physics, University of Warwick, Coventry CV4 7AL, United Kingdom

** Physicotechnical Institute, Ural Division, Russian Academy of Sciences, ul. Kirova 132, lzhevsk, 426001 Russia*

Received October 23, 2001

The relaxed configurations of yttria-stabilised zirconia (YSZ) between 3 and 10 mol % of Y_2O_3 were modeled using the pseudopotential technique. In the displacive limit of a double-well potential model, the vibrational mode corresponding to the soft phonon in pure *c*-ZrO_2 was calculated for each Y_2O_3 composition. These anharmonic vibrations, associated with the stabilization of YSZ, were investigated within the self-consistent phonon approximation making obtainable the fine structure in spectral density. In studying the phonon dynamics, we use the displacement probability density, which can quantify very accurately the transition temperature necessary for stabilizing the YSZ cubic phase. © *2001 MAIK "Nauka/Interperiodica"*.

PACS numbers: 63.20.-e; 64.70.Kb

Yttria stabilized zirconia (YSZ), formed by the addition of Y_2O_3 to ZrO_2, is a property controlling material with numerous commercial applications [1]. Pure ZrO_2 exhibits three polymorphous modifications: the monoclinic (*m*) phase, the tetragonal (*t*) phase between 1170°C and 2370°C, and the high-temperature cubic (*c*) phase, which exists up to the melting point. Y_2O_3 has a large solid solubility range in ZrO_2 and can be used to stabilize the *t* phase of $(Y_2O_3)_x(ZrO_2)_{1-x}$ over the composition range $0.02 < x < 0.09$ and the *c* phase with $0.04 < x < 0.4$. In pure *c*- and *t*-ZrO_2, the Zr^{4+} ions are located in perfect and distorted 8-fold coordination environments, respectively, while, in *m*-ZrO_2, Zr^{4+} is found in 7-fold coordination. In YSZ, the trivalent dopant cations Y^{3+} substitute for some of the Zr^{4+} ions and, in order to maintain charge neutrality, one O vacancy (□) must be created for each pair of dopant cations. The presence of □*s* reduces the average cation coordination number to a value between 7 and 8, depending on the dopant concentration. YSZ contains relaxed defects such as □*s* and *Y* substituted atoms, which make the local atomic enviroments of the stabilized crystals rather different from the corresponding stoichiometric phases.

Figure 1 shows the arrangement of atoms around the vacant O site before structural relaxation. The large cube in Fig. 1 is the conventional fluorite unit cell with a side of length *a*. It is divided into eight octants, and it is clear that the four 7-fold coordinated cations NN to the □ occupy the centers of alternate octants to create a tetrathedral arrangement around the vacancy. The *t* distortion of the metal sublattice (~1.03) has little effect on the relaxation process [2] and, therefore, it can he neglected. The anion sites nearest neighbouring (NN) to the □ are located at the face centers of the fluorite cube, while the next nearest neighbouring (NNN) anions are positioned at the middle of each edge of the cube, and the third nearest (NNNN) anions are at the corners. Figure 1 shows the initial *t* distortion of the O sublattice with alternate columns of O displaced up and down by 0.06*a* along the unique direction defined as [001].

To date, no full quantitative description of the stabilization mechanism of YSZ has been reported. The X-ray absorption findings [3] confirm that dopant cations do not take an active part in stabilization. Using the *ab initio* technique to relax the *c* cell, Stapper *et al.* [4] have reported that the cation sites NNN to vacancy,

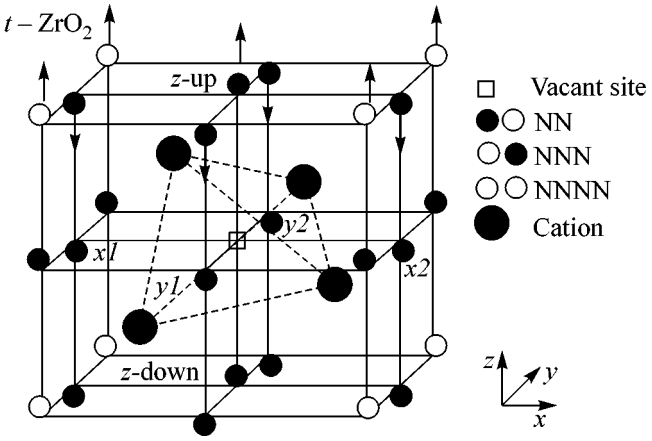

Fig. 1. Unrelaxed arrangements of atoms in pure *t*-ZrO_2 near the vacant fluorite O site shown as a small empty box at the center. The big circles, which form a tetrahedron, denote the ideal cation NN sites, while the smaller circles denote the O NN (black), NNN (grey), and NNNN (light). The O atoms NN to the □ are labelled.

[1] This work was submitted by the authors in English.

rather than NN sites, are favored for Y. Placing Y in the NNN positions allows the coordination of Zr atoms in the sites NN to the □ to be similar to the arrangement in the *m* phase, while Y remains 8-fold coordinated. If the vacancies associate with host Zr ions, it may support a coordination-driven ordering model of stabilization in YSZ, which argues that increasing covalency lowers the coordination of Zr.

In recent neutron diffraction experiments it has been reported that, at low concentrations of Y_2O_3, there are regions ~15–20 Å in size which contain isolated O □ and □*s* arranged in pairs on the NN anion sites in the [111] fluorite direction, with the cation site located between them occupied by Zr [5]. Modeling the long-range ordered $Zr_3Y_4O_{12}$ structure, Bogicevic *et al.* [6] have also reported that the □ pair along ⟨111⟩ and the 6-fold coordinated Zr appear in the most energetically favorable relaxed compositions. Electrostatic considerations suggest that □*s* should repel. From this point of view, the di-□ configuration along ⟨111⟩ would be favorable against those along ⟨100⟩ or ⟨110⟩. Because of the small size of Zr^{4+}, the electrostatic arguments place ZrO_2 on the border between the 8-fold coordinated fluorite and 6-fold coordinated structures [7]. The presence of the larger Y atoms, which possess the longer Y–O bond, compared to the Zr–O bond, appears to shift this balance in favor of 7-fold and 6-fold coordination for Zr, resulting in the local *m*- and brookite-type [8] bonds, respectively.

As for doped ZrO_2, no microscopic mechanism for the phase transitions has been proposed up to now. In pure ZrO_2, a zone-boundary soft phonon, X_2^--, which breaks the *c* symmetry of the O sublattice, displacing the O atoms toward their positions in the *t* phase, might be responsible for the $c \longrightarrow t$ transformation. The previous calculations of the X_2^--phonon frequency within the harmonic approximation [2, 9] yield an imaginary frequency of 5.2–5.5 THz. This simply indicates that the *c*-ZrO_2 is unstable at low temperatures. At high temperatures, the effects of anharmonicity might stabilize the *c* phase. Unfortunately, in YSZ, the experimental data [10] are not fully clarified for this soft mode because of the static disorders in the O sublattice. Thus, our theoretical investigation of the YSZ vibration mode, which corresponds to the X_2^- phonon, would be useful in understanding the role of the atomic vibrations in this material. We believe that the allowance for anharmonicity can give a quantitative criterion for the microscopic mechanism of stability. In this approach, the "frozen-phonon" method [11] and self-consistent phonon approximation [12] are used to calculate the phonon frequency and its temperature dependence, respectively.

The plane-wave, pseudopotential-based free-energy molecular dynamics technique [13] is used to relax the positions of atoms in the (96-*y*)-atom YSZ supercells ($y = 1, 2, 3$), allowing one to calculate the X_2^- phonon in VSZ between the 3 and 10 mol % Y_2O_3 composition. The 95-atom cell corresponds to 3.2 mol % Y_2O_3-ZrO_2. Starting with the *c* configuration of O and the experimental value of the unit cell volume, we make the static optimization allowing the coordinates of all atoms to be relaxed. Experimentally, 3 mol % Y_2O_3-ZrO_2 can exist indefinitely in the *t* form. The effect of starting relaxation with the O atoms in the *t* geometry was investigated as well, showing that the total energies are reduced by ~ 1 eV/cell relative to the relaxed *c* configurations. The □ strongly prefers Y in NN sites before relaxation, but, after relaxation, a configuration with two Y NNN shows the lowest energy. The energy differences between the different Zr/Y NNN configurations are only ~ 1 meV/cation, so that all are likely to coexist in this material at room temperature.

The 94- and 93-atom cells model 6.7 and 10.4 mol % Y_2O_3-ZrO_2. Placing Y not closer than NNN site to each □, an optimum configuration was obtained. In the lowest energy configuration of the divacancy cell, the □*s* are along the fluorite [111] direction and separated by the 6-fold coordinated Zr. This brookite-type Zr–O motif sometimes can appear in the low-energy configurations of the high Y_2O_3 compositions. Figure 2, panel (a), shows the difference in energy between the most stable *c* and *t* configurations. The energy is given in Kelvins per cation to show the temperature required. In the mono- and di-□ cells, the *t* configurations are more stable while, for 3-□*s*, the *c* configuration is marginally more stable. Experimentally, the same change in stability is observed.

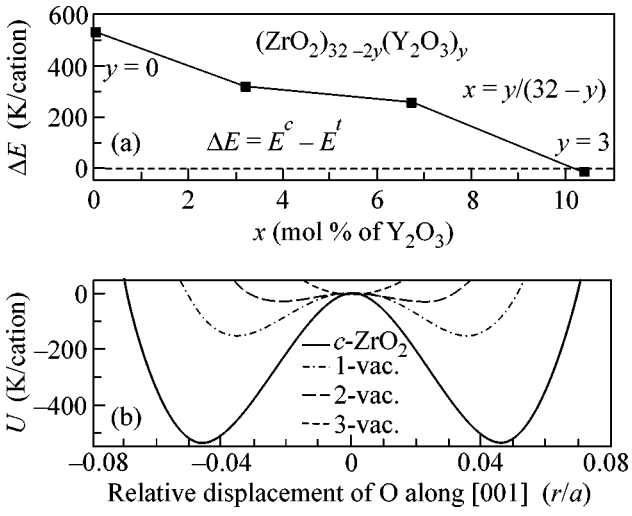

Fig. 2. Difference in the relaxed energy between the *t* and *c* configurations of YSZ, shown in panel (a). In panel (b), a decay of the double-well potential, with yttria doping, is shown as a change in energy plotted vs. the *t* displacements of the O sublattice for each concentration of Y_2O_3.

The experimental electron energy-loss near-edge shapes (ELNES), which depend on the crystal structures and the Y_2O_3 composition, can be a characterization probe of these doped oxides. *Ab initio* calculations [8] were performed to obtain the O *K*-edge ELNES in the relaxed YSZ, demonstrating that relaxation of defects plays an important role. Good agreement between calculated and measured ELNES data were obtained with respect to the number of maxima, the intensity ratios, and energy positions of the peaks [8]. This agreement shows that our modeling can reflect the realities of YSZ.

Within the "frozen phonon" method, the effective phonon potential can be calculated as the difference in energy between the perfect and distorted lattices for various amplitudes of atomic displacements according to the symmetry of the phonon considered. In doped ZrO_2, the intrinsic defects break the translational symmetry, and, therefore, one has to deal with the renormalized phonon, whose attenuation is due to the scattering by these defects [14]. Figure 2, panel (b), displays the effective potential U, calculated as a function of the O t displacements, r/a, along the z axis. The U's were shifted to the common zero energy at $r = 0$ to illustrate the development of a double-well shape. In 10 mol % Y_2O_3, U has a single minimum at $r = 0$. With decreasing Y_2O_3 content, U develops two minima; i.e., its form becomes similar to that of the X_2^- phonon in pure c-ZrO_2. The relative temperature units used give an idea of the temperature changes of the c–t interface. In fact, for practical calculations, the U's should be normalised per fluorite (4-cation) unit cell.

The modified pseudoharmonic approximation [12] was developed to calculate anharmonic dynamics of the quasi-local mode associated with the low-frequency vibrations of the defect atoms. This model was applied recently to study the structure instability in pure Fe [15] and Zr [16]. In this work, we consider the one-phonon inelastic neutron scattering spectrum, whose peak position and width determine the phonon frequency and lifetime. The spectral intensity can be calculated via the imaginary part of the one-phonon Green's function, spectral density $g_q(\omega, T)$ [14]:

$$I_q(\omega, T) \sim g_q(\omega, T) = \frac{1}{\pi}\frac{\Gamma(\omega_q, T)}{(\omega - \tilde{\omega}_q(T))^2 + \Gamma^2(\omega_q, T)}, \quad (1)$$

where $\tilde{\omega}_q(T)$ is the renormalized frequency and $\Gamma(\omega_q, T)$ is the phonon attenuation due to various scattering processes. For the latter, we restricted ourselves to the defect-dependent attenuation: $\Gamma(\omega, E) = A_x\omega(E)$, with $A_x = 0.1$, 0.15, 0.2, and 0.25 for each $x = 0$, 1, 2, and 3 concentration of Y_2O_3. The random variable E, which is the energy averaged over a characteristic period of oscillations, can be introduced [12] with its mean value $\langle E\rangle = T$ and equilibrium distribution function $\rho(E) = \exp(-E/T)/T$. The characteristic time of E variation is $\tau_E \sim 1/\Gamma \gg 1/\omega_q$; i.e., this variable is slow, as compared to the oscillation period, which allows us to calculate the frequency for each E within the pseudoharmonic approximation [12]. The partial density $g_q(\omega)$ can be obtained by averaging Eq. (1) (where the substitution of E for T is made) with distribution function $\rho(E)$.

The result might be summarized as follows: at all temperatures, there is an occasion to find (i) the basic (b) vibrations localized near minima of U, with the frequencies b close to the principal frequency ω_0 ($m\omega_0^2 = \partial^2U(r)/\partial r^2\big|_{r = r_{\min}}$), and (ii) the excited (e) overbarrier vibrations with $\omega_e \simeq \omega_0/2$. With increasing temperature, the portion of the b vibrations diminishes, $c_b = 1 - \exp(-E_c/T)$ (E_c is the "local transition" energy [12]), while the share of e vibrations increases, $c_e = 1 - c_b$. New harmonics therewith arise, which lead to a shift of the peaks and some changes of their anharmonic broadening. The basic vibration peak moves toward the low-frequency range, while the e peak moves toward the high-frequency range. These findings are in qualitative agreement with previous numerical results [17], which describe the anharmonic mode dynamics using the arbitrary potential and oscillator attenuation.

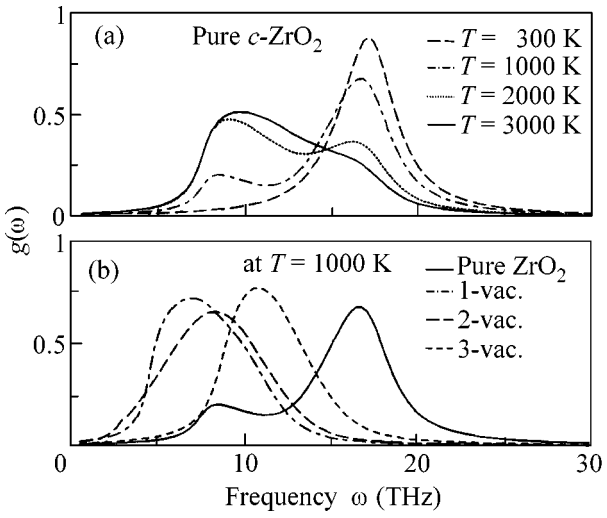

Fig. 3. Spectrum of the soft-phonon mode in pure c-ZrO_2 at different temperatures, plotted in panel (a), and its changes in YSZ with yttria doping, which are shown in panel (b).

In pure ZrO_2, the $g_q(\omega)$ plotted in panel (a) of Fig. 3 shows the b peak at room temperature, as it would be in the t phase. At intermediate temperatures, the b peak and e peak are clearly resolved. With increasing temperature, the intensity of the b peak drops, and, finally, at $T = 3000$ K the cubic-like e vibrations become dominant. In pure material, the calculated ω_e of ~10 THz is a rather reasonable value compared to the acoustic phonon branches observed in this point of the Brillouin zone [10]. Figure 3, panel (b), shows the $g_q(\omega)s$ at $T = 1000$ K. At this temperature, the b vibrations are

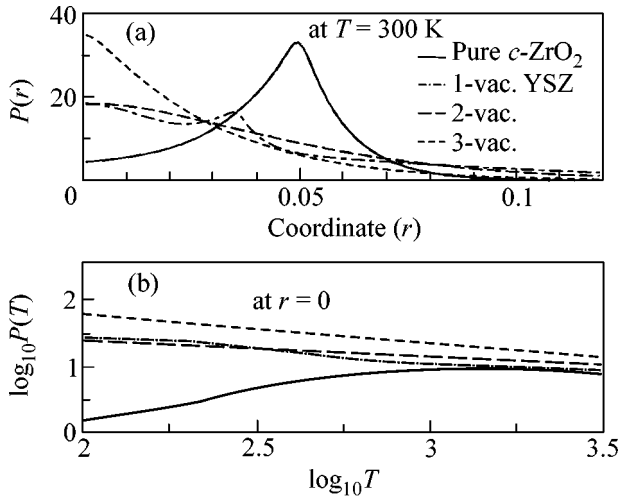

Fig. 4. The displacement probability densities $P(T, r)$: the room-temperature *Ps* ranging between 0 and 10 mol % Y_2O_3, which are plotted in panel (a), and the zero-coordinate *Ps*, shown in panel (b).

dominant in pure ZrO_2 exclusively. In YSZ, the $g_q(\omega)$*s*, shown in this panel for each defective cell, illustrate the evolution in shape with increasing Y_2O_3. This fine structure in the $g_q(\omega)$ shape of the soft phonon, responsible for the $c \longrightarrow t$-phase transition in YSZ, indicates that both these phases may coexist at intermediate temperatures.

Since, within the framework of the method used, the arbitrary parameter $\Gamma(\omega, E)$ cannot be estimated, it would be desirable to consider a $\Gamma(\omega, E)$-independent function other than $g_q(\Gamma)$. It might be the displacement probability density [18] (DPD):

$$P(r) = \int P_{\text{harm}}(r, E)\rho(E)dE, \qquad (2)$$

where

$$P_{\text{harm}}(r, E) = \sqrt{\frac{C(E)}{2\pi}}\exp\left\{\frac{-[r - r_0(E)]^2 m\omega^2(E)}{2k_B E}\right\}, \quad (3)$$

and $C(E) = m\omega^2(E)/k_B E$. In panel (a) of Fig. 4, the DPD, plotted for pure and defect zirconias, displays a change in the $P(r)$ shape at room temperature. In pure ZrO_2 and single-vacancy YSZ, the DPD shows a peak in the region of the *b* vibrations, which illustrates the room-temperature instability of the *c* configuration. The temperature dependence of DPD at $r = 0$ is shown in panel (b). In the di- and tri-□ cells, the $\log_{10}P$ vs. $\log_{10}T$ at $r = 0$ is almost linear showing the decreasing trend with increasing temperature. In pure ZrO_2 and 3 mol % ZrO_2-Y_2O_3, there is a low-temperature peak of $\log_{10}P_{r=0}$ and then, with increasing temperature, the linear behavior against $\log_{10}T$ appears. In ZrO_2, such a form of DPD starts at ~2500 K, i.e., close to the $t \longrightarrow c$-transition temperature observed, whereas the 3 mol % Y_2O_3 shows the room temperature characteristic value. Note that, at this point, the lattice dynamics become unchangeable with variation of $U(r)$ near its bottom ($T \gg E_b$).

In summary, the calculated DPD features of YSZ are in very good agreement with experiment. This fact suggests that the zero-coordinate DPD, $P_{r=0}(T)$, can be used as a quantitative criterion for stability in zirconia-stabilized materials. This report can be considered as a first attempt to get some insight into whether the *t* and *c* phases can coexist in YSZ. It would be worthwhile to apply this model to investigate the low-temperature stability in other doped metal oxides.

We thank Mike Finnis, Alan Craven, and Ali Alavi for their interest in this work. This work was supported in part (E.S.) by the Russian Foundation for Basic Research (project nos. 01-02-96463 and 00-02-17426).

REFERENCES

1. E. C. Subbarao, in *Science and Technology of Zirconia*, Ed. by A. H. Heuer and L. W. Hobbs (American Ceramic Society, Columbus, 1981), Advances in Ceramics, Vol. 3.
2. S. Fabris, A. T. Paxton, and M. W. Finnis, Phys. Rev. B **63**, 94101 (2001).
3. Ping Li, I-Wei Chen, J. E. Penner-Hahn, *et al.*, Phys. Rev. B **48**, 10063 (1993); **48**, 10082 (1993).
4. G. Stapper, M. Bernasconi, N. Nicoloso, and M. Parinello, Phys. Rev. B **59**, 797 (1999).
5. J. P. Goff, W. Hayes, S. Hull, *et al.*, Phys. Rev. B **59**, 14202 (1999).
6. A. Bogicevic, C. Wolverton, G. M. Crosbie, and E. B. Stechel, Phys. Rev. B **64**, 14106 (2001).
7. M. W. Finnis and A. T. Paxton, Phys. Rev. Lett. **81**, 5149 (1998).
8. S. Ostanin, A. J. Craven, D. W. McComb, *et al.*, Phys. Rev. B **62**, 14728 (2000).
9. F. Detraux, Ph. Chosez, and X. Gonze, Phys. Rev. Lett. **81**, 3297 (1998).
10. D. W. Liu, C. H. Perry, A. A. Feinberg, and R. Currat, Phys. Rev. B **36**, 9212 (1987); D. N. Argyriou and M. M. Elcombe, J. Phys. Chem. Solids **57**, 343 (1996).
11. Y.-Y. Ye, Y. Chen, K.-M. Ho, and B. N. Harmon, Phys. Rev. Lett. **58**, 1769 (1987).
12. E. I. Salamatov, Phys. Status Solidi B **197**, 323 (1996); **177**, 75 (1993).
13. A. Alavi, J. Kahonoff, M. Parrinello, and D. Frenkel, Phys. Rev. Lett. **73**, 2599 (1994).
14. A. A. Maradudin and A. E. Fein, Phys. Rev. **128**, 2589 (1962).
15. S. A. Ostanin and E. I. Salamatov, J. Phys.: Condens. Matter **9**, 37063 (1997).
16. S. A. Ostanin, E. I. Salamatov, and V. Yu. Trubitsin, Phys. Rev. B **57**, 5002 (1998); **58**, R15962 (1998).
17. Yu. N. Gornostyrev, M. I. Katsnelson, A. V. Trefilov, *et al.*, Phys. Rev. B **54**, 3286 (1996); C. A. Condat and P. W. Lamberti, Phys. Rev. B **53**, 8354 (1996).
18. S. Aubry, J. Chem. Phys. **62**, 3217 (1975).

JETP Letters, Vol. 74, No. 11, 2001, pp. 556–558. Translated from Pis'ma v Zhurnal Éksperimental'noĭ i Teoreticheskoĭ Fiziki, Vol. 74, No. 11, 2001, pp. 630–632.

Polaron Hopping Conduction in $La_{0.85}Sr_{0.15}MnO_3$ Single Crystal

É. A. Neĭfel'd*, V. E. Arkhipov, N. A. Tumalevich, and Ya. M. Mukovskii[1]

Institute of Metal Physics, Ural Division, Russian Academy of Sciences, ul. S. Kovalevskoĭ 18, Yekaterinburg, 620219 Russia
**e-mail: neifeld@imp.uran.ru*
[1]Moscow Institute of Steel and Alloys, Leninskiĭ pr. 4, Moscow, 117939 Russia

Received October 25, 2001

Temperature dependences of electrical resistance and thermopower of a $La_{0.85}Sr_{0.15}MnO_3$ single crystal were measured in the paramagnetic and ferromagnetic dielectric phases. It was shown that charge transfer in both phases is due to the variable-range polaron hopping over the localized states. The activation energies in both phases linearly depend on $T^{3/4}$ but differ from each other by a constant which is approximately equal to the exchange energy kT_c. The results obtained are in compliance with the concept of percolation character of metal–insulator transition in manganites. © *2001 MAIK "Nauka/Interperiodica".*

PACS numbers: 72.15.Jf; 72.20.Ee; 71.38.-k

Electrical conduction in the dielectric phase of lanthanum manganites above the Curie temperature is explained either by the activation of charge carriers to the mobility edge [$\rho \sim \exp(\varepsilon/kT)$] [1] or by hopping of small adiabatic polarons between the localized states [$\rho \sim T^*\exp(\varepsilon/kT)$] [2] or variable-range polaron hopping [$\rho \sim \exp(T_0/T)^{1/4}$] [3]. In all cases, the conclusions about the conduction mechanism are customarily justified by the possibility of the linear extrapolation of the logarithmic dependence of resistance on T^{-1} or $T^{-1/4}$. However, such a procedure of processing experimental results is not always unambiguous, because the temperature interval of activated conduction changes by only 1.5–2 times, while the resistance usually changes by less than an order of magnitude. For example, the experimental dependence $\rho(T)$ discussed below can be satisfactorily approximated at T = 360–280 K by a linear function of both T^{-1} and $T^{-1/4}$.

This work reports the results of studying the conduction mechanism at the portions of the temperature curve for electrical resistance above and below the Curie temperature of a $La_{0.85}Sr_{0.15}MnO_3$ single crystal, which is compositionally at the dielectric border of the metal–insulator transition in this system. This crystal is paramagnetic dielectric (PMD) above the Curie temperature and ferromagnetic dielectric (FMD) below it. The resistance was measured over the temperature range 4.2–420 K using a four-probe scheme. While measuring thermopower at 100–420 K, the sample was in a vacuum; the temperature was measured by copper–constantan thermocouples, and the emf was measured between their copper terminals. Indium leads were soldered to the sample using an ultrasonic solderer.

The temperature dependences of resistivity (ρ) and thermopower (S), and the Curie (T_c) and charge-ordering (T_{co}) temperatures were determined for the sample from the magnetometric and neutron diffraction data [4] and are shown in Fig. 1. Hysteresis at T = 360–380 K corresponds to the transition from the high-temperature rhombohedral phase to the low-temperature orthorhombic phase.

Let us first analyze the temperature dependences $\rho(T)$ and $S(T)$ in the temperature interval between the structural transition and the Curie temperature, i.e., in the PMD phase. Assuming that the charge transfer is accomplished by small-radius polarons in the adiabatic regime, we use the expression $\rho \sim AT\exp(\varepsilon_\rho/kT)$ for $\rho(T)$ and $S = k/\exp(\varepsilon_s/kT + B)$ for the thermopower. Figure 2 shows the temperature dependences $\varepsilon_\rho(T)$ and $\varepsilon_s(T)$ calculated as $\varepsilon_\rho = d(\ln(\rho/T))/d(T^{-1})$ and $\varepsilon_s = dS/d(T^{-1})$ from the experimental data. One can see, first, that the activation energies determining the behav-

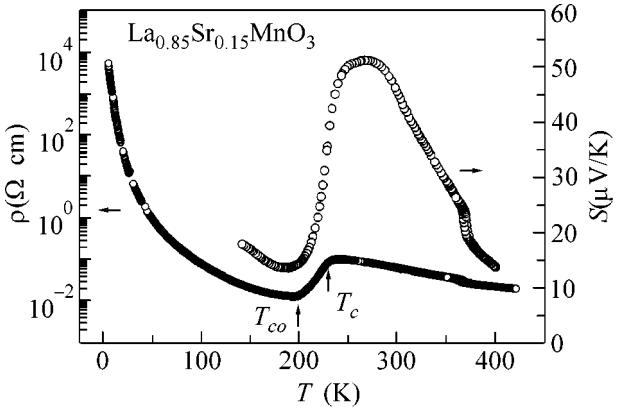

Fig. 1. Temperature dependences of electrical resistivity and thermopower for $La_{0.85}Sr_{0.15}MnO_3$. T_c is the Curie temperature, and T_{co} is the charge-ordering temperature.

ior of the thermopower and resistivity differ by more than a factor of three and, second, that the activation energy ε_ρ decreases monotonically with temperature, while ε_s remains constant in the same temperature interval. It is known [5] that, in the case of carrier activation from the localized states to the mobility edge, ε_ρ does not depend on temperature and $\varepsilon_s = \varepsilon_\rho$, while, for the polaron hopping conduction, $\varepsilon_\rho = \varepsilon_s + W$, where W is the energy necessary for the polaron jump. For this reason, the experimental data presented in Fig. 2 imply that the conduction of $La_{0.85}Sr_{0.15}MnO_3$ in this temperature interval is due to the variable-range polaron hopping over the localized states (VRH mechanism).

Next, let us consider the temperature dependence of resistivity in the FMD phase at 4.2–130 K. Contrary to the activated conduction at $T > T_c$, where temperature varies only ~1.5-fold, while the resistivity varies ~5-fold, the temperature in this interval changes by approximately a factor of 40, and the resistivity of the sample increases by three orders of magnitude. Therefore, a clearly defined linear dependence of $\ln\rho(T_0/T)^{1/4}$ unambiguously points to the VRH conduction in this temperature interval. Nevertheless, to analyze the activation energy, we determined $\varepsilon_\rho(T)$ in the same manner as was done above at $T > T_c$. Inasmuch as the VRH activation energy depends on temperature as [6]

$$\varepsilon_a(T) = \frac{(kT)^{3/4}}{(N(\varepsilon_F)a^3)^{3/4}}, \qquad (1)$$

where $N(\varepsilon_F)$ is the density of states at the Fermi level and a is the radius of localized state, the experimentally measured ε_ρ is plotted in Fig. 3 as a function of $T^{3/4}$ for both temperature intervals of activated conduction. In accordance with Eq. (1), ε_ρ depends linearly on $T^{3/4}$, with the slopes of straight lines being virtually the same for the PMD and FMD phases and corresponding to $N(\varepsilon_F)a^3 = 0.2$ eV^{-1}, while the temperature-independent difference between them is ~24 meV, i.e., approximately equal to the exchange energy $kT_c = 20$ meV. This suggests that the conduction mechanism and the density of localized states near the Fermi level are the same in both PMD and FMD phases. A constant difference in activation energies (~24 meV) indicates that both lattice and magnetic interactions are involved in the polaron formation. In the ferromagnetic phase, the polaron hops between the centers with the same direction of magnetic moment. Because of this, the activation energy in this phase is lower than in the paramagnetic phase by a value approximately equal to the exchange energy.

On the whole, the temperature dependence of electrical conduction of $La_{0.85}Sr_{0.15}MnO_3$ in the orthorhombic phase can be described as follows. As the temperature decreases, the charge transfer obeys the VRH mechanism immediately after the structure transition to the PMD phase, and the activation energy depends on

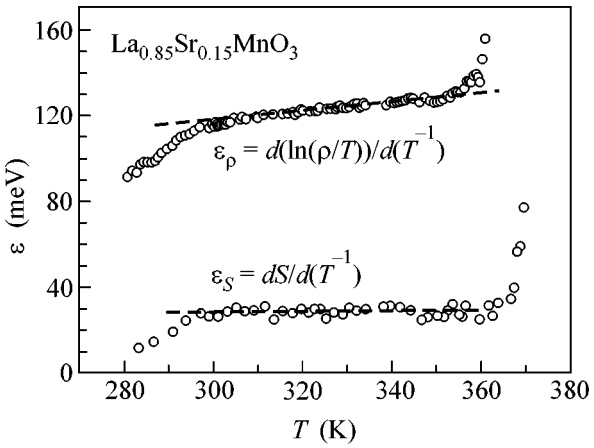

Fig. 2. Temperature dependences of activation energies derived from the electrical resistivity (ε_ρ) and thermopower (ε_s) for the paramagnetic dielectric phase.

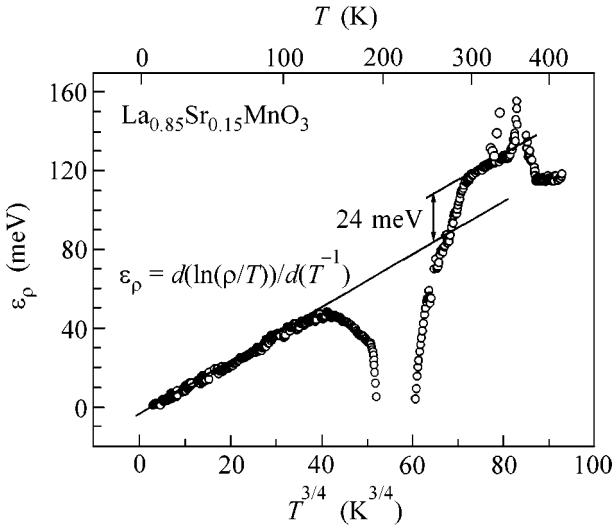

Fig. 3. Temperature dependences of activation energies ε_ρ for the paramagnetic and ferromagnetic dielectric phases.

both lattice and magnetic interactions. Near the Curie temperature, the resistance of the sample sharply drops because of the formation of metallic clusters. The clustering is caused by the inhomogeneous distribution of strontium in the sample, as is evident from the neutron diffraction data. A superstructural reflection observed in the neutron diffraction pattern near T_{co} corresponds to the charge ordering in the composition with $x = 0.125$, although the stoichiometric value is $x = 0.15$ [6]. This signifies that the strontium-deficient domains exist in the sample in an amount sufficient for the appearance of the superstructural reflection; hence, the domains with $x > 0.15$, where metallic conduction appears, are also present in the sample. However, the growth of the metallic phase is not completed in the formation of a singly connected metallic cluster. For this reason, after

the metallization process is terminated upon further decrease in temperature, the temperature dependence of resistance is determined by the dielectric ferromagnetic phase, because the resistance of the metallic phase is virtually independent of temperature [7]. In this phase, the charge carriers and the conduction mechanism are the same as in the paramagnetic phase, but the activation energy is lower by a value equal to approximately kT_c.

We are grateful to A.S. Moskvin for discussing the experimental results and to A.V. Korolev for measuring Curie temperature on a SQUID magnetometer. This work was supported by the Russian Foundation for Basic Research, project no. 99-02-16280.

REFERENCES

1. N. G. Bebenin, R. I. Zaĭnullina, V. V. Mashkautsan, *et al.*, Zh. Éksp. Teor. Fiz. **117**, 1181 (2000) [JETP **90**, 1027 (2000)]; R. I. Zaĭnullina, N. G. Bebenin, V. V. Mashkautsan, *et al.*, Zh. Éksp. Teor. Fiz. **120**, 139 (2001) [JETP **93**, 121 (2001)].
2. M. Jaime, P. Lin, S. H. Cyun, *et al.*, Phys. Rev. B **60**, 1028 (1999); D. C. Worledge, L. Mieville, T. H. Geballe, *et al.*, Phys. Rev. B **57**, 15267 (1998).
3. M. Jaime, M. B. Salamon, K. Pettit, *et al.*, Appl. Phys. Lett. **68**, 1576 (1996).
4. S. F. Dubinin, V. E. Arkhipov, V. E. Naĭsh, *et al.*, Fiz. Met. Metalloved. **93** (3) (2002) (in press).
5. N. F. Mott and E. A. Davis, *Electronic Processes in Noncrystalline Materials* (Clarendon, Oxford, 1971; Mir, Moscow, 1974).
6. B. I. Shklovskiĭ and A. L. Efros, *Electronic Properties of Doped Semiconductors* (Nauka, Moscow, 1979; Springer-Verlag, New York, 1984).
7. A. Urushibara, Y. Moritomo, T. Arima, *et al.*, Phys. Rev. B **51**, 14103 (1995).

Translated by V. Sakun

JETP Letters, Vol. 74, No. 11, 2001, pp. 559–563. Translated from Pis'ma v Zhurnal Éksperimental'noĭ i Teoreticheskoĭ Fiziki, Vol. 74, No. 11, 2001, pp. 633–637.

On a Simple Model of the Photonic or Phononic Crystal

A. M. Kosevich

Verkin Physicotechnical Institute of Low Temperatures, National Academy of Sciences of Ukraine, Kharkov, 61164 Ukraine
kosevich@ilt.kharkov.ua

Received October 11, 2001; in final form, November 8, 2001

A model is proposed for a one-dimensional dielectric or elastic superlattice (SL) that relatively simply describes the frequency spectrum of electromagnetic or acoustic waves. The band frequency spectrum is reduced to minibands contracting with increasing frequency. A procedure is suggested for obtaining local states near a defect in a SL, and the simplest of these states is described. Conditions for the initiation of Bloch oscillations of a wave packet in a SR are discussed. © *2001 MAIK "Nauka/Interperiodica".*

PACS numbers: 42.70.Qs; 63.20.Dj

1. By a photonic crystal is meant a macroscopic periodic structure composed of two spatially alternating dielectrics differing in dielectric constants (velocities of electromagnetic waves) [1]. Analogously, by a phononic crystal or acoustic superlattice (SL) is meant a periodic structure composed of two alternating elastic materials differing in elastic moduli and velocities of sound (the general acoustics theory of layered media is expounded in [2], and a useful bibliography on acoustic SLs is given in one of the last publications [3]). A great number of publications are devoted to studying the frequency spectrum of SLs. It is clear that, in the general case, this spectrum is extremely complicated and contains a system consisting of both a great number of eigenfrequency bands and gaps corresponding to forbidden frequencies of eigenmodes. In order to characterize such spectra qualitatively and to illustrate their main quantitative features, it would be appropriate to use simple models that allow for these features. The well-known 1D Kronig–Penney model [4] may serve as an example of such a model in the electronic theory of crystals. In this work, a model of a SL is proposed that provides an analytical description of the high-frequency part of its spectrum and suggests a possible implementation of an interesting acoustic SL.

Consider a SL in the form of alternating plane-parallel layers of two materials differing in either elastic or dielectric (depending on the implementation of interest) characteristics. Denote the layer thicknesses by d_1 and d_2; then, the SL period equals $d = d_1 + d_2$. The elastic or electromagnetic field inside each material, which is assumed to be isotropic, is described by the wave equation

$$\frac{\partial^2 u^\alpha}{\partial t^2} - c_\alpha^2 \frac{\partial^2 u^\alpha}{\partial x^2} = 0, \quad \alpha = 1, 2, \tag{1}$$

where c_α is the wave velocity in the layer of the α type. The velocity of light in a dielectric equals $c_\alpha = c/\sqrt{\varepsilon_\alpha}$ (c is the velocity of light in free space), and that in an elastic medium equals $c_\alpha = \sqrt{\mu_\alpha/\rho_\alpha}$; ε_α, μ_α and ρ_α (α = 1, 2) are dielectric constants,[1] elastic moduli, and mass densities, respectively.

Consider a wave propagating along the X axis perpendicular to the layers. In this case, waves of two possible polarizations do not interact, and it is possible to study scalar fields $u^{(\alpha)}$ (α = 1, 2).

The standard boundary conditions will be formulated as applied to the acoustic problem. The displacements $u^{(\alpha)}$ and stresses $\sigma^\alpha = \mu_\alpha(\partial u^{(\alpha)})/\partial x$ at the layer boundaries will be considered continuous. It is known that, by virtue of the periodicity of a structure with a period of d, eigenmodes can be characterized by a quasi-wave number k, considering that the field in a unit cell with the number n takes the form

$$u_n(x) = u_0(x - nd)e^{iknd}. \tag{2}$$

The dispersion equations in this problem were obtained by Rytov for both the electromagnetic field [5] and acoustics [6]

$$\cos kd = \cos k_1 d_1 \cos k_2 d_2 - \frac{1}{2}\left(\frac{k_1}{k_2} + \frac{k_2}{k_1}\right)\sin k_1 d_1 \sin k_2 d_2, \tag{3}$$

where $k_1 = \omega/c_1$ and $k_2 = \omega/c_2$ (ω is frequency). Equation (3) determines the frequency as an implicit function of the quasi-wave number. It allows the spectrum of long-wavelength vibrations ($kd \ll 1$) to be described readily, for which a sound spectrum with averaged elas-

[1] Because I am interested mainly in narrow frequency bands, the frequency dispersion of ε can be neglected, and ε can be related to the corresponding frequencies.

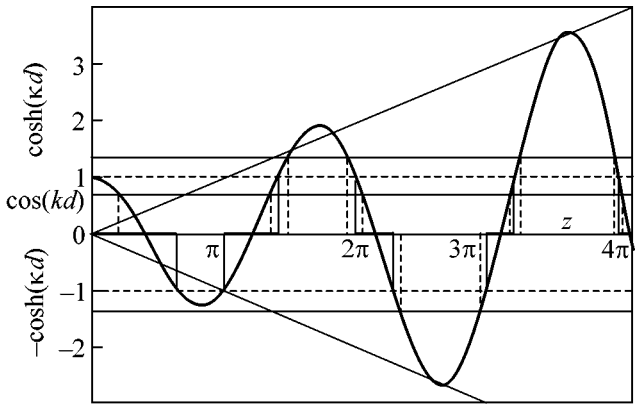

Fig. 1. Graphical solution of Eq. (7). Eigenfrequency bands are shown in heavy lines on the *z* axis.

tic moduli $\langle\mu\rangle$ and density $\langle\rho\rangle$ is naturally obtained. It was shown [6] that

$$\langle\rho\rangle d = \rho_1 d_1 + \rho_2 d_2; \quad \frac{d}{\langle\mu\rangle} = \frac{d_1}{\mu_1} + \frac{d_2}{\mu_2}. \tag{4}$$

The relationship for $\langle\mu\rangle$, which contains only d_α/μ_α ratios, is curious. A limiting case that is commonly of no interest in the dynamics of a quantum particle can be considered based on this relationship. Consider the limit $d_2 \longrightarrow 0$ and $\mu_2 \longrightarrow 0$ at $d_2/\mu_2 = P = \text{const}$.[2] In this case, $d_1 \longrightarrow d$ and $k_2 d_2 = \omega d_2/c_2 = \sqrt{\rho_2 d_2}\,\omega\sqrt{d_2\mu_2} \longrightarrow 0$; therefore, Eq. (3) is reduced to the following equation:

$$\cos kd = \cos k_1 d - \frac{1}{2}P\left(\frac{\rho_2\mu_1}{\rho_1 D}(k_1 d)\right)\sin k_1 d. \tag{5}$$

It is useful to note that the dispersion law (Eq. 5) corresponds to an elastic SL composed of a chain of regularly repeating elements of length d with parameters μ_1 and c_1. The following boundary conditions are fulfilled at their joints: (1) continuity of the normal stresses $[\sigma]_-^+ = 0$, which is equivalent to $[\partial u/\partial x]_-^+ = 0$ and (2) occurrence of a jump of displacements at a soft interlayer determined by the stresses at the joint

$$[u]_-^+ = M\sigma \equiv \mu_1 M\left(\frac{\partial u}{\partial x}\right), \tag{6}$$

where $M = P(\rho_1/\rho_2)$. A set of such boundary conditions at a fixed M is used in describing capillary phenomena in solids [7] or planar defects in crystals [8]. If the parameter M is small, the system at hand is reduced to a periodic sequence of elastic sections weakly bound together. A chain of piezoelectric sections bound together by thin vacuum interlayers may serve, for example, as a possible implementation of such a system. Then, the coupling of elastic vibrations in neighboring sections would be accomplished through electromagnetic oscillations in vacuum gaps.

To illustrate the distribution of roots $\omega = \omega(k)$ of Eq. (5), this equation will be represented in the form

$$\cos kd = \cos z - Qz\sin z, \tag{7}$$

where $z = k_1 d = \omega d/c_1$ and $Q = P(\rho_2\mu_1/2\rho_1 d)$. Consider the graphical construction in Fig. 1. The figure shows a plot of the right-hand side of Eq. (7). When it runs over values between ±1, the roots of the equation run over values within intervals marked off on the abscissa axis.

Note that the allowed frequencies are localized in contracting intervals at values $k_1 d = \pm m\pi$, where m is a large integer, as z increases.[3] Under the condition that $m^2 Q \gg 1$, the dispersion laws in these intervals take the form

$$\omega = m\omega_0 + \frac{2\Omega}{m}\begin{cases}\sin^2(kd/2), & m = 2p+1;\\ \cos^2(kd/2), & m = 2p,\end{cases} \tag{8}$$

where $\omega_0 = \pi c/d$ and $\Omega = c/\pi Q d$. It is clear that Eq. (8) gives the size quantization phonon spectrum in a layer of thickness d, whose levels are split into minibands because of low "transparency" of interlayer boundaries. An attempt to analyze the character of the SL band spectrum was made in [9], where the dispersion relation (Eq. (3)) was derived once again. However, their analysis is not satisfactory in a limiting case close to that considered in this work, because it leads to the conclusion that the miniband widths do not vary with increasing frequency.

Consider Eq. (8) from another point of view: Eq. (8) describes the spectrum of a pseudo-quantum particle for which the Schrödinger equation within the tight-binding model takes the form (for $m = 2p + 1$)

$$i\frac{\partial\psi_n}{\partial t} = m\omega_0\psi_n - \frac{\Omega}{m}(2\psi_n - \psi_{n+1} - \psi_{n-1}) \tag{9}$$

or (for $m = 2p$)

$$i\frac{\partial\psi_n}{\partial t} = m\omega_0\psi_n + \frac{\Omega}{2m}(2\psi_n + \psi_{n+1} + \psi_{n-1}). \tag{9a}$$

Actually, Eqs. (9) and (9a) are equations for the envelop curve of SL vibrations taken at discrete points (at joints). As usual, the order of the derivative with respect to time decreases in such equations. These equations describe analytically the dynamics of a wave packet corresponding to the allowable high frequencies. Using the explicit form of the dispersion laws (Eq. (6)) and simple Eqs. (7) and (8), the passage of wave packets through the system under study can be described readily, and explicit relationships can be proposed for comparison with possible experimental results.

[2] A more general case, i.e., $d_2 \longrightarrow 0$ and $c_2 \longrightarrow 0$ at $d_2/c_2 = \text{const}$, could be considered; however, no new results arise in this case.

[3] The contraction of bands with increasing frequency was also noted previously; in particular, this was mentioned in [3].

Nonlinear effects in optical SLs associated with the dependence of the refraction coefficient (that is, the velocity of light c and the parameter ω_0) or the characteristic of joints Q on the field strength ψ_n can be readily taken into account using Eqs. (9) and (9a), as was done in [10] when describing optical solitons in such SLs.

The frequencies of forbidden bands correspond to displacements of the type $u_n \sim e^{\mp\kappa nd}$ (when $k = i\kappa$) or $u_n \sim (-1)^n e^{\mp\kappa nd}$ (when $k = i\kappa + \pi$), which drop (grow) with increasing displacement number n. The frequency dependence of the parameter κ for solutions of the first type can be found from the relationship

$$\cosh\kappa d = \cos z - Qz\sin z > 1, \tag{10}$$

and, for solutions of the second type, from the relationship

$$-\cosh\kappa d = \cos z - Qz\sin z < -1. \tag{10a}$$

It is clear that such states have a physical meaning only in the x semiaxis under the condition that a solution vanishing at infinity and corresponding to certain boundary conditions at the origin is selected. Solutions of the first and the second types correspond to frequencies in the intervals $(2p-1)\pi < z < 2p\pi$ and $2p\pi < z < (2p+1)\pi$, respectively, (see Fig. 1). The necessity of using exponentially decreasing solutions arises in describing displacements in the vicinity of a local SL defect.

2. We assume that the boundary conditions at one of the joints (let its number $n = 0$) differ from those described above; or, more specifically, these conditions differ in the parameter M: $M^* \neq M$. The local vibration frequency is essentially determined by the difference $M^* - M = \xi M$. Calculations show that the boundary condition at the defect leads to the relationship

$$\sinh\kappa d = \xi Qz\sin z, \tag{11}$$

which, along with Eq. (10) or (10a) (depending on the sign of ξ) gives the local vibration frequency. The local frequencies are determined by the intersection points of plots of the right-hand sides of Eqs. (10) and (10a) with the plot of the function $f(z) = \sqrt{1+\sinh^2 z} = [1 + (\xi Qz)^2\sin^2 z]^{1/2}$, which is determined by Eq. (11). Because $\kappa > 0$, the solutions correspond to the frequencies (values of z) determined by the equation (see Fig. 2)

$$\cos z - Qz\sin z = \operatorname{sgn}\{\xi Qz\sin z\}\sqrt{1+(\xi Qz)^2\sin^2 z}. \tag{12}$$

The local vibration frequencies corresponding to different signs of ξ are located in alternating intervals between $z = 2p\pi$ and $z = (2p+1)\pi$ ($p = 0, 1, 2, \ldots$): $\omega = \omega_s$, $s = 1, 2, 3, \ldots$. The corresponding solutions can be presented in the standard form $u_n(x, t) = w_n(x)\exp\{-i\omega t\}$, where $w_n(x)$ is an odd function ($w_{-n}(-x) = w_n(x)$) of the following form (see Fig. 3):

$$\begin{aligned} w_0^{(s)}(x) &= a_0\cos(k_1^{(s)}x - \theta_s), \quad 0 < x < d; \\ w_n^{(s)}(x) &= a_1\cos(k_1^{(s)}x - \theta_s)e^{-\kappa nd}, \\ & nd < x < (n+1)d, \quad n \geq 1; \end{aligned} \tag{13}$$

where θ_s is the constant phase corresponding to the eigenfrequency ω_s. The function $w_1(\xi)$ depends harmonically on the argument and can easily be found.

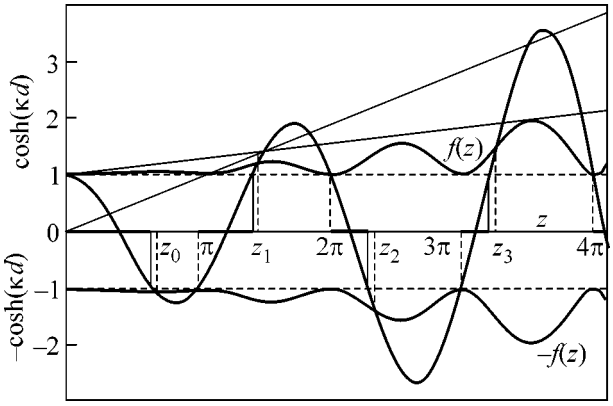

Fig. 2. Determining a series of roots of Eq. (12) graphically: roots z_0, z_2, … and z_1, z_3, … correspond to two types of vibrations.

In this case, the local vibrations for which $(2p-1)\pi < z < 2p\pi$ (points z_2 and z_4 in Fig. 2) are described by a monotonic function decreasing with increasing number of the unit cell, and the vibrations with frequencies $2p\pi < z < (2p+1)\pi$ ((points z_1 and z_3 in Fig. 2) are described by a function proportional to $(-1)^n e^{-\kappa nd}$. It is essential that a local vibration may arise at any sign of the perturbation ξ.

A local vibration with an even eigenfunction cannot arise at a defect localized at one boundary at any sign of ξ. Assume that this is a joint with $n = 0$; at this joint, $[u]_-^+ = 0$ and $\sigma_0 = 0$; therefore, an excitation in the form of a standing wave with an even dependence on the x coordinate is not sensitive to the value of the parameter Q at the joint $n = 0$ and does not differ from the vibration of the free SL boundary passing along this joint. The free SL boundary corresponds to a section through the joint $n = 0$. This is equivalent to the condition $\sigma_0 = 0$, which is obtained in the given model at $\xi = \infty$ ($M^* = \infty$). It follows from Eq. (13) that only uniform vibrations ($\kappa = 0$) are possible in this case at frequencies $\omega = (c/d)\pi m$, $m = 0, 1, 2, \ldots$. Hence, no localized wave exists at the free SL end. This means that vibrations of the even type are impossible if the defect is lumped at one joint. Such localized excitations arise upon variation (perturbation) of the parameter M at least at two neighboring joints. As in the case of an odd solution,

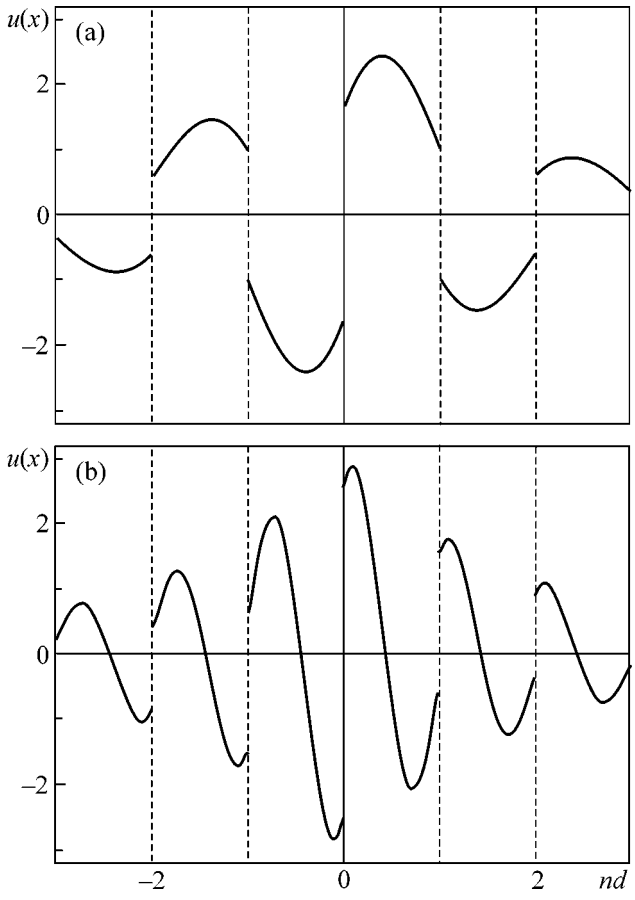

Fig. 3. Coordinate dependence of displacements of a SL in the vicinity of a defect for two types of vibrations consistent with roots in Fig. 2: (a) corresponds to z_0, z_2, … roots (antiphase vibrations of unit cells) and (b) corresponds to z_1, z_3, … roots (in-phase vibrations of unit cells).

the regions of occurrence of such local vibrations with in-phase and antiphase displacements of neighboring unit cells alternate, depending on the sign of ξ, with the period $\Delta z = \pi$.

3. It is interesting to discuss the possibility of occurrence and experimental observation of Bloch oscillations of a wave packet in the SL under consideration. Bloch oscillations of an optical pulse in a different situation were described and observed experimentally [11, 12]. Therefore, this discussion is not groundless.

We assume that the physical characteristics of the constituent SL elements weakly depend on the number n, for example, $c = c_0 + \Delta c = c_0\{1 + \delta c/c_0\}$, where Δc is a small change in the wave velocity in passing from one element to the next one (in the experiments [10, 11], such a nonuniformity was created by a temperature gradient using the temperature dependence of the refraction coefficient of the dielectric). Then, the parameter ω_0 in Eqs. (8), (9), and (9a) should be changed as follows:

$$m\omega_0 = \Omega_n \equiv \Omega_0 + \eta nd, \tag{14}$$

where η is a small gradient of the fundamental frequency. In the case of $m = 2p + 1$ (the case of $m = 2p$ is analyzed in a similar way), this results in the Schrödinger equation in a uniform field

$$i\frac{\partial\psi_n}{\partial t} = \Omega_0\psi_n + \eta nd\psi_n + \frac{\Omega}{2m}(2\psi_n - \psi_{n+1} - \psi_{n-1}), \tag{15}$$

and the expression given by Eq. (8) is transformed to the Hamiltonian of the particle under consideration determined as a function of n and k. Actually, Eq. (15), as well as (9), determines the envelop function of vibrations at the fundamental frequency.

We introduce an operator of the site number, which takes the form $n = i/d\ \partial/\partial k$ in the one-band model.[4] Then, Eq. (15) in the k representation takes the form consistent with the above Hamiltonian

$$i\frac{\partial\psi(q)}{\partial t} = \Omega_0\psi(q) + i\eta\frac{\partial\psi(q)}{\partial q} + \frac{2\Omega}{m}\sin^2(q/2)\psi(q), \tag{16}$$

where the designation $q = kd$ is used. A particle governed by Eq. (15) or (16) is subjected to so-called dynamic localization [14], which is manifested in a peculiar kind of oscillation with a frequency that can be determined from the following considerations. The time and the wave number enter into Eq. (16) for the stationary states as the combination $q + \eta t$. Because the stationary eigenfunction in this case is a periodic function q with a period of 2π, it corresponds to an equidistant frequency spectrum with the characteristic frequency

$$\omega_B = \eta = m\Delta\omega_0 = m\omega_0\frac{\Delta c}{c} = m(\pi c/d)\frac{\Delta c}{c}. \tag{17}$$

This is just the Bloch oscillation frequency of the wave packet in the SL.

An analysis of the evolution of a wave packet experiencing Bloch oscillations is outlined, for example, in the reviews [15, 16]. The character of Bloch oscillations depends essentially on the packet width. A packet with a very narrow Fourier k spectrum (with well-defined k) behaves as a particle whose Hamiltonian

[4] One own band of frequencies corresponds to each m. The question of the role of interband transitions in the theory of Bloch oscillations was discussed in the literature [13]. Only one frequency participates in the model of the tight-binding type considered in this work. The occurrence of interband interactions in the similar model of a nonlinear optical SL was taken into account when the stability of autolocalized vibrations of the band-gap (solitons) was analyzed [10].

coincides with the right-hand side of Eq. (8) given Eq. (14). The center of gravity of the packet executes vibrations with the frequency ω_B and the amplitude $A = \Omega d/m\eta$. If the initial packet ($t = 0$) is very narrow in the x space (for example, is localized at one site $n = 0$), its dynamics is different: with increasing time, the excitation propagates in both directions from $n = 0$; however, when reaching the distance A, it stops and "rolls" back, assembling into the initial pulse at the instant $t = 2\pi/\omega_B$, that is, in the period of Bloch oscillations.

It is likely that the estimations of the Bloch frequency $\omega_B \sim m(c/d)(\Delta c/c)$ and the amplitude $A \sim d(m^2Q\Delta c/c)^{-1}$ leave room for their observation in acoustic SLs.

The author is grateful to Vladimir Al'shits, Andreas Mayer, and Él' Ganapol'skiĭ for useful discussions, to Marina Mamaluĭ and Vladimir Grishaev for help with calculations and preparation of figures, and to the Max Planck Institute for the Physics of Complex Systems (Dresden) for hospitality and beautiful working conditions. This work was partly supported by INTAS (INTAS open call 1999, project no. 167).

REFERENCES

1. J. D. Joannopulos, R. D. Meade, and J. N. Win, *Photonic Crystals* (Prinston Univ. Press, Princeton, 1995).
2. L. M. Brekhovskikh, *Waves in Layered Media* (Nauka, Moscow, 1973; Academic, New York, 1980).
3. Pi-Gang Luan and Zhen Ye, Phys. Rev. E **63**, 66611 (2001).
4. R. de L. Kronig and W. G. Penni, Proc. R. Soc. London, Ser. A **130**, 499 (1931).
5. S. M. Rytov, Zh. Éksp. Teor. Fiz. **29**, 605 (1955) [Sov. Phys. JETP **2**, 466 (1956)].
6. S. M. Rytov, Akust. Zh. **2**, 71 (1956) [Sov. Phys. Acoust. **2**, 68 (1956)].
7. A. F. Andreev and Yu. A. Kosevich, Zh. Éksp. Teor. Fiz. **81**, 1435 (1981) [Sov. Phys. JETP **54**, 761 (1981)].
8. L. J. Pyrak-Nolte, J. Xu, and G. M. Haley, Phys. Rev. Lett. **68**, 3650 (1992); A. M. Kosevich and A. V. Tutov, Fiz. Nizk. Temp. **19**, 1273 (1993) [Low Temp. Phys. **19**, 905 (1993)]; A. M. Kosevich and A. V. Tutov, Phys. Lett. A **213**, 265 (1996).
9. A. Figotin and V. Gorentsveig, Phys. Rev. B **58**, 180 (1998).
10. A. A. Sukhorukov and Y. S. Kivshar, Phys. Rev. Lett. **87**, 083901 (2001).
11. N. Petsch, P. Dannberg, W. Elflein, *et al.*, Phys. Rev. Lett. **83**, 4752 (1999).
12. R. Morandotti, U. Perschel, J. S. Aitchison, *et al.*, Phys. Rev. Lett. **83**, 4756 (1999).
13. M. Gluck, A. R. Kolovski, and H. J. Korsch, Phys. Lett. A **249**, 483 (1998); Phys. Rev. Lett. **82**, 1534 (1999).
14. D. H. Dunlap and V. M. Kenkre, Phys. Lett. A **127**, 438 (1988).
15. A. M. Kosevich, Fiz. Nizk. Temp. **27**, 699 (2001) [Low Temp. Phys. **27**, 513 (2001)].
16. M. Gluck, A. R. Kolovski, and H. J. Korsch, Phys. Lett. A **249**, 483 (1998); Phys. Rep. (2001) (in press).

Translated by A. Bagatur'yants

JETP Letters, Vol. 74, No. 11, 2001, pp. 564–567. Translated from Pis'ma v Zhurnal Éksperimental'noĭ i Teoreticheskoĭ Fiziki, Vol. 74, No. 11, 2001, pp. 638–641.

Cyclotron Resonance in a Two-Dimensional Electron System with Self-Organized Antidots

S. D. Suchalkin*, Yu. B. Vasil'ev*, M. Zundel, G. Nachtwei**, K. von Klitzing**, and K. Eberl****

** Ioffe Physicotechnical Institute, Russian Academy of Sciences, St. Petersburg, 194021 Russia*

*** Max-Planck-Institut für Festkörperforschung, 70569 Stuttgart, Germany*

Received January 29, 2001; in final form, November 14, 2001

Experimental data are reported on studying cyclotron resonance in a two-dimensional electron system with an artificial random scattering potential generated by an array of self-organized AlInAs quantum islands formed in the plane of an AlGaAs/GaAs heterojunction. A sharp narrowing of the cyclotron resonance line is observed as the magnetic field increases, which is explained by the specific features of carrier scattering in this potential. The results obtained point to the formation of a strongly correlated electron state in strong magnetic fields at carrier concentrations smaller than the concentration of antidots. © *2001 MAIK "Nauka/Interperiodica".*

PACS numbers: 76.40.+b

1. In spite of the fact that cyclotron resonance (CR) is one of the most powerful experimental techniques for studying charge carrier systems in semiconductors, its application to observing effects due to electron–electron interactions is rather limited, because CR in a translationally invariant and uniform system is associated with the motion of the center of inertia, and both the position and the shape of the CR line do not depend on the relative coordinates of carriers [1].

However, the conditions of the Kohn theorem in each real system are, to a greater or lesser extent, not fulfilled, and collective effects can become "apparent" in the CR spectra because of the violation of translational symmetry due to the occurrence of a random potential [2] and by virtue of the finite nonparabolicity of the energy spectrum. A sufficiently small concentration of carriers n_s is another condition for observing correlation effects in CR, because the ratio of the potential energy associated with electron–electron interactions to the kinetic energy of an electron in a two-dimensional system grows as $n_s^{-1/2}$ with decreasing carrier concentration.

In this work, we present the results of studying CR in a two-dimensional (2D) system of carriers with an artificial random potential due to self-organized quantum "islands" formed in the plane of the 2D system of carriers. The results obtained point to the decisive role of electron–electron interactions in the formation of the CR spectrum.

2. Samples used in the experiment consist of an inverted single AlGaAs/GaAs heterojunction with an array of self-organized quantum AlInAs islands formed in the junction plane at the AlGaAs surface. The position of the conduction band bottom in AlInAs is higher in energy than that in GaAs; therefore, the "islands" serve as antidots, creating a short-range repulsive potential for electrons in GaAs. STM and AFM data indicate that the "islands" are shaped in cross section like a circle from 6 to 12 nm in diameter and ~1 nm in height in the direction of growth. Their concentration exceeds 10^{11} cm^{-2}, and the average distance between them is ~ 10 nm.

The given samples differ from similar samples studied previously [4–6]. The main difference is that AlInAs antidots contain no electrons and, therefore, are electrically neutral, which determines the short-range character of the random potential generated by these antidots. Another important feature is that the distance between neighboring antidots is of the order of the antidot diameter. Hence, the given system can actually be considered as a heterojunction with artificially introduced interface roughness, which generates a random scattering potential with a correlation radius of ~10 nm. The measurements of CR were carried out using a Fourier spectrometer in the Faraday geometry at a temperature of 2.1 K. The electron concentration was estimated from the CR spectra and was varied using both a gate and a short-time exposure to a red photodiode.

3. A typical series of CR spectra is displayed in Fig. 1. Each curve was obtained at its own fixed magnetic field, and the difference between the field values corresponding to neighboring curves comprises 0.35 T. The most pronounced feature of the series of spectra presented here is a sharp narrowing of the CR line in

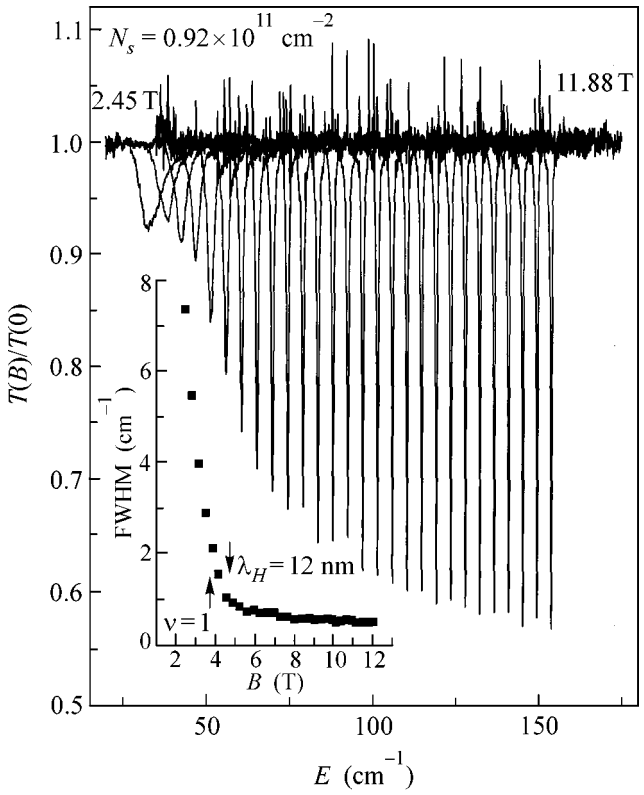

Fig. 1. Cyclotron resonance spectra in magnetic fields for a sample with the electron concentration $n_s = 0.85 \times 10^{11}$ cm^{-2}. Inset: the half-width of the cyclotron resonance line as a function of the magnetic field.

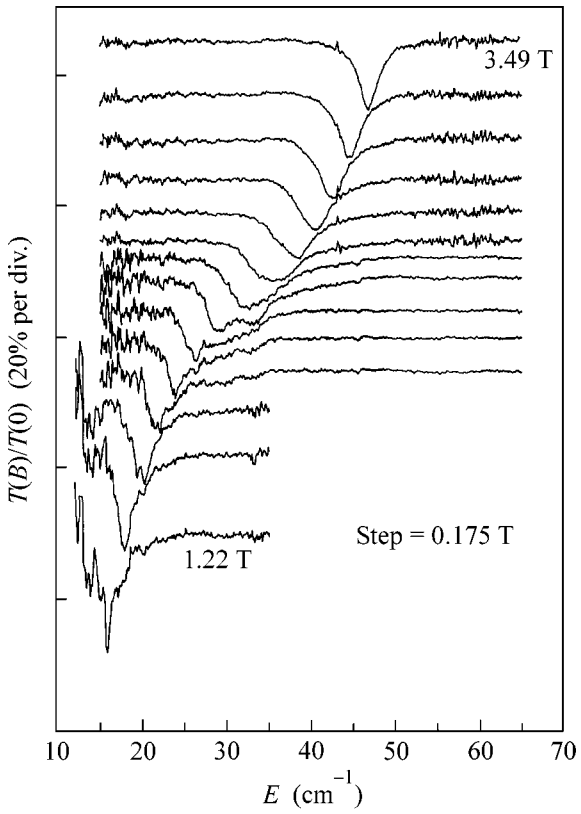

Fig. 2. Switching of the cyclotron resonance line to a higher energy mode for a sample with the electron concentration $n_s = 0.85 \times 10^{11}$ cm^{-2}.

strong magnetic fields. At a magnetic field of 12 T, the half-width of the CR line is only 0.5 cm^{-1}. Such narrow CR lines were observed previously only in top-quality and very pure GaAs/AlGaAs heterojunctions [7]. The concentration and transport mobility of electrons obtained from an analysis of Shubnikov–de Haas oscillations in the structures investigated in this work are equal to $n_s = 0.85 \times 10^{11}$ cm^{-2} and $\mu_T = 9.3 \times 10^4$ cm^2 V^{-1} s^{-1}, respectively. The low mobility, coupled with the fact that the spin splitting in magnetic fields corresponding to odd filling factors (except for $\nu = 1$) is not allowed in SHO, points to the occurrence of strong disordering in the system [8]. Under these conditions, such a strong (more than an order of magnitude) narrowing of the CR line is indicative of the suppression of the pulse relaxation of carriers in a strong magnetic field.

"Switching" in the range of magnetic fields 1–3 T from the CR mode to another mode with a higher frequency shifted by a certain value ω_0 with respect to the cyclotron mode is another specific feature of CR spectra (Fig. 2).

Note that these features are absent in the structure identical in composition and grown under similar conditions but containing no array of antidots.

The main features of the CR spectra in the given system strongly depend on the carrier concentration. The characteristic carrier concentration $N_s \sim 10^{11}$ cm^{-2} that corresponds to the concentration of antidots can be determined based on the obtained experimental data. The behavior of CR sharply changes when the carrier concentration becomes smaller than N_s. In this case, ω_0 depends on the carrier concentration (Fig. 3); on the contrary, the magnetic field B_s corresponding to the saturation of the half-width of the CR line does not depend on the concentration and equals approximately 4.5 T for $n_s < 10^{11}$ cm^{-2}.

Quite the reverse picture is observed for $n_s > 10^{11}$ cm^{-2}: now, ω_0 does not depend on the carrier concentration, and B_s exhibits notable correlations with the filling factor.

4. The potential acting on a particular electron is summed up from the random potential of ionized donors separated from the plane of the 2D electron system by a spacer with $D = 20$ nm, the potential created by the other electrons, and the random potential created

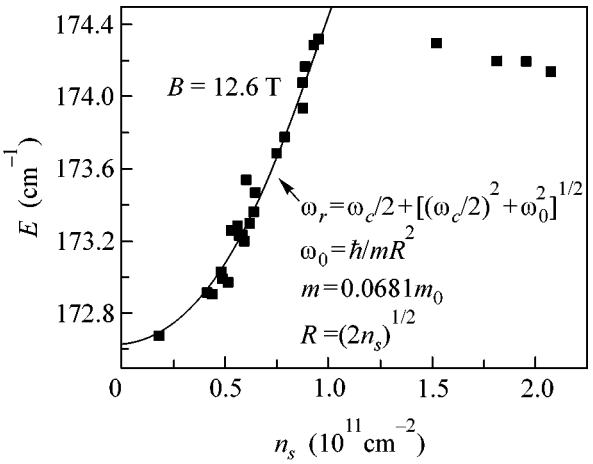

Fig. 3. Position of the absorption line as a function of the electron concentration.

by antidots. Taking into account the fact that the concentration of ionized donors $N = n_s$ and suggesting that the positive charge of donors is distributed uniformly (with the density $\sigma = Ne$) in a plane parallel to the plane of 2D electrons, one can estimate the random potential of antidots by the order of magnitude at

$$W \sim 4\pi e^2 n_s \langle z \rangle / \epsilon,$$

where $\langle z \rangle$ is the characteristic "height" of quantum antidots in the direction of growth, and ϵ is the dielectric constant of the material. The estimation gives the value $W \sim$ 1–2 meV, which is considerably higher than kT = 0.0172 meV (2 K) but lower than the cyclotron energy at already moderate magnetic fields ($H > 2$ T).

In the case of weak magnetic fields, when the characteristic size of the wave function

$$\sim \lambda_H = (\hbar c/eH)^{1/2} \gg L,$$

where L is the correlation radius of the random potential, the CR line experiences homogeneous broadening determined by the relaxation time of the longitudinal component of the electron quasi-momentum. As the magnetic field increases when the magnetic length λ_H becomes smaller than L, the carriers start to "feel" the local potential. In this case, the absorption frequency differs from the cyclotron one. For simplicity, it may be suggested that the local potential minimum is parabolic in shape with the characteristic size R. Hence,

$$\omega_{\text{res}} = \frac{\omega_c}{2} + \sqrt{\left(\frac{\omega_c}{2}\right)^2 + (\omega_0)^2}, \qquad (1)$$

where $\omega_0 = \hbar/m^*R^2$. Because the values of R have a spread, the CR line is broadened, and the broadening is inhomogeneous in this situation. As the magnetic field increases, the broadening of the CR line changes in character. The CR line width determined by the given mechanism decreases with increasing magnetic field, because only the harmonics of the random potential with wave vectors $k > 1/\lambda_H$ can affect the CR peak width essentially [9]. Under the suggestion that the size distribution of antidots is of Gaussian character, the amplitude of such harmonics drops exponentially with decreasing λ_H.

The nonmonotonic character of the resonance frequency as a function of the carrier concentration is of special interest. In the region of small concentrations when n_s is lower than the density of minima of the chaotic potential of antidots, the CR line shifts toward high frequencies as the concentration grows (Fig. 3). This shift cannot be explained by the occurrence of nonparabolicity. The given effect may indicate that the effective potential acting on a particular electron is determined by electron–electron interactions rather than the potential of antidots. In other words, a strongly correlated state of the Wigner crystal type can form under these conditions [10].

Previously, a narrowing and a shift of the CR line were observed in inversion layers at the Si surface in a number of works [11–14]. The results obtained were interpreted by invoking models that also involve electron–electron interactions such as charge density wave pinning [11], Wigner crystal [12], and Wigner glass [13]. Apparently, the effects observed in these works were due to the occurrence of a random scattering potential arising because of the strong roughness of the SiO_2 surface at the interface with Si.

In conclusion, we would like to emphasize that the results presented in this work point to the formation of a strongly correlated electron state. This state can be observed experimentally because of the occurrence of a random potential (in the given case, the potential of antidots) violating the conditions of the Kohn theorem. A more comprehensive analysis of this state and of the role of such parameters as the electron concentration and the random potential amplitude and correlation length will be presented in further publications.

This work was supported by the Russian Foundation for Basic Research, INTAS (project no. 99-01146), and the program Physics of Solid-State Nanostructures.

REFERENCES

1. W. Kohn, Phys. Rev. **123**, 1242 (1961).
2. J. Richter, H. Sigg, K. von Klitzing, and K. Ploog, Surf. Sci. **228**, 159 (1990); Phys. Rev. B **39**, 6268 (1989).
3. C. M. Hu and E. Batke, Phys. Rev. Lett. **75**, 918 (1995).
4. G. Yusa and H. Sakaki, Appl. Phys. Lett. **70**, 345 (1997).

5. E. Ribeiro, E. Müller, T. Heinzel, *et al.*, Phys. Rev. B **58**, 1506 (1998).
6. S. Cina, D. D. Arnone, H. P. Hughes, *et al.*, Phys. Rev. B **60**, 7780 (1999).
7. R. J. Nicholas, M. A. Hopkins, D. J. Barnes, *et al.*, Phys. Rev. B **39**, 10955 (1989).
8. M. M. Fogler and B. I. Shklovskii, Phys. Rev. Lett. **80**, 4749 (1998).
9. I. V. Kukushkin, S. V. Meshkov, and V. B. Timofeev, Usp. Fiz. Nauk **155**, 219 (1988).
10. Yu. E. Lozovik and V. I. Yudson, Pis'ma Zh. Éksp. Teor. Fiz. **22**, 26 (1975) [JETP Lett. **22**, 11 (1975)].
11. J. P. Kotthaus, Surf. Sci. **73**, 472 (1978).
12. R. J. Wagner *et al.*, Phys. Rev. B **22**, 945 (1980).
13. B. A. Wilson, S. J. Allen, Jr., and D. C. Tsui, Phys. Rev. Lett. **44**, 479 (1980); Phys. Rev. B **24**, 5887 (1981).
14. J.-P. Cheng and B. D. McCombe, Phys. Rev. B **44**, 3070 (1991).

Translated by A. Bagatur'yants